ISSN: 2175 9146

JOURNAL OF AEROSPACE TECHNOLOGY AND MANAGEMENT

VOLUME NO. 17
ISSUE NO. 3
SEPT- DEC 2025

ENRICHED PUBLICATIONS PVT.LTD

JE - 18,Gupta Colony, Khirki Extn,
Malviya Nagar, New Delhi - 110017.
E- Mail: info@enrichedpublication.com
Phone :- +91-8877340707

ISSN: 2175 9146

Journal of Aerospace Technology and Management

Aims and Scope

The Journal of Aerospace Technology and Management (JATM) is an open-access journal devoted to research and management on different aspects of aerospace technologies.

For all accepted manuscripts, the correspondence author will be asked to contribute with the Article Processing Charge, which will be applied to editorial services that support the publishing process, like editing, proofreading, indexing and dissemination.

The value is fixed per article, independent of its length and is R$ 800,00 (in Brazilian reais) or U$300,00 (in American dollars). In exceptional cases, the editorial board may waive a contribution upon reasonable request.

JATM accepts manuscripts already published in preprint, considered reliable by the editorial committee, and must be informed in the Open Science Compliance Form that must be submitted as a supplementary file to the Manuscript.

ISSN: 2175 9146

Journal of Aerospace Technology and Management

EDITORS IN CHIEF

ISSN: 2175 9146

Journal of Aerospace Technology and Management

(Volume No. 17, Issue No. 3, Sept- Dec 2025)

Contents

ISSN: 2175 9146

Simulation and Measurement of Plume Characteristics of a Hall Thruster with 12.5 kW

Mingming Sun1,Hai Geng1 , Chao Liu1 , Jun Gao1 , Pei Li1 , Shangmin Wang1

1.China Academy of Space Technology , Shangmin Wang1 – Lanzhou Institute of Physics – Science and Technology on Vacuum Technology and Physics Laboratory – Lanzhou/Gansu – China.

A B S T R A C T

To rapidly and cheaply obtain the plume characteristics of a 12.5 kW Hall thruster, a simulation model based on the fluid method is developed, and a plume measurement is conducted to verify and compare with the simulations. The results show that the discharge process will mainly occur in the upper part of the discharge channel, and the error between simulations and measurements of the magnetic field is less than 5%. The pressure in the discharge channel is the highest and the average pressure is about 0.12 Pa. In the plume diffusion region, the plasma density decays slightly along the axial direction and rapidly in the radial direction. Additionally, the plasma density and the electron temperature from the discharge channel outlet to the upper boundary of the plume region are in the range of 6.2 × 101 6 to 5.2 × 1017 m-3 and 1.8 to 12.2 eV, respectively. In the plume measurement, a single Faraday probe is used to scan and measure the beam current, and the simulations are consistent with the experiments. The simulation model basically achieves the purpose of obtaining the plume characteristics with certain accuracy, low cost and rapidly.

Keywords: *Hall thruster; Ion beams; Plasma discharges; Plasma diagnostics.*

INTRODUCTION

Based on the advantages of lower cost and high reliability, Hall thrusters have been widely used in many space missions such as satellite orbit adjustment, attitude control, and rotation (Huang et al. 2011; Kozubskii et al. 2003; Mazouffre 2016). However, Hall thruster plumes consist of electrons, ions, neutrals and sputters, which can lead to surface contamination and surface charging of the spacecraft (Goebel et al. 2014; Tajmar et al. 2001). Therefore, with the continuous expansion of in-orbit application missions, the influence of the thruster plume on spacecraft operation has received more attention. Meanwhile, the interactions between the thruster plume and the spacecraft determine the layout of the thruster and other spacecraft carrying equipment, such as the solar arrays, antennas, and so on. Additionally, the plume density and distribution also determine the working parameters of the thruster, such as plume divergence angle and thrust density. That is, the higher the axial plume density, the smaller plume divergence angle, and the higher the thrust density. As shown in Fig. 1, the 12.5 kW Hall thruster with a (discharge channel) diameter of 200 mm is developed by the Lanzhou Institute of Physics (LIP), and its application is for the future nuclear power propulsion and deep space exploration in China. To optimize the working parameters of the 12.5 kW Hall thruster, it is necessary to study the

plume characteristics of the thruster.

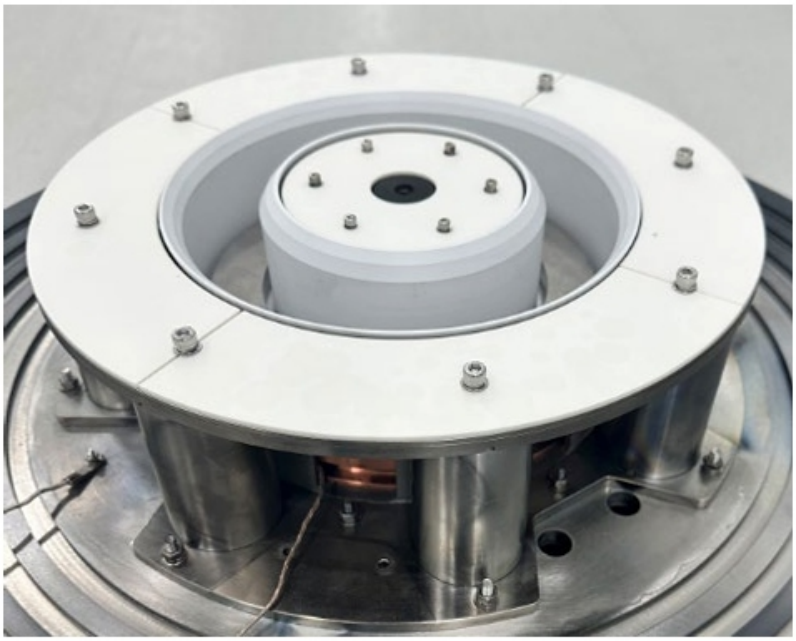

Source: Elaborated by the authors.

Figure 1. The 12.5 kW Hall thruster developed by LIP.

T he study of plume characteristics includes simulation and experimental measurement. There are three methods to simulate the plume characteristics: the fluid method, the full particle method, and the hybrid simulation. The difference between the three methods is the treatment of particles in the plume, that is, the use of fluid equations, particle motion equations, or a combination of the two types of equations to deal with the plume particles. Since the 1980s, some researchers have calculated and studied the plume of Hall thrusters. Typically, David et al. (1999) built a plume simulation model of a Hall thruster using the particle-in-cell direct Monte Carlo collision (PIC-DSMC) method, and the results indicated that the plume consists of quasi-neutral plasma and collision-free electrons, hence the effect of the magnetic field (MF) on the thruster plume can be ignored. Additionally, the simulation results of beam current density were in good agreement with the experimental results. Taccogna et al. (2008) investigated collisions between different types of particles in the plume by the full particle simulation method. In the simulation, the electron temperature in the plume near-field region was assumed to be constant, and the plume as a whole was electrically neutral. Boyd et al. (2002) and Keidar et al. (2005) added a fluid model to the full particle model, which was used to solve electron density. The simulations were compared with the measurement results, and the results showed that plasma density in the near-field of the plume was close to the measurements. Since 2010, studies on plume modeling of Hall thrusters have gradually increased, and the models were mainly based on axial and radial modeling, while the solution area included the discharge channel and near-field plume region. For example, Andreussi et al. (2017) and Kawashima et al. (2018) used a two-dimensional (z and r direction) hybrid model to simulate the Hall

thruster discharge channel and plume near-field region, and the solution of potential in the evaluation was treated as plasma quasineutral, that is, the effect of self-consistent electric field (ES) was ignored, and the experiments showed that it had no great influence on the simulation results of the discharge process. Domínguez et al. (2018) and Campanell et al. (2015) established a full-particle radial model of the discharge channel by using the PIC-MCC method, and concluded that the non-Maxwell distribution of electrons in the discharge channel has some influence on the plasma sheath. Therefore, controlling the secondary electron emission coefficient can keep the stability of the sheath. Merino et al. (2015) used a full fluid model to quickly predict the spatial distribution of plasma in the plume near-field region and found that the fluid method can greatly expand the calculation region, and the boundary conditions (including thruster input parameters, plume boundary settings, etc.) have an important impact on the simulation results of the thruster plume. Cao et al. (2020), Lu et al. (2018), and other researchers have carried out computational simulations on the charge exchange (CEX) ion distribution and etching of discharge channels. The measurements of plume characteristics include contact methods and non-contact method represented by probe measurement (Long et al. 2024) (such as Faraday probe, Langmuir probe) and optical measurements (Linnell et al. 2006) (such as laser-induced fluorescence method, spectral diagnosis). Measuring the plume current density with probes is the cheapest and easiest to achieve, while optical measurement requires expensive instruments and a special transparent glass for the vacuum chamber to obtain the plume parameters. As mentioned above, although there have been many simulation and measurement studies on the plume characteristics of Hall thrusters, there are few studies on the plume characteristics of high-power Hall thrusters, and most of research chooses full-particle or hybrid simulation models, require high cost and time to develop models. Moreover, due to the urgent on-orbit tasks, the development cycle of thrusters is correspondingly shortened, and the final structure of thrusters often needs several iterations of design improvement. Therefore, developing an efficient, cheap, and accurate plume simulation model and obtaining the characteristics of the plume have obvious engineering value for accelerating the structural improvement of high-power Hall thrusters.

T he purpose of this paper is to quickly establish an efficient and cheap plume model using commercial software, and the model needs to have a certain level of precision. The plume characteristics are then evaluated, and the simulations are verified by experiments. According to the comparison results, the accuracy of the model will be verified, and it will be estimated whether the model can be used for rapid simulation of plume characteristics. Additionally, theoretical results can be used for the possible improvement of existing structures improvement in the future.

METHODOLOGY

As shown in Fig. 1, the 12.5 kW Hall thruster adopts a centering cathode design, where the cathode is

installed at the center of the thruster's geometric symmetry. This facilitates the symmetry of the plume and results in higher anode efficiency. Considering the advantages of the three plume simulation methods and the purpose of rapid iterative thruster structure optimization, the fluid method is adopted to obtain the plume characteristics. Therefore, COMSOL Multiphysics coupling software is used for the simulation, hence COMSOL is suitable for inexpensive and quick fluid parameter studies, but the convergence of calculations needs to be solved (Gabriel 2005).

T he fluid method is to obtain the relevant parameters of the plume particles by solving the magneto-fluid equation, with certain assumptions made in the calculation, which mainly include:

• All three types of particles (electrons, ions, and atoms) in the plume are simulated using fluid equations;

• The calculation area consists of the discharge channel and the plume near-filed region (2 to 3 times the diameter of the discharge channel (Andreussi et al. 2017), but considering the comparison with the test, the length of calculation area is extended to 1 m;

• The ES in the plume area is an electrostatic field, and the ES distribution is obtained by the potential relationship when the thruster is working steadily. Here, the influence of the plasma self-consistent ES is ignored, as the plasma beam in the Hall thruster plume region is electrically neutral due to the relatively weak MF;

• The influence of the cathode on the plume is ignored. This is because, after the discharge is stabilized, the number of electrons emitted from the hollow cathode is constant. Therefore, an electron flux boundary is set in the fluid model to simulate the electron emission. Additionally, the cathode has no effect on the distribution of the MF in the plume diffusion region, and the potential of the cathode is only about 11 to 18 V relative to the power ground, which is much lower than the potential difference (600 V) between the anode and the power ground;

• The influence of the plasma sheath on the potential distribution is ignored. This is because, to satisfy the quasi-neutrality of the plasma, the mesh size used in the fluid model is much larger than the Debye length of the plasma (about 0.2 to 1 mm) in the plume region.

As shown in Figs. 1 and 2, the 12.5 kW Hall thruster adopts an axisymmetric structure design, with the cathode is mounted at the geometric center of the thruster. This is because the built-in cathode can obtain a smaller plume divergence angle, and can effectively improve the anode efficiency (Ding et al. 2018; Hofer et al. 2008). Figure 2a shows the installation relationship of various components inside the thruster, with the magnetic pole being the main supporting component. Other components (such as the anode, discharge channel, etc.) are installed on the magnetic pole. In this structural design, the thermal conduction path can be divided into axial (along the discharge channel) and radial (along the diffusion plate). The axial heat conduction path is mainly "the energy deposition in the discharge channel – interior stay and magnetic pole – diffusion plate and thruster base." The components along this path are

mainly metal, and the heat transfer is mainly through contact heat conduction. In contrast, due to the gaps between the various components in the radial direction, most of the heat is transferred in the form of surface-tosurface radiation, with some heat transferred along the diffusion plate. Therefore, although the thruster operates at a power of up to 12.5 kW , the high-temperature components are mainly the discharge channel and the interior coil (measured temperature ranges from 300 to 318 °C), while the exterior coil and the base have lower temperatures (ranging from 150 to 210 °C).

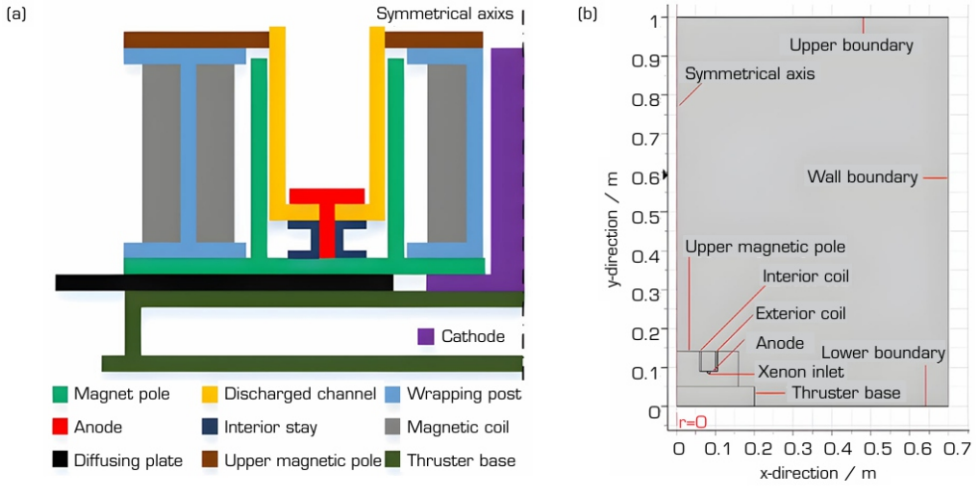

Source: Elaborated by the authors.

Figure 2. Structure and simulation area of 12.5 kW Hall thruster. (a) Internal structure of the thruster; (b) Schematic diagram of simulation area.

Figure 2b shows a schematic diagram of the simulation area. The discharge area is axisymmetric and includes both the thruster and the plume diffusion area. The thruster model is built according to the real structure size, but only the discharge channel, coil, magnetic pole, and base are retained to simulate the discharge process. The radius of the upper magnetic pole and the width and depth of the discharge channel are 0.16 m, 0.03 m and 0.06 m, respectively. Additionally, the plume diffusion area includes the upper and lower boundaries as well as the wall boundary. The upper boundary simulates the moving plane of the Faraday probe. According to the actual position of the probe when the plume is measured, the distances between the upper and lower boundaries, as well as between the upper boundary and the thruster outlet, are set to 1 m to 0.86 m, respectively. The lower boundary simulates the thruster-mounting platform. According to the distance between the vacuum facility wall and the thruster, the distance between the wall boundary and the symmetrical axis is set to be 0.7 m, ensuring that the plume can be fully diffused.

Table 1 shows the rated parameters of the 12.5 kW Hall thruster. The electrical parameters and gas supply parameters listed in the table, such as anode voltage and current, and flow rate of the cathode and the anode, are determined after several iterations of performance tests in a vacuum environment. The thrust is measured by the pressure sensor for several times and obtained by averaging. Other parameters, such as specific impulse and efficiency, are obtained through theoretical calculation. Additionally, it is

noted that the voltages of the anode, keeper, and base are all the difference relative to the power ground.

Table 1. Rated work parameters of a 12.5 kW Hall thruster.

Parameters	Values	Parameters	Values
Thrust/mN	533	Efficiency	52.9%
Specific impulse/s	2,800	Total power/W	12,500
Anode voltage/V	600	Anode flow rate/mgs^{-1}	20
Anode current/A	20.4	Cathode flow rate/mgs^{-1}	0.47
Keeper voltage/V	18	Base voltage/V	25
Turns of interior coil	490	Turns of exterior coil	260
Interior coil current/A	5	Exterior coil current/A	3

Source: Elaborated by the authors.

Discharge model and boundary settings

As shown in Fig. 2b, the discharge model retains the main discharge area according to its real size, and the discharge channel is integrated with the plume diffusion region, so that the simulation results are continuous. According to the discharge process of the thruster, the static ES module, MF module, single-phase flow (SPF) module, and drift-diffusion (DD) module of COMSOL are used in the simulation. The ES, the MF, and the SPF modules are used to obtain the distribution of the ES, MF, as well as the f luid velocity, neutral density, and other parameters. These parameters are used as calculation boundaries or setting conditions for the DD module.

The ES distribution directly affects the motion of ions and electrons, thereby changing the plume characteristics and significantly affecting the diffusion of the plume. As shown in Fig. 2 and Table 1, the potentials of the upper magnetic pole and the base are equal, set to 25 V. The potential of the upper boundary, as shown in Fig. 2b, is set to -30 V because the upper boundary simulates the moving plane of the probe. That is, the bias voltage applied on the probe is -30 V, with the negative of the bias power is grounded to the vacuum facility. Moreover, the potentials of the wall boundary and the lower boundary, as shown in Fig. 2b, are set to 0 V to simulate the facility wall. The ES can be calculated by $= E - \nabla V$. Additionally, the ES distribution is obtained based on the assumption that the plasma beam is electrically neutral, and the self-consistent electric field of the discharged plasma is ignored.

The MF distribution mainly affects the movement of electrons, which indirectly influences the movement of ions and changes the plume distribution. According to previous research, adjusting the MF distribution has noticeable effects on the plume divergence angle and ion density in the plume near-field region (Yu et al. 2017). As shown in Fig. 2b and Table 1, the coil closer to the symmetrical axis is the interior coil, and the turns and current of the interior coil are set to 490 and 5 A, respectively, while those of the exterior coil are set to 260 and 3 A, respectively.

In the neutral fluid simulation of the calculation area, the boundaries are first set according to the actual size and gas supply rate, and then the boundaries are slightly adjusted according to whether the result is convergent. As shown in Fig. 2b and Table 1, for the discharge channel, the interior diameter of the xenon inlet is 5 mm. The SPF module is adopted to obtain the velocity and pressure of the neutral gas in the calculation area. According to the previous temperature measurement results of the 12.5 kW Hall thruster, the temperature of the inner wrapping post and the discharge channel after stable operation is in the range of 300318 °C. In many cases, Hall thrusters operate under a low-density neutral gas, so the Knudsen number of the neutral gas is much greater than one, while collisions between the neutrals can be ignored and the neutrals in the channel are free-molecule (Katz et al. 2011). In the simulation, the turbulence is ignored, and the boundaries of all walls in the channel are set to no-slip, meaning that the velocity of the fluid on the walls is zero. The xenon inlet is set to a mass flow boundary with a value of 20 mg·s-1, and the flow direction is from the inlet to the channel. The initial pressure of the calculation region is set to 0.005 Pa, and the upper, wall, and lower boundaries shown in Fig. 2b are set as gas outlets with a pressure of 0.008 Pa (measured vacuum degree after stable operation).

Based on the DD equation, the DD module is used to simulate the generation and diffusion of the charged plasma in the calculation area, which regards the plasma as a fluid flow, and the flow is effected by magnetic and ES. The DD module mainly contains the electron continuity equation, the electron DD equation, and the energy balance equation. The electron continuity equation is expressed as follows:

$$\frac{\partial n_e}{\partial t} + \nabla \Gamma_e = R_e \tag{1}$$

where ne is the plasma density, Γe is the electron flux in the channel, and Re is the generation rate of the electrons (unit is m-3s-1). The electrons are produced by elastic, excitation, and ionizing collisions, respectively, and the reaction rate coefficients corresponding to different collision type are defined as k1, k2, and k3. Each collision type has its own reaction coefficient (Miller et al. 2002), and all the reaction coefficients have a similar expression, which is expressed as σν , where σ and ν are the collision cross section and the total collision frequency (determined by the electron temperature Te), respectively. It is noted that elastic collisions are ignored, as there are almost no Maxwellian electrons produced during elastic collisions, but only energy transfer occurs in most cases. T herefore, the excitation reaction rate r2 and the ionization reaction rate r3 are expressed as k2n0ne and k3n0ne. The production of Maxwellian electrons and the total reaction rate Re in discharge channel can be expressed as:

$$\begin{aligned} &e + X_e^* \rightarrow X_e^+ + 2e \\ &e + X_e \rightarrow X_e^+ + 2e \\ &R_e = r_2 + r_3 = k_2 n_0 n_e + k_3 n_0 n_e \end{aligned} \tag{2}$$

The electron flux Γ_e is obtained by the DD equation, which is shown as:

$$\Gamma_e = -(\mu_e \cdot E) n_e - D_e \cdot \nabla n_e \tag{3}$$

where E and μ_e are the ES and electron migration coefficient, respectively, and μ_e can be expressed as:

$$\mu_e = e / m_e \nu (1 + \Omega_e^2) \tag{4}$$

Considering that the number of electrons generated by collisions between ions and ions, ions and atoms, is much lower than that generated by collisions between electrons and atoms, electrons and ions. Therefore, collisions between ions and ions and between ions and atoms are ignored. Thus, the total collision frequency ν is consisted of the collision frequency ν_{en} between electrons and neutral atoms, as well as the collision frequency ν_{ei} between electrons and ions. ν_{en} and ν_{ei} are given by Katz *et al.* (2004) and Book (1987), respectively. Ω_e is the term of electron Hall parameter correction and reflects the ability of the MF to restrain the electrons, which can be expressed as $\Omega_e = eB/m_e\nu$, where B is MF distribution. D_e is the electron diffusion coefficient, which has Einstein's relation with μ_e, and expressed as $D_e = \mu_e T_e$. The energy balance equation can be expressed as:

$$\frac{\partial n_\varepsilon}{\partial t} + \nabla\Gamma_\varepsilon + \mathbf{E}\cdot\Gamma_e = S_{en} \tag{5}$$

where n_ε and Γ_ε are the energy density and energy density flux of the electrons, respectively, and determined by μ_e, n_e and T_e. S_{en} is the collision energy loss, consisting of the elastic collision energy loss d_{e1}, the first-order energy loss d_{e2} and the second-order energy loss d_{e3} caused by the ionizing collision between electrons and atoms. Table 2 gives the setting of the main parameters, where k is Boltzmann constant and m_e is electron mass.

Table 2. Main parameter settings in DD module.

Parameters	Expressions	Description
k_1	$1.99^{-14}\ T_e^{0.93}\ e^{0.41/T_e}$	Elastic collision coefficient
k_2	$1.93^{-19}\ e^{11.6/T_e}/T_e^{0.5}[8eT_e/\pi/m_e]^{0.5}]$	Exciting collision coefficient
k_3	$10^{-20}(3.97 + 0.643T_e - 0.0368T_e^2) \times e^{-12.127/T_e}$ $[8eT_e/\pi/m_e]^{0.5}$	Ionizing collision coefficient
r_1	$k_1\ n_0\ n_e$	Elastic reaction rate
r_2	$k_2\ n_0\ n_e$	Exciting reaction rate
r_3	$k_3\ n_0\ n_e$	Ionizing reaction rate
d_{e1};d_{e2};d_{e2}	0; 8.31; 12.13	Energy loss
R_e	$r_2 + r_3$	Production rate of electrons
S_{en}	$-e(r_1\ d_{e1} + r_2\ d_{e2} + r_3\ d_{e3})$	Collision energy loss
σ_{en}	$6.6^{-19}\ (T_e/4 - 0.1)/[1+(T_e/4)^{1.6}]$	Collision cross section
$\ln\Lambda$	$23^{-0.5}\log\ (10^6\ n_e/T_e^3)$	Coulomb logarithm
V_{en}	$\sigma_{en}\ n_0\ (8kT_e/\pi/m_e)^{0.5}$	Collision frequency (electrons and neutrals)
V_{ei}	$2.9^{-12}\ n_e\ ln\Lambda/T_e^{1.5}$	Collision frequency (electrons and ions)
μ_e	$e/[m_e\ (\nu_{en} + \nu_{ei})]$	Migration coefficient

Source: Elaborated by the authors.

The initial density and energy of the electrons in the entire model are set as 1×10^{18} m^{-3} and 3 eV, respectively. As shown in Fig. 2b, the reaction rate R_e is only set in the channel, so the plume mainly diffuses by the effect of electric and MFs. The electron reflection coefficient of the discharge channel walls, shown in Fig. 2b, is set to 0, meaning that the secondary electrons emission by the wall is ignored. Additionally, since the distance between the upper and the wall boundaries from the discharge channel is 0.86 m and 0.7 m, respectively, which is much larger than the characteristic length of the thruster (i.e., the width of discharge channel of 0.03 m), it can be approximatively considered that the distance between the upper and the wall boundary from the thruster is infinite, and the electron flux at these two boundaries is set to 0, that is, the density and energy of electrons are both 0. After defining all the boundaries and parameters of the model, then the simulation processes in the MF, ES, and SPF modules are set to steady-state simulations. Moreover, the simulation process in the DD module is set as a transient simulation, and the simulation duration is from 10^{-8} s to 10^{-1} s, during which the discharge process and plume diffusion can reach a steady state.

Simulation results and analysis

The potential distribution and MF distribution are shown in Figs. 3a and b. Figure 3a shows that the closer to the outlet of the thruster, the higher the potential and the larger the potential gradient. Additionally, the distribution of potential shows obvious axisymmetric characteristics and the direction of ion motion is perpendicular to the isopotential line. Therefore, the plume extracted from the discharge channel is divergent, and the divergence angle has a strong relationship with the curvature of the isopotential line.

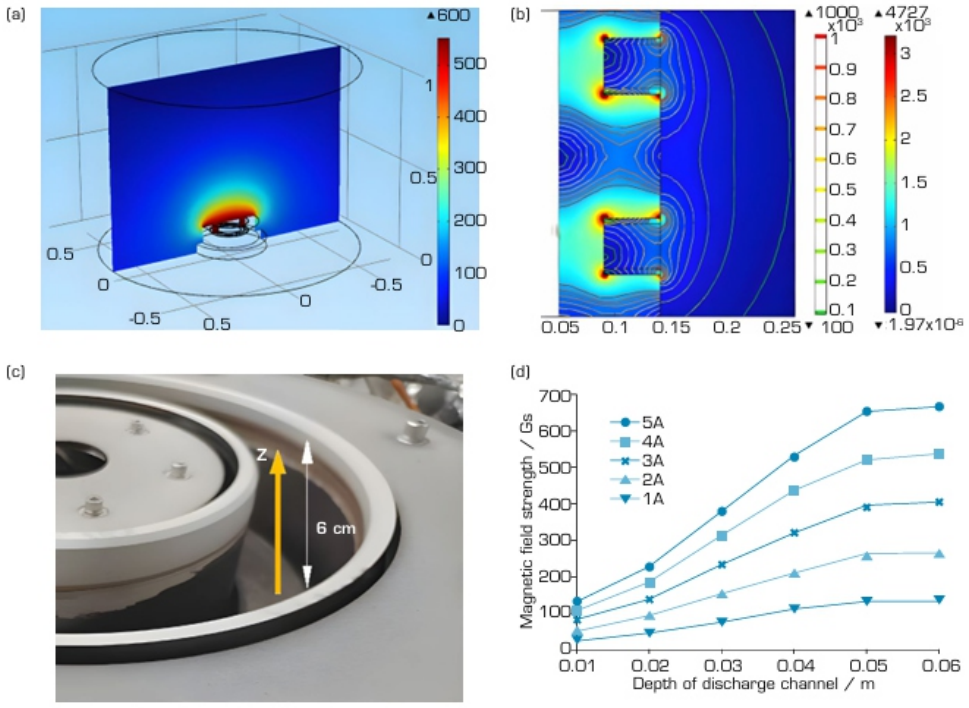

Source: Elaborated by the authors.

Figure 3. Potential and MF distribution and MF measurement. (a) Potential/V; (b) MF distribution/Gs; (c) MF test; (d) Measured MF/Gs.

Based on the interior and exterior coil turns and current conditions in Table 1 (the turns and current of the interior and exterior coil are 490/5 A and 260/3 A, respectively), Fig. 3b shows the MF distribution in the channel and plume near-field region. The MF has no effect on ion motion, while it mainly restrains electron motion and controls the ionization reaction rate. The distribution of isopotential lines indicates that the MF in the channel is not uniform, and there is an obvious gradient along the axis of the discharge channel. This is because the MF is generated by the coil, and the number of turns and current of the interior coil are greater than those of the exterior coil, so the closer to the interior coil of the channel, the stronger the MF. Meanwhile, the MF closer to the channel bottom is lower, which means the discharge process will mainly occur in the upper part of the discharge channel. According to the previous research (Morozov *et al.* 2000), most discharge processes of the Hall thruster are concentrated in the upper 30% region of the discharge channel.

To estimate the accuracy of the simulation results, a LakeShore Model-425 Gauss meter is used to measure the MF in the channel, and the test method is shown in Fig. 3c. Along the centerline of the discharge channel with a depth of 6 cm, that is, along the z-axis in the positive direction shown in the figure, the MF at different points is measured with a step size of 1 cm. Additionally, the same current is applied to the interior and exterior coils, ranging from 1 A to 5 A, and the MF is measured five times in steps of 1 A. The measurement results are shown in Fig. 3d. According to the same conditions as the test, the MF at the same measuring points for different currents is calculated, and the comparison results are shown in Table 3. Table 3 shows that the comparison errors are all less than 5%, which proves that the simulation results are accurate.

Table 3. Comparison of simulation and measurement results of MF.

Current/ A	5	4	3	2	1
Measurements/Gs	668.20	536.83	402.54	267.78	134.23
Simulations/Gs	650.1	539.4	404.7	272.5	135.3
Errors	2.71%	0.48%	0.53%	1.78%	0.79%

Source: Elaborated by the authors.

The fluid velocity simulation results in the calculation area are shown in Fig. 4a, and it can be concluded that the fluid velocity is highest along the axis of the discharge channel, with the average value is in the range of 160 to 200 ms^{-1}. Meanwhile, the fluid ejecting into the plume region shows an obvious diffusion characteristic. In the calculation, it is found that the inner friction of the fluid should be ignored to better achieve computational convergence. Additionally, it is further found that the backflow of the fluid should be ignored to achieve convergence. The neutral density is shown in Fig. 4b. The result shows that the neutral density in the channel is the highest, and in most areas of the channel, the neutral density is in the range of 2×10^{19} to 3×10^{19} m^{-3}. The calculation results can be verified by equation 6, where P is the average pressure in the channel, $\bar{v}$ is the average velocity of xenon atoms, and r_1 and r_2 are the inner circle radius and outer circle radius of the discharge channel, respectively. The average velocity of xenon atoms can be obtained by the gas temperature, then the average pressure in the discharge channel is calculated to be about 0.12 Pa, thus the average atom density in the channel is about 2.9×10^{19} m^{-3}, which is basically consistent with the simulations. Moreover, the simulations are consistent with the previous calculation results (Katz *et al.* 2011), which show that the atom density in the channel is in the range of 1×10^{19} to 5×10^{19} m^{-3}.

$$P = m_a \bar{v} / \pi (r_2^2 - r_1^2) \tag{6}$$

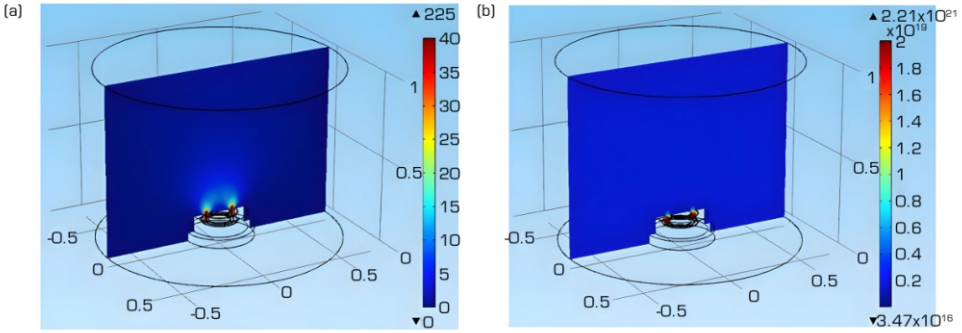

Source: Elaborated by the authors.

Figure 4. Distribution of fluid velocity and neutral density. (a) Fluid velocity/ms^{-1}; (b) Neutral density/m^{-3}.

Figures 5a and d show the characteristics of the discharge plasma in the channel and the plume region. As shown in Fig. 5a, the plasma density along the centerline of the channel is the highest, and the plasma density decreases less along the axial direction. However, the plasma density decreases rapidly along the radial direction of the plume calculation region. This is mainly due to the distribution of the potential isopotential lines, and the ions move in a direction perpendicular to the equipotential line. As shown in Fig. 3a, the decay of potential in the axial direction is low, so the ions move rapidly along the axis under the acceleration of the ES, and the reduction in plasma density is not significant. However, the radial potential distribution decays obviously and has little effect on charged particles. Therefore, the motion of ions along the radial direction is mainly diffusion, and the plasma density decreases rapidly. According to Figs. 5a and b, the plasma density and the electron temperature from the discharge channel outlet to the upper boundary of the plume region are in the range of 6.2×10^{16} to 5.2×10^{17} m^{-3} and 1.8 to 12.2 eV, respectively, while the plasma density and the electron temperature from the channel outlet to the wall boundary are in the range of 4.6×10^{9} to 5.2×10^{17} m^{-3} and 1.2 to 12.8 eV. The distribution of electron temperature shown in Fig. 5b expresses a similar characteristic to the potential distribution. This is because the acceleration of ions is determined by the isopotential lines and the electric potential in the channel and the plume near field area is the highest, thus the ions in these regions can obtain the highest acceleration energy.

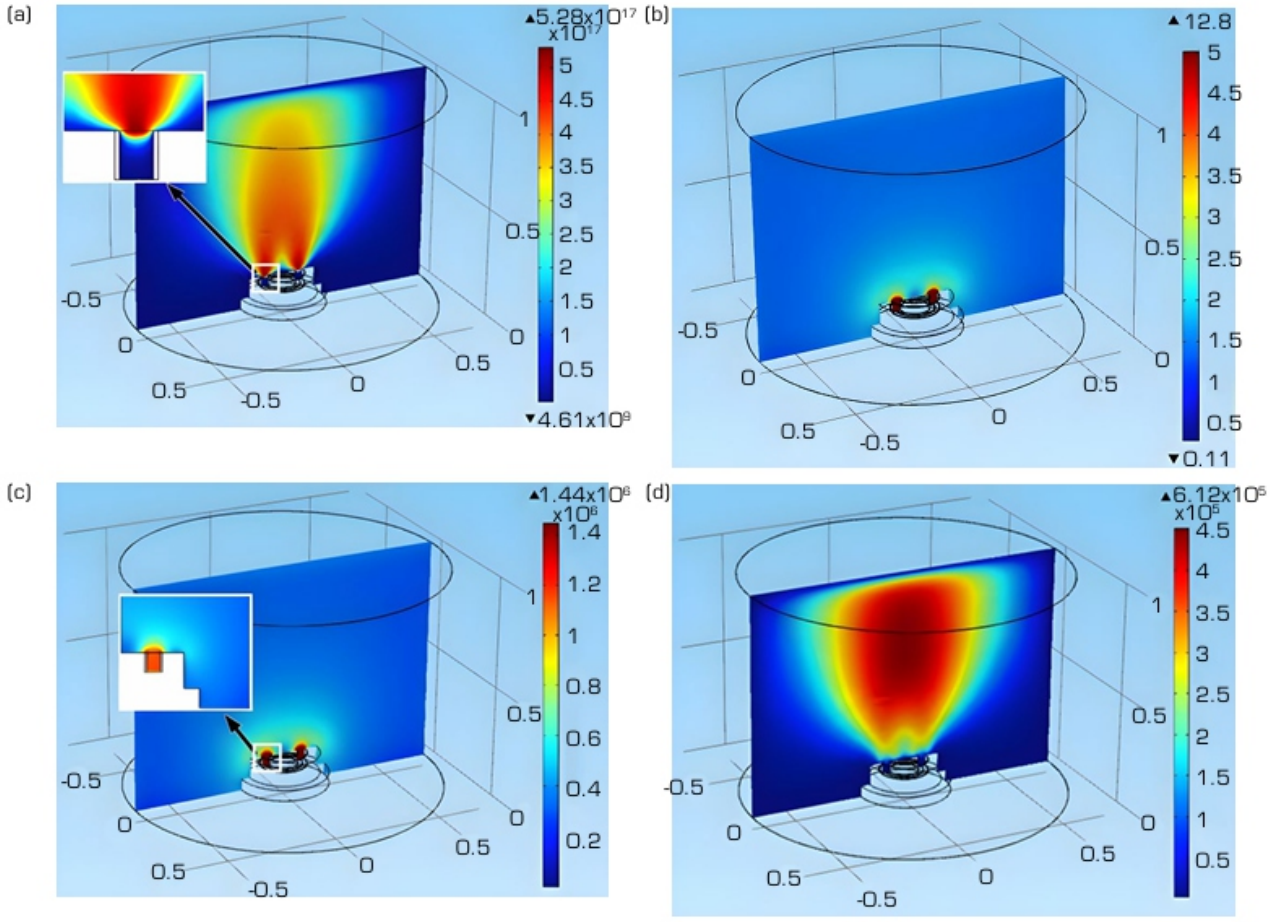

Source: Elaborated by the authors.

Figure 5. Characteristics of thruster plume. (a) Plasma density/m^{-3}; (b) Electron temperature/ eV; (c) Electron-neutral collision frequency/Hz; (d) Electron-ion collision frequency/Hz.

Figures 5c and d show the collision frequencies of electrons and neutrals and electrons and ions, respectively. Collision between electrons and neutrals shows the main ionization and ion production region, while the latter shows the divalent ion production region. The higher the density of divalent ions, the higher the thrust loss of the thruster will be, and the higher density of the divalent ions will lead to the enhancement of discharge energy loss and the decrease in discharge efficiency, causing higher erosion to the discharge channel. As shown in the figure, the collision frequency between electrons and neutrals is in the range of 1×10^6 to 1.44×10^6 Hz, and which is almost concentrated in the channel, where the atomic density is highest. The collision frequency between electrons and ions is in the range of 1.5×10^5 to 4.5×10^5 Hz and is concentrated in the plume diffusion region.

Test results and comparison

Figure 6a shows the simulated plume density near the upper boundary, with the plume density is in the range of 4.9×10^{13} to 8.4×10^{15} m^{-3}. To estimate the precision of the simulation results, a plume test of the 12.5 kW Hall thruster is carried out. The test is conducted in a large vacuum facility at LIP, the vacuum chamber having a diameter of 8 m and a length of 16 m, and the facility is equipped with 6 external cryogenic pumps and 30 internal cryogenic pumps, which can maintain a vacuum of 1.7×10^{-3} Pa under the rated working conditions of the thruster. As shown in Figs. 6b and c, the plume test uses a moving single Faraday probe to collect the beam current. The diameter of the probe collector is 8 mm, and the length of the stainless steel sleeve outside the probe is 14 mm. The thruster is mounted on a fixed bracket, the Faraday probe is installed on a travel mechanism, and the distance from the probe to the thruster base is 0.9 m (z-axis shown in Fig. 6c), and both are at the same height (the height in the y-axis is 0.6 m). The scanning range of the probe is 0 to 1.2 m, and the thruster is installed in the middle position of the scanning distance, that is, at a location of 0.6 m on the x-axis. However, in the actual test, only a distance of 0 mm to 0.8 m is scanned, as the beam has a symmetrical distribution, so the measurement is stopped after scanning the beam peak.

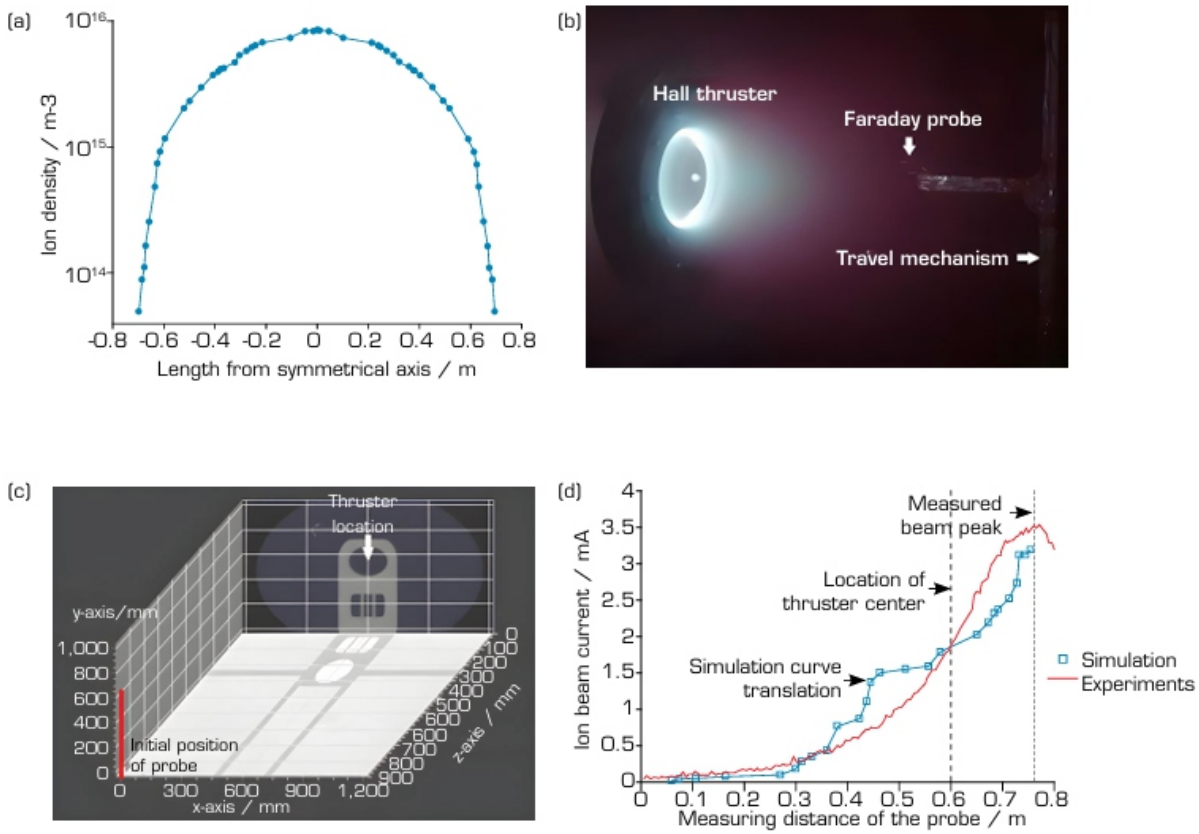

Source: Elaborated by the authors.

Figure 6. Plume measurement and the results comparison. (a) Plume density on the upper boundary/m^{-3}; (b) Plume measurement; (c) Location of the thruster and probe; (d) Comparison of results.

Since the Faraday probe collects beam current, then the simulated plasma density shown in Fig. 6a should be converted into current, as shown in Eq. 7,

$$I_b = n_e e v_i \pi r_0^2 \tag{7}$$

where I_b is the ion beam, v_i and r_0 are the ion velocity (which is calculated to be 2.96×10^4 ms^{-1}) and the radius of the probe collection surface (which is 4 mm), respectively. According to Eq. 7, the plasma density shown in Fig. 6a is converted into beam current to compare with the measurements, and the comparison results are shown in Fig. 6d. It should be noted that the beam peak does not appear at the projection of the thruster center on the moving plane of the probe, that is, 600 mm, but at 780 mm. Therefore, to compare with the test, the simulation curve is translated to ensure that the beam peak also appears at 780 mm. The beam peak does not appear in the projection of the thruster center mainly because the centerline of the thruster is not perpendicular to the moving plane of the probe during installation, and even a small angular deviation will cause a large displacement of the projection of the centerline on the moving plane. Additionally, the focusing effect of the MF on plasma and the uneven gas supply in the discharge channel will lead to the deviation of the beam peak.

According to the comparison results, the simulation results are consistent with the experimental results. However, near the edge of the plume, that is, where the probe moves from 0.3 m to 0.5 m, the variation of the beam current obtained by simulation is obviously higher than that of the measured results (changes from 0.29 A to 1.01 A). This is because the simulated plasma density changes from 1.11×10^{15} to 6.15×10^{15} in this measurement distance (-0.48 m to -0.28 m shown in Fig. 6a), and the corresponding beam current changes from 0.25 A to 1.50 A. Similarly, within the probe travel distance of 0.6 m to 0.78 m, the simulated plasma density changes from 6.78×10^{15} to 8.05×10^{15} in a distance of -0.18 m to 0 m (as shown in Fig. 6a), and the simulated beam current is lower than the measured value. In conclusion, the measured beam current changes more gradually, while the simulations show that the variation of beam current is greater near the edge of the plume, and the closer to the beam center, the smaller the change in beam current, which is due to the boundary settings in the simulation, especially the distribution of ES s and MF s. Additionally, the defects of the fluid method are also an important source of error. Although there are some errors between simulations and measurements in some test distances, in general, the variation of simulated beam current coincides well with the variation trend of measured results.

CONCLUSION

The plume characteristics are of great significance for the on-orbit application and design optimization of the thruster. Therefore, an efficient and inexpensive plume model based on COMSOL software is established and verified by beam current measurement. The comparison results of simulations and experiments show that the fluid method can rapidly obtain plume characteristics, and the fluid method is suitable for the study of macroscopic parameters of the thruster. The simulation model achieves the purpose of obtaining the plume characteristic parameters with certain accuracy, low cost, and rapidly execution. Moreover, the model has obvious engineering value in the optimization and improvement of Hall thruster. For example, according to the plume characteristics reflected in the model, the focus of the thruster plume can be evaluated. That is, based on simulated plume density, the divergence angle of the plume can be obtained, and then the MF and the ES can be constantly adjusted by the model to reduce the divergence angle as much as possible. However, the defects of the fluid method must be considered. Compared with the PIC method, the fluid method ignores the microscopic processes such as electron motion, the sheath in the discharge area, the collision between the particles, and the secondary electron emission effect on the wall of the channel, which will lead to a higher electron temperature of the plasma near the sheath, and a lower plasma density in the plume near-field region, resulting in errors with the measurements. Additionally, another defect of the fluid method is that it requires sufficient parameter settings in the calculation, which is an important source of error. Therefore, more tests and measurements should be conducted in the subsequent study to optimize the boundary and parameter settings of the model to minimize the errors.

CONFLICT OF INTEREST

Nothing to declare.

AUTHORS' CONTRIBUTION

Conceptualization: Sun M; **Methodology:** Sun M; **Software:** Sun M; **Validation:** Sun M and Liu C; **Formal analysis:** Sun M and Liu C; **Investigation:** Geng H and Gao J; **Resources:** Sun M and Li P; **Data Curation:** Sun M and Wang S; **Writing - Original Draft:** Sun M; **Writing - Review & Editing:** Sun M and Liu C; **Visualization:** - **Supervision:** Sun M; **Final approval:** Sun M.

DATA AVAILABILITY STATEMENT

The data are available in a data repository.

FUNDING

Not applicable.

ACKNOWLEDGMENTS

Not applicable.

REFERENCES

Andreussi T, Giannetti V, Leporini A, Saravia M, Andrenucci M (2017) Influence of the magnetic field configuration on the plasma flow in Hall thrusters. Plasma Phys Control Fusion 60(1):014015. https://doi.org/10.1088/1361-6587/aa8c4d

Book D (1987) NRL plasma formulary. Washington D.C.: Naval Research Laboratory.

Boyd D, Dressler A (2002) Far field modeling of the plasma plume of a Hall thruster. J Appl Phys 92(4):1764-1774. https://doi.org/10.1063/1.1492014

Campanell D, Wang H, Kaganovich D, Khrabrov V (2015) Self-amplification of electrons emitted from surfaces in plasmas with E×B fields. Plasma Sources Sci Technol 24(3):034010. https://doi.org/10.1088/0963-0252/24/3/034010

Cao XF, Liu H, Yu DR (2020) Research of the influence of the additional electrode on the Hall thruster plume by particle-in-cell simulation. Chin Phy. B 29(9):095204. https://doi.org/10.1088/1674-1056/aba2e3

David O, Daniel E, Colleen M, James M, Alec D (1999) Modeling of stationary plasma thruster-100 thruster plumes and implications for satellite design. J Propuls Power 15(2):345-357. https://doi.org/10.2514/2.5432

Ding Y, Li H, Li P, Jia B, Wei L, Su H, Sun H, Wang L, Yu D (2018) Effect of relative position between cathode and magnetic separatrix on the discharge characteristic of Hall thrusters. Vacuum 154:167-173. https://doi.org/10.1016/j.vacuum.2018.05.005

Dominguez-Vazquez A, Taccogna F, Ahedo E (2018) Particle modeling of radial electron dynamics in a controlled discharge of a Hall thruster. Plasma Sources Sci Technol 27(6):064006. https://doi.org/10.1088/1361-6595/aac968

Gabriel S (2005) COMSOL modelling of hollow cathodes. Paper presented 2005 35th International Electric Propulsion Conference Exhibit. Georgia Institute of Technology; Atlanta, USA.

Goebel D, Hofer R, Mikellides G, Katz I, Polk J, Dotson B (2014) Conducting wall Hall thrusters. IEEE Trans Plasma Sci 43(1):118-126. https://doi.org/10.1109/TPS.2014.2321110

Hofer R, Johnson K, Goebel D, Wirz R (2008) Effects of internally mounted cathodes on Hall thruster plume properties. IEEE Trans Plasma Sci 36(5):2004-2014. https://doi.org/10.1109/TPS.2008.2000962

Huang W, Gallimore D, Hofer R (2011) Neutral flow evolution in a six-kilowatt Hall thruster. J Propuls Power 27(3):553-563. https://doi.org/10.2514/1.B34048

Katz I, Mikellides I (2011) Neutral gas free molecular flow algorithm including ionization and walls for use in plasma simulations. J Comput Phys 230:1454-1464. https://doi.org/10.1016/j.jcp.2010.11.013

Katz I, Mikellides I, Goebel D (2004) Model of the plasma potential distribution in the plume of a hollow cathode. Paper presented 2004 40th Joint Propulsion Conference & Exhibit. AIAA; Ft. Lauderdale, USA.

Kawashima R, Hara K, Komurasaki K (2018) Numerical analysis of azimuthal rotating spokes in a crossed-field discharge plasma. Plasma Sources Sci Technol 27(3):035010. https://doi.org/10.1088/1361-6595/aab39c

Keidar M, Boyd D (2005) On the magnetic mirror effect in Hall thrusters. Appl Phys Lett 87(12):121501. https://doi.org/10.1063/1.2053351

Kozubskii N, Murashko M, Rylov P, Trifonov V, Khodnenko V, Kim V, Popov G, Obukhov VA (2003) Stationary plasma thrusters operate in space. Plasma Phys Rep 29(3):251-266. https://doi.org/10.1134/1.1561120

Linnell A, Gallimore D (2006) Internal plasma potential measurements of a Hall thruster using plasma lens focusing. Phys Plasmas 13(10):103504. https://doi.org/10.1063/1.2358331

Long J, Huang D, Sun M, Cheng Y, Wang J, Xu L, Guo N, Yang W (2024) Experimental study on beam characteristics of μHT-1 thruster under operating conditions adjustment. Vacuum 219:112735. https://doi.org/10.1016/j.vacuum.2023.112735

Lu C, Qiu P, Cao Y, Zhang T, Chen J (2018) A 3D particle model for the plume CEX simulation. Aeronaut J 122(1255):1425-1441. https://doi.org/10.1017/aer.2018.79

Mazouffre S (2016) Electric Propulsion for Satellites and Spacecraft: Established Technologies and Novel Approaches. Plasma Sources Sci Technol 25(3):033002. https://doi.org/10.1088/0963-0252/25/3/033002

Merino M, Cichocki F, Ahedo E (2015) A collisionless plasma thruster plume expansion model. Plasma Sources Sci Technol 24(3):035006. https://doi.org/10.1088/0963-0252/24/3/035006

Miller J, Pullins S, Levandier D, Chiu Y, Dressler R (2002) Xenon charge exchange cross sections for electrostatic thruster models. J Appl Phys 91(3):984-991. https://doi.org/10.1063/1.1426246

Morozov I, Savelev V (2000) One-dimensional hydrodynamic model of the atom and ion dynamics in a stationary plasma thruster. Plasma Phys Rep 26(3):219-224. https://doi.org/10.1134/1.952841

Taccogna F, Longo S, Capitelli M, Schneider R (2008) Surface-driven asymmetry and instability in the acceleration region of Hall thruster. Contrib Plasma Phys 48(4):375-386. https://doi.org/10.1002/ctpp.200810061

Tajmar M, Gonzalez J, Hilgers A (2001) Modeling of spacecraft-environment interactions on SMART-1. J Spacecr Rockets 38(3):393-399. https://doi.org/10.2514/2.3697

Yu D, Meng T, Ning Z, Liu H (2017) Confinement effect of cylindrical-separatrix-type magnetic field on the plume of magnetic focusing type Hall thruster. Plasma Sources Sci Technol 26(4):04LT02. https://doi.org/10.1088/1361-6595/aa6425

ISSN: 2175 9146

Air Corridor-Based Optimization of Chinese Airspace and Carbon Emission Analysis

Ruiling Han1,2,3 , Xinyue Ran1,* , Huiying Li4

1. Hebei Normal University – School of Geographical Sciences – Shijiazhuang – China.
2. Hebei Key Laboratory of Environmental Change and Ecological Construction – Shijiazhuang – China.
3. Hebei Technology Innovation Center for Remote Sensing Identification of Environmental Change – Shijiazhuang – China.
4. Shijiazhuang Institute of Railway Technology– Shijiazhuang – China.

ABSTRACT

This study theoretically delineates China's current airspace based on airspace management rules, primarily by constructing air corridors to optimize the existing structure, with validation through aviation carbon emissions analysis. First, seven air corridors were delineated based on route clustering analysis, and their significance was further evaluated through carbon emission efficiency comparison. The results show that: 1) the seven corridors are mainly located in central and eastern China, forming a "diamondshaped three-dimensional structure"; 2) there are significant differences in operational scale among the corridors, with the HarbinHaikou route being the most active and the Chongqing-Zhuhai route the least; 3) the total carbon emissions from the seven corridors amount to 619,431 tons, with carbon emissions and efficiency positively correlated with aircraft type, cruising time, and operational scale; 4) the flight density within established corridors is higher than before their formation, and they accommodate more flights. This study provides a broad coverage, highlighting the structural characteristics of China's airspace.

Keywords: *Air corridor designation; Route clustering; Aviation carbon emissions; Efficiency.*

INTRODUCTION

Airspace is the space of air above the surface of the Earth that supports the flight of aircraft and is an important strategic resource for the country (Han 2023). To ensure the safe and orderly flight of a large number of aircraft in the airspace, the civil aviation authorities have authorized "air highways" (Lili 2019), namely airways (Fig. 1). Airways are structured around a linear path connecting individual ground-based navigation facilities, with defined upper and lower limits in terms of both altitude and width. These airway networks are categorized into three tiers: the national hub airway network, the regional trunk airway network, and the regional feeder airway network. Routes refer to a predetermined navigational pathway followed by an aircraft during flight, encompassing both a designated starting point and an endpoint. Routes primarily encompass elements such aircraft flight direction, starting point, endpoint, and any intermediate stopping points, without a specified width limit. On the other hand, air corridors, as described by Yang et al. (2022), are public routes connecting major urban centers

(Lili 2012) where common flight paths converge. These corridors are characterized by being unidirectional, non-intersecting, high-speed aerial pathways, with specific restrictions and priorities designed for efficient long-range travel (Ye et al. 2019). With characteristics including high traffic volume, efficiency, and density (Yaqing et al. 2018), air corridors represent a revolutionary breakthrough in traditional air traffic management practices. Furthermore, they embody a new technological development known as dynamic airspace configuration (DAC) (Ye et al. 2014). The concept of air corridors has gained significant attention as a new approach to airspace resource utilization (Lili 2012; Xue 2009). These corridors are also referred to as highways-in-the-sky, dynamic multitrack airways (DMA), flow corridors or ribbons, and super sectors (Hoffman and Prete 2008), and are designed to group air routes with similar trajectories within a corridor constrained by distance, reserving sufficient airspace for high-density routes (Sridhar et al. 2006). The establishment of air corridors involves determining both the location of the corridor and the participants in the routes. When determining the corridor location, Alipio et al. (2003), Hoffman and Prete (2008), and Yousefi and Zadeh (2013) proposed models based on priority sorting and hierarchical setting, velocity vector fields, and velocity vector clustering, as well as f light delay and cancellation evaluation. Through the identification of candidate airspaces for the corridor and the simulation of the its effectiveness, they developed a relatively complete approach for determining corridor locations based on high-load values and high flight volumes along major air routes. In determining the participants in the air routes, Xue (2009) proposed a method for incorporating more routes with fewer additional flight distances, based on the characteristic that many flights have similar flight trajectories. This method is constrained by three conditions: great circle distance, vertical distance at flight entry and exit, and an additional 5% flight distance. Thus, by determining air corridor locations based on high-traffic routes and including relevant flight participants through distance constraints, the establishment of an air corridor can be effectively completed (Yaqing et al. 2018).

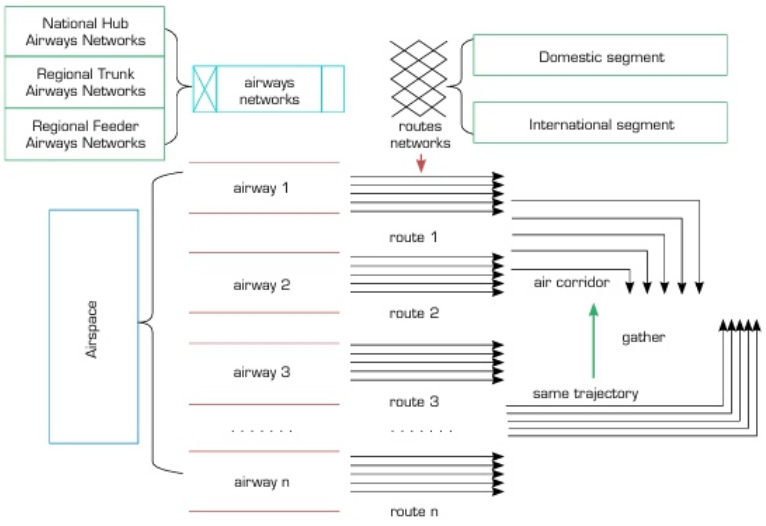

Source: Elaborated by the authors.

Figure 1. Airspace structure diagram.

As the demand for air transportation continues to grow, the problem of insufficient supply capacity in the airspace system has become more noticeable, it is shown in four main aspects: 1) Regional disparities: an imbalance exists in regional development within China's airspace system. Eastern China boasts a dense network of routes, with approximately 90% of the nation's flight traffic concentrated east of the Beijing-Guangzhou air route. In contrast, the airspace in Western and Central China is relatively sparse. However, regional hubs such as Xi'an, Lanzhou, and Urumqi are quite tight on airspace resources (Chen 2022); 2) The expansion rate of airspace infrastructure lags behind the growth rate of the civil aviation industry (Ligang 2015). From 2000 to 2019, China's total civil aviation transportation turnover experienced a significant average annual growth rate of 12.51%. However, despite this growth, the average annual increase in total domestic route mileage, based on unduplicated distance, stands at only 9.65% (Han 2023). While there has been an increasing transfer of military airspace to civilian use in recent years, it remains insufficient to meet the growing demand; 3) Inadequate route design, with multiple routes converging at one point, making route intersections excessively busy (Yang 2023). There are also problems of uneven distribution of trunk and branch routes, poor straightness of flight paths (increasing the path of aircraft), and cut-off roads. It makes the existing air transportation network unable to match the traffic demand, which also creates congestion, and safety issues (Wang et al. 2021); 4) The overall efficiency of airspace utilization requires enhancement. While there have been strides in fine-tuning airspace management (Chen 2011), challenges persist, including disparities in the spatial and temporal distribution of airspace traffic (Han et al. 2019), as well as shortcomings in dynamic airspace allocation (Yaqing et al. 2022).

Studies aimed at optimizing airspace utilization through air corridor analysis primarily concentrate on three key dimensions. Firstly, efforts focus on the identification and delineation of air corridors. The demarcation of these corridors serves multiple purposes, including the evaluation of safe flight zones within the corridor, potential collision trajectory assessment, identification of congested segments, and facilitation of space-time utilization analysis along with its associated benefits (Yousefi and Zadeh 2013). Specifically, the process of pinpointing and outlining continuous high-traffic air corridors necessitates consideration of nine crucial aspects: entrance and exit points, geometrical configuration, all-encompassing locations, accountable entities, utilization prerequisites, operational regulations within the corridor, accessibility parameters, restrictions, and the establishment of a comprehensive pipeline network (Hoffman and Prete 2008). Notably, the dynamic corridors intrinsic to the two major long-distance air highways traversing primary traffic conduits in Europe predominantly reside within a 150-nautical-mile radius of the busiest airports. Consequently, the application of the Hough transform methodology to discern clusters or groups of routes exhibiting congruent trajectories aids in the construction of an airborne "pipeline network." Such a network, characterized by its ability to accommodate heightened traffic volumes compared to linear air corridors, enhances airspace utilization

efficiency, thereby augmenting its inherent value. Secondly, the optimization problem of air corridors, with the overarching objective of mitigating airspace flight complexity (Tian et al. 2019). Air corridor optimization endeavors encompass airspace reconfiguration strategies, notably through the dynamic deployment of air corridors to establish a network of temporally variable flow corridors. Such adaptive configurations confer advantages in terms of average delay, average occupancy, and activation time (Ye et al. 2022). This approach not only facilitates the augmentation of airspace capacity but also engenders reductions in airborne delays, thereby fostering enhanced self-separation control capabilities for aircraft. Notably, a significant portion of US scheduled flights, approximately 33%, are concentrated within a mere 10% of origindestination (O-D) pairs (Ye et al. 2014). Therefore, the deployment of mobility corridors based on the frequency of daily operations between city pairs offers great potential for improving airspace utilization efficiency. However, it is imperative to acknowledge that certain flow corridors cater to only a fraction, approximately 4.05%, of the total traffic demand, indicative of a pronounced coverage deficiency. Through the optimization of air corridors, the amalgamation of actual flight trajectories yields discernible benefits, culminating in a noteworthy 20% reduction in aircraft fuel consumption and an average 4% reduction in aircraft flight time without extending the overall flight duration (Takeichi and Abumi 2016). Thirdly, identifying and assessing potential aircraft collision risks os essential (Zhang and Sherry 2015). The nexus between collision risk and airspace capacity necessitates delineation to mitigate f light conflicts within air corridors, consequently enhancing operational throughput and stability. For instance, the implementation of self-separation algorithms integrating route adjustments and speed modifications (Nakamura et al. 2014) within strip airspaces characterized by constrained widths enables conflict-free aircraft operations within narrow air corridors.

The study of airspace optimization and carbon emission analysis has become a central focus in air traffic management and sustainability research. To ensure both safety and efficiency in air operations, several approaches have been proposed to enhance airspace utilization. Babinski et al. (2024) investigated air traffic safety management in Brazilian airspace using a matrix-based approach to assess perceived safety levels. This study highlights the importance of structuring airspace in a way that optimizes both safety and operational efficiency, which aligns directly with the goals of this work to optimize Chinese airspace. Additionally, Xiang et al. (2023) analyzed airspace capacity improvements and optimization, providing an important foundation for incorporating carbon emission reduction strategies into optimized air corridors. Their work emphasizes the relevance of efficient airspace management to minimize environmental impacts, a theme that is central to this study. To regulate air traffic flow by optimizing airspace structure to match the flow with the capacity of the airspace, the establishment of air corridors is an effective way to form a regular and systematic airspace network structure. In addition, since the allocation of airspace resources has a direct impact on the operational efficiency of air traffic

flows, it also has a direct impact on aviation carbon emission results. Therefore, this study attempts to study to analyze total aviation carbon emissions and the efficiency of the corridors based on improvements to the existing methodology for delineating air corridors in China's airspace. First of all, based on the researched route data, clustering and extraction of routes are carried out to identify air corridors and their route participants. Then, the high-traffic air corridors are determined to analyze the structure of China's existing route network and designate air corridors. Second, the aviation carbon emissions of each corridor are measured and characterized based on indicators such as the number of flights, aircraft type, and aircraft cruise time of each route participant within the delineated air corridors. Finally, the carbon emission efficiency of the seven air corridors is compared and analyzed to justify the existence of air corridors. This study attempts to explore airspace optimization from the perspective of air corridor delineation and to verify the results of delineation for carbon emission reduction. Furthermore, breaking through the limitations of the previous airport-centered aviation point carbon emission research, and actively expand the research perspective on aviation carbon emission. This will provide a theoretical reference for the balanced and rapid development of the national civil aviation industry, enrich the theoretical content of aviation carbon emission research, and assist in promotion of China's 14th Five-Year Plan for green aviation development.

As global climate change becomes an increasingly urgent issue, reducing greenhouse gas emissions has become a critical challenge that governments and businesses worldwide must address. The aviation industry, as one of the significant sources of global carbon emissions, faces tremendous pressure to mitigate its impact. Under the United Nations Framework Convention on Climate Change (UNFCCC), the aviation sector's emission reduction targets have been incorporated into global climate action agendas, with a particular emphasis on reducing aviation carbon emissions in Sustainable Development Goal 13. At the same time, the aviation industry is also an energy-intensive sector, where fuel consumption not only affects operational costs but also has a profound impact on global energy structures and sustainable development. Therefore, optimizing airspace management and designing aviation corridors to improve flight fuel efficiency has become a crucial method for enhancing the aviation industry's energy efficiency and advancing Sustainable Development Goal 7. This research focuses on optimizing China's airspace, aiming to explore how to reduce redundant flight routes, lower fuel consumption during flights, and subsequently decrease carbon emissions in the aviation sector through an air corridor-based aviation optimization model. As one of the largest aviation markets in the world, China accounts for a significant portion of global aviation-related carbon emissions. Therefore, by optimizing China's airspace layout and improving flight fuel efficiency and air corridor fluidity, this study can not only reduce operational costs for airlines in the short term but also make a positive contribution to reducing energy consumption and greenhouse gas emissions both in China and globally. This research not only provides scientific support for Sustainable Development Goal 13 but also offers

practical pathways to achieve Sustainable Development Goal 7 by promoting energy-efficient practices in the aviation industry.

METHODOLOGY

Data sources

The route data used in this paper is mainly based on the research obtained from the FlightAware Big Data platform (https:// map.variflight.com) and the FlightAware website (https://zh.flightware.com). Specifically, route data (excluding Hong Kong, Macao, and Taiwan flights, cargo flights, and international flights) for all airports in China were collected over 4 weeks from January 1st to 28, 2023, taking into account the cyclical characteristics of flight schedules of air carriers. The data includes fields such as the number of flights, aircraft type, operating carrier, connecting city, departure time, arrival time, etc. During data processing, shared f lights were deleted, and direct flight routes were combined with stopover routes, such as decomposing the Dalian-Tianjin-Xining routes into two routes, Dalian-Tianjin and Tianjin-Xining. This was collated to get 5,224 one-way routes with 277,069 flights. For geographic location identification, the coordinate data (latitude and longitude) of all routes involving airports are picked up and entered into the ArcGIS10.4 software with the help of the Baidu map pickup coordinate system as a tool. Furthermore, with the help of ArcGIS 10.4 software, the latitude and longitude coordinate data of the vertical position of the aircraft entering and exiting the air corridor from each airfield point was identified for the distance calculations. When measuring the carbon emission efficiency of aircraft in air corridors, the input-output indicators were selected according to the principles of comprehensiveness, comparability, indirectness, and accessibility, and the carbon emission efficiency was evaluated in the landing and take-off (LTO) and climb, cruise, and descent (CCD) phases, respectively. The input indicators included the number of air corridor route participants, the average flight distance of route participants (km), and the average cruise time of aircraft (s); the desired output indicators included the number of air corridor flights (sorties), while the undesired output indicators included the total amount of carbon emissions from the air corridor (t).

Research methodology

K-means clustering method

This study introduces the K-means clustering method for route clustering analysis. Each route is treated as a data sample. Utilizing the K-means clustering algorithm, all routes are grouped into K different route clusters (ROC) based on similar route directions and smaller Euclidean distances between routes. This aids in identifying route features and their relationships. Referring to previous research on the

structure of domestic scholars' route networks (Ligang 2015; Yaqing et al. 2018), the value of K was determined to be 16 based on the rule of thumb. The K-means clustering method was employed to assign original route samples to K group classes based on the similarity of Euclidean distances between them. This ensured that each sample was closest to the center of its respective group class, resulting in the formation of K groups of ROC. Each group of ROC possesses an ROC centerline.

Air corridor establishment method

The width of air corridors is typically designed to be 7 km (Zhang and Sherry 2015). Currently, two main delineation steps have been proposed by relevant scholars: 1) covering flights with 99.99% of their flight time within 133 km of the corridor centerline and 2) identifying the two-dimensional location of the corridor by combining the Hough transform with a genetic algorithm. Routes with an additional flight distance ratio of ≤ 5% are identified as route participants in the air corridor (Xue 2009). enhances the air corridor delineation method from existing literature (Yaqing et al. 2018), taking into account the characteristics of the research subjects. To encompass more route participants, routes with a distance-to-extra-flight ratio (dextra) ≤ 10% are considered as route participants in the corridor.

Initially, ROC centerlines of longer than 600 km were extracted using the K-means clustering method to determine the air corridor locations. Then, the additional flight distance for each route was calculated based on great-circle flight trajectory distances for aircraft entering and exiting the air corridor vertically at an airport point, aircraft flying in the air corridor, and routes before the delineation of the air corridor. Routes with dextra ≤ 10% were included in the air corridor. The air corridor was named according to the most frequented routes within the ROC. It extended from the centerline of the initially selected ROC to the last airport with routes joining the air corridor, following a great circle trajectory to complete the air corridor establishment. Then, the additional flight distance for each route (dextra):

$$d_{\text{extra}} = \frac{(d_1 + d_2 + d) - D}{D} \times 100\% \quad (1)$$

where dextra represents the extra flight distance ratio, d1 and d2 represent the great-circle flight trajectory distances for flights entering and exiting the air corridor vertically, respectively, d represents the great-circle flight trajectory distance on the air corridor, and D represents the great-circle flight trajectory distance before the air corridor is delineated. Taking D as an example, the calculation formula is as follows:

$$D = R * \arccos\left(\cos(latA)\cos(latB)\cos(longB - longA) + \sin(latA)\sin(latB)\right) \quad (2)$$

where R is the radius of the earth (6,371 km) latA, longA and latB, and longB are the latitude and longitude for points A and B, respectively (Fig. 2), the latitudinal and longitudinal coordinates of the vertical positions of entering and exiting the air corridor, respectively, and d1, d2, and d are computed in the same way as D.

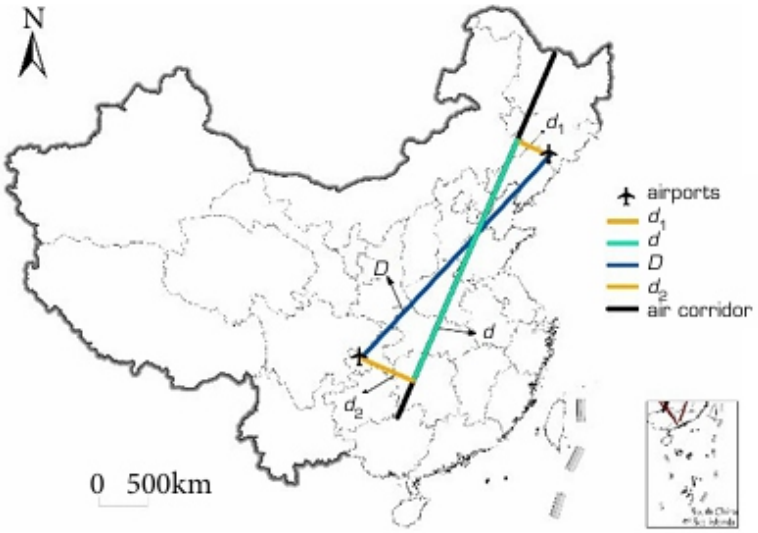

Source: Elaborated by the authors.

Figure 2. Schematic diagram of d, d_1, d_2, and D flight paths and air corridors.

Aircraft carbon emissions measurement method for different flight phases

The International Civil Aviation Organization (ICAO) divides the entire flight process of an aircraft into the LTO and CCD phases. Previous studies have found that aviation fuel consumption and CO2 emissions primarily occur below 1 km and between 8-12 km (Jun 2022). This paper calculates carbon emissions during the LTO and CCD phases of flights based on the ICAO standard emission calculation model and the carbon emission accounting model for the CCD phase.

• LTO phase carbon emissions calculation methodology

Carbon emissions from aircraft flying through air corridors are measured based on aircraft engine type data using a "bottom-up" methodology based on operational data established by ICAO. The ICAO has calibrated the duration of operation for each phase of the aircraft LTO phase as follows: take-off (0.7 min), climb (2.2 min), approach (4 min), and taxi (26 min) (Lu et al. 2018), with the following equations:

$$F_i = \sum_j T_{ij} \cdot R_{ij} \cdot N_i \quad (3)$$

$$E_{LTO} = \sum_i F_i \cdot I \cdot n_i \quad (4)$$

where i is the aircraft type, j is the four different phases of LTO operation, Fi is the fuel consumption (kg) of a category I aircraft during LTO, Rij is the fuel consumption rate (kg·s) of a engine of aircraft of category i in phase j, Ni is the number of engines of aircraft of category I, Tij is the operating time of aircraft of category i in phase j (s), ELTO is the carbon emission of aircraft in LTO phase (kg), I is the fuel carbon emission coefficient, which is a constant of 3.15 (kg/kg) (Liu et al. 2019), and ni is the LTO of aircraft of category i cycle total number (min). • CCD phase carbon emission calculation methodology T he aircraft's engine settings vary at each phase of flight. The ICAO Engine Emissions Database Attachment 16 provides specific thrust parameters, with engine thrust values of 100, 85, 65, 30, and 7%

for take-off, climb, cruise, approach, and taxi phases, respectively. By fitting a binomial equation to the thrust-specific fuel consumption data and performing interpolation, the fuel flow rate for aircraft engines at 65% thrust during each LTO phase can be derived. This enables the calculation of carbon emissions during the CCD phase of an aircraft.

The formula is as follows:

$$T_{CCD} = T_{TOTAL} - T_{LTO} \tag{5}$$

$$E_{CCD} = N_{CCD} F_{CCD} I \tag{6}$$

where, TCCD, TTOTAL, and TLTO are the operating time (s) of the CCD phase, full flight process, and LTO phase of an aircraft, respectively, ECCD is the carbon emission (kg) of CCD phase of an aircraft, N is the number of engines of an aircraft, FCCD is the fuel flow rate of an engine of an aircraft in the CCD phase (kg·s), and I is the fuel carbon emission coefficient, which is a constant 3.15 (kg/kg) (Liu et al. 2019). Aviation CO2 emission factors Aviation CO2 emission factors represent the CO2 emissions per unit flight kilometer of an aircraft type (Lyu et al. 2022) and serve as an important criterion for determining carbon emissions. The formula is as follows:

$$X_i = (E_{i/LTO} + E_{i/CCD})/L \tag{7}$$

where Xi is the aviation CO2 emission factor (kg·km), Ei/LTO and Ei/CCD are the carbon emissions in the LTO and CCD phases of aircraft of category i, respectively, and L is the flight mileage of the aircraft (km).

SBM model of super-efficiency based on undesired outputs

In traditional efficiency evaluation models, usually only desired outputs are considered, such as corporate profits or product quantities. However, in the actual production process, there will also be undesired outputs, such as pollutant emissions, energy waste, etc. The super-efficiency slacks-based measure (SBM) model based on undesired outputs is designed to evaluate the efficiency of decision-making units (DMUs) more comprehensively and accurately, especially in the presence of undesired outputs. It is an efficiency evaluation model based on slack variables, which is non-radial and non-angular. It measures efficiency by taking into account the slack variables for inputs, desired outputs, and undesired outputs. Compared with the traditional data envelopment analysis (DEA) model, the SBM model can handle the non-proportional changes in inputs and outputs as well as the problem of undesired outputs more effectively.

Specifically, in the super-efficiency SBM model based on undesired outputs, the concept of input is as follows: input refers to the resources required in the production or service process, and these resources usually have an impact on outputs – the input indicators used in this paper are the number of air routes in

the corridor, the flight volume, and the average distance of route participants; desired output: this is the output that is expected to be increased as much as possible in the model, representing positive results – the desired output indicator used in this paper is the average cruising time of the air routes in the corridor. undesired output: this is the result that is not desired or is hoped to be minimized as much as possible in the production process, usually an environmental burden, such as carbon emissions, exhaust gas, etc. – the undesired output indicator used in this paper is the carbon emissions of the corridor. T he non-radial slacks-based variable super-efficiency SBM model is selected to measure the efficiency of aircraft carbon emissions in air corridors. It incorporates slack variables in the objective function, which effectively solves the problem of slackness of input and output variables when air corridor aviation carbon emissions are used as an undesired output indicator for efficiency evaluation (Tone 2001).

RESULTS

Results of air corridor establishment

Route cluster aggregate results

China's route network exhibits a diamond-shaped three-dimensional structure. Utilizing the K-means algorithm, 16 groups of ROC were identified, numbered from 0 to 15 (Figs. 3 and 4 and Table 1). Air corridors were delineated and located based on the centerlines of these 16 ROC groups. As the centerline length of ROC 1 and 4 is shorter than 600 km, they were not considered for reference. Upon examining the distribution characteristics of the remaining 14 ROC groups and their centerlines, a noteworthy observation emerged: the centerlines of ROC roughly coincide with the location of other ROC. Consequently, the centerlines of overlapping ROC merged to form a diamond-shaped structure (Fig. 5).

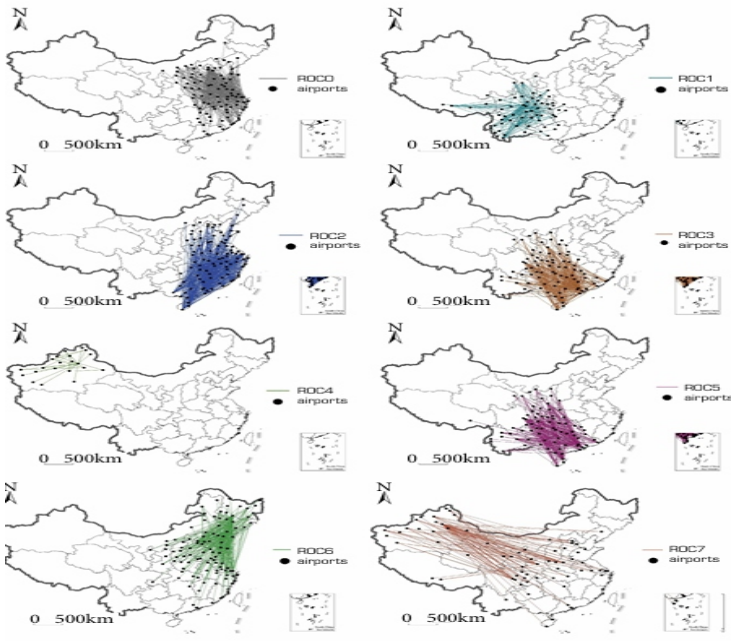

Source: Elaborated by the authors.

Figure 3. ROC 0-7 and their including airports.

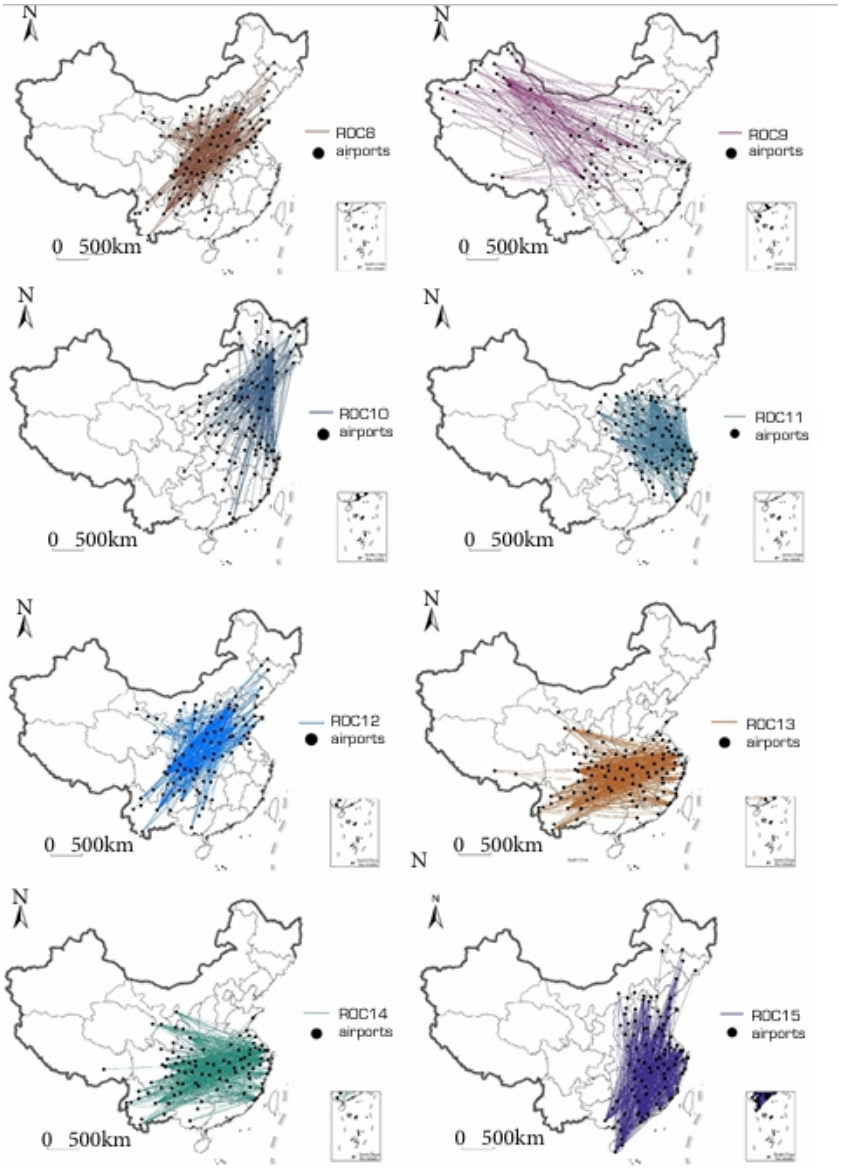

Source: Elaborated by the authors.

Figure 4. ROC 8-15 and their including airports.

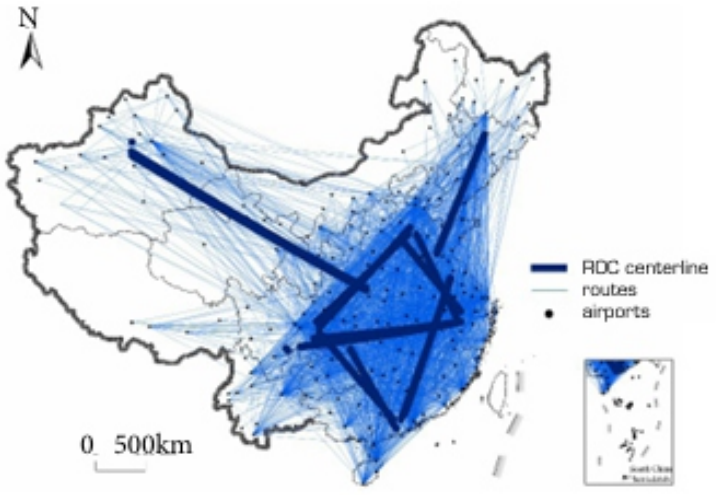

Source: Elaborated by the authors.

Figure 5. ROC centerline diamond-shape structures.

Table 1. Length of each ROC centerline and the number of routes in the ROC.

ROC groups	Distance of ROC centerline/km	Number of routes	Number of flights
ROC0	846	442	20,287
ROC1	28	335	14,975
ROC2	1140	526	34,449
ROC3	785	368	19,300
ROC4	3	58	2,658
ROC5	977	282	15,483
ROC6	1062	315	15,669
ROC7	2430	107	5,270
ROC8	1119	350	13,975
ROC9	2410	116	5,465
ROC10	1147	289	14,951
ROC11	829	443	4,884
ROC12	1190	325	13,916
ROC13	1328	368	22,416
ROC14	1277	397	24,869
ROC15	1236	502	33819

Source: Elaborated by the authors.

Table 2 shows the centerlines of the five groups of ROC that form the diamond-shaped structure and their connecting areas.

Table 2. The centerline of the five groups of ROC that form the diamond-shaped structure and their connecting regions.

ROC centerline group	Connect regions
ROC0 & ROC11	Beijing-Tianjin-Hebei Airport Cluster-Yangtze Delta Airport Cluster
ROC2 & ROC 15	Yangtze Delta Airport Cluster-Guangdong-Hong Kong-Macao Greater Bay Area Airport Cluster
ROC3 & ROC 12	Beijing-Tianjin-Hebei Airport Cluster-Chengdu-Chongqing Airport Cluster
ROC5 & ROC 8	Chengdu-Chongqing Airport Cluster-Guangdong-Hong Kong-Macau Airport Cluster
ROC13 & ROC14	Yangtze Delta Airport Cluster-Chengdu-Chongqing Airport Cluster

Source: Elaborated by the authors.

The four vertices of the diamond are situated in Beijing-Tianjin-Hebei, the Yangtze River Delta, the Guangdong-Hong Kong-Macau Greater Bay Area, and Chengdu-Chongqing. This indicates that airports within and between these four major urban areas in China experience more intense air traffic and serve as key clusters and connecting corridors within the domestic aviation network. The results are consistent with studies that have been done (Yang et al. 2022). China's route network covers about half of the country's cities in terms of routes distribution. The framework of a broad spatial connectivity network was essentially established on a national scale, and the main lines of the network consist primarily of long-distance lines connecting different regional economic hubs. Table 3 shows the coordinates and connection locations of the centerline vertices of the remaining two sets of ROC. The two ROC effectively connect the above rhomboid structure to northwest and northeast China, forming a

trans-regional air trunk community. This will promote the balanced development of the aviation network layout in China. Additionally, the project will significantly enhance inter-regional economic and trade exchanges, supporting the advancement of national strategies such as the Belt and Road Initiative and the revitalization of the northeastern region of the country.

Table 3. The coordinates of the centerline of the outer ROC of the diamond-shaped structure and its connecting region.

ROC centerline	Vertex coordinates 1	Vertex coordinates 2	Direction	Connect regions	Connect regions
ROC7	(85.49E, 42.67N)	(110.67E, 33.09N)	Northwest-southeast	Xinjiang Autonomous Region	Shaanxi province
ROC9	(110.68E, 33.28N)	(85.74E, 42.37N)			
ROC6	(124.93E, 43.51N)	(117.85E, 35.35N)	Northeast-southwest	Heilongjiang province	Shandong province
ROC10	(119.97E, 35.60N)	(125.31E, 43.93N)			

Source: Elaborated by the authors.

Results of air corridor establishment

Seven air corridors have been delineated within China's airspace based on the research route data, primarily located in the area to the east of the Hu Line (Fig. 6). The longest distance centerline was selected from the centerlines of the two overlapping ROC and the short line routes in the corridor were merged with the long line routes. Finally, seven ROC mid-lines, ROC0, ROC5, ROC7, ROC10, ROC12, ROC13, and ROC15, were identified as the basis for air corridor delineation and the approximate locations of the seven air corridors were determined. Afterward, extending the initial ROC centerline positions along great circle trajectories towards both ends until reaching the last airport with a route incorporated into the air corridor constitutes the establishment of the air corridor. It shall be named after the route within the ROC with the highest traffic volume. T he seven designated air corridors include the Harbin-Changsha, Harbin-Haikou, and Beijing-Chongqing corridors in the Northeast-Southwest, the Chongqing-Zhuhai, Urumqi-Hangzhou, and Beijing-Fuzhou corridors in the Northwest-Southeast, and the Shanghai-Chongqing corridor in the East-West. The Harbin-Changsha corridor is the highest frequency corridor among the seven corridors, averaging 131 flights per routes (Table 4), and Chongqing-Zhuhai is the lowest frequency corridor, averaging 39 flights per routes. The Urumqi-Hangzhou corridor is the longest average flying distance of the seven corridors, and the Chongqing-Zhuhai corridor is the shortest average flying distance.

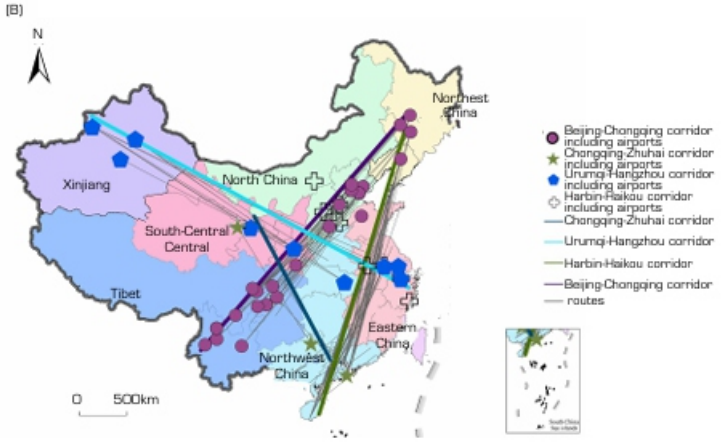

Source: Elaborated by the authors.

Figure 6. Location of the seven air corridors and their including airports.

Table 4. List of airports included in each air corridor.

Air corridors	Number of flights	Average number of flights per air routes	Includes airports
Chongqing-Zhuhai	352	39	BHY, DZH, KOW, CAN, KWL, HAK, SWA, JGS, MXZ, NNG, HSC, XNN, ZHA, CKG, ZUH
Beijing-Fuzhou	749	62	PKX, PEK, FOC, HDG, HGH, HFE, HET, TNA, NKG, JUZ, SJW, TYN, WNZ, XUZ
Urumqi-Hangzhou	630	63	HGH, KRL, LHW, NKG, NNY, SHF, WUX, URC, WUH, XIY, YIN
Shanghai-Chongqing	1,888	76	BFJ, CTU, TFU, HGH, TXN, LZY, LZO, KHN, NGB JIQ, JUZ, PVG, HYN, WUH, XIC, YBP, YIW, YYA, CKG, CQW, WMT, ZYI
Harbin-Changsha	3,676	131	DLC, XUZ, LYG, JNZ, SHE, CGQ, DQA, EHU, YNT LYI, WEF, HRB, WUH, HNY, HFE, RIZ, TAO, LDS
Beijing-Chongqing	2,849	73	AKA, BSD, PKX, CTU, TFU, DZH, DLU, HRB, HDG TNA, KMG, LJG, LZO, NAO, SHE, WDS, SJW, YSQ TVS, TSN, XIC, YBP, CGQ, CIH, ZAT, CKG, WMT
Harbin-Haikou	6,041	93	AQG, JUH, DLC, FUO, KOW, CAN, HRB, HAK, HFE HIA, SWA, JGS, JDZ, LYG, LYI, LCX, KHN, NKG, TAO, BAR, JJN, RIZ, SYX, HSC, SZX, SHE, WEH WEF, WHA, XUZ, YNT, YNZ, CGQ, CSX, ZUH
Total	16,185	-	-

Source: Elaborated by the authors.

Air corridor structure and element characterization

The seven designated air corridors exhibit a "diamond-shaped three-dimensional structure," with the Beijing-Tianjin-Hebei Airport Cluster, Yangtze River Delta Airport Cluster, Guangdong-Hong Kong-Macao Greater Bay Area Airport Cluster, and Chengdu-Chongqing Airport Cluster forming the apex. Among them, the edges that form the diamond-shaped structure are Beijing-Fuzhou, Beijing-Chongqing, Chongqing-Zhuhai, and Harbin-Haikou, with Shanghai-Chongqing serving as its central line. The five corridors are all located east and south of the Hu Line, encompassing 158 routes and 12,706 flights, which account for 80.6% of the total routes and 78.5% of the total flights among the seven corridors. This indicates that China's aviation network layout is closely tied to population and urban distribution, reflecting the national air traffic control capability of core airport clusters (Wang and Fengjun 2019). However, in terms of airport coverage, the Western region boasts the highest number of

airports, followed by the Eastern, Central, and Northeastern regions of China. This can largely be attributed to the remarkable growth in airport numbers in the West from 2000 to 2019. According to Shuyan et al. (2023), the number of airports in these regions experienced growth rates of 118.2, 19.6, 50, and 107.7%, respectively. Specifically, the pace of airport construction in the West accelerated significantly after 2005, resulting in more than 50% of the country's airports being located in this region by 2019. T his surge in airport infrastructure not only enhances connectivity within the Western region but also strengthens ties between the West and other regions, thereby further promoting the development of the regional aviation industry. Urumqi Diwopu Airport, playing a central role in the Western region, hosts a multitude of linear airports offering a diverse array of air services. T he region has fostered a dispersed aviation layout radiating outward from a single core, thereby facilitating the establishment of the Urumqi-Hangzhou air corridor.

The seven corridors exhibit variations in the number of airports they encompass (Table 2). The Beijing-Fuzhou corridor connects 14 airports spanning North and East China. The Chongqing-Zhuhai corridor links 15 airports across the Southwest, Northwest, Central-South, and East China regions. The Urumqi-Hangzhou corridor links 12 airports in Xinjiang, the Northwest, South-Central, and East China regions. The Harbin-Changsha corridor connects 20 airports in the Northeast, East China, and South-Central regions. The Beijing-Chongqing corridor interconnects 28 airports across the Northeast, North, Northwest, and Southwest regions. The Shanghai-Chongqing corridor serves 23 airports in the Southwest, Central

South, and East China. Finally, the Harbin-Haikou corridor interlinks 35 airports in the Northeast, North, East, and South Central regions. Notably, the Harbin-Haikou corridor boasts the highest number of airports and flights among the corridors, traversing much of Eastern China.

The seven air corridors exhibit significant disparities in the number of participating routes. Specifically, the Harbin-Haikou corridor boasts the highest number of participating routes, with 65 routes (Tables 3 and 4), and the largest total flight volume, totaling 6,041 flights. Within this corridor, there are 12 routes with flight volumes exceeding 100 flights (bi-directional), HRB-HAK, CAN-SHE, CAN-YNT, CAN-TAO, HAK-NNG, SYX-SHE, SYX-NNG, SZX-SHE, SZX-TAO, SHE-ZUH, CGQZUH, and CGQ-SYX. Among these, the Harbin-Haikou corridor stands out as the corridor with the widest latitude span within Chinese airspace. Its participants primarily operate medium-haul routes, with an average distance of 1,828 km. Long-haul routes are favored by routes due to their higher profitability (Shuyan et al. 2023), and air travel is increasingly preferred by passengers due to its high efficiency and minimal susceptibility to ground conditions. With the growing prevalence of the "migratory bird" retirement model and the exacerbation of aging populations in Northeast China, the proportion of individuals aged 60 and above in the three Northeastern provinces exceeded 20% in 2021 (National Bureau of Statistics of China 2021). Consequently, more elderly individuals are opting for retirement destinations with

superior climates and environments, such as Sanya and Haikou in Hainan, Guilin and Nanning in Guangxi, and Zhuhai and Shenzhen in Guangdong (IIR-SJTU 2022). Additionally, the organization of regional tourism events influences aviation transport layouts (Wang and Jingjuan 2016). For instance, in January 2023, the Harbin International Ice and Snow Festival attracted 23,394 million visitors, resulting in an 18.2% increase in total flight operations and a 49.4% increase in completed passenger throughput at Harbin Taiping International Airport compared to the previous year (Shuyan et al. 2023).

The Chongqing-Zhuhai corridor has the fewest participating routes and the lowest flight volume. Among these, only the Chongqing-Zhuhai route has a flight volume exceeding 100 flights (bi-directional), while the flight volumes of other routes are all less than 50 flights. This is primarily due to the corridor's participants operating short-haul routes, with an average length of 963 km, such as BHY-CAN (485 km), SWA-HAK (857 km), MXZ-ZHA (763 km), KOW-NNG (941 km), NNG-HSC (679 km), etc. The expansion of the high-speed rail network has exerted pressure on the aviation network, with high-speed rail gradually becoming the dominant mode of transportation within a 1,500 km range (Yang et al. 2022). Consequently, passengers have a greater number of cost-effective alternative transportation options such as high-speed rail, trains, and buses, leading to a lower frequency of air transportation for short-distance journeys.

After the establishment, the flight density of individual routes within the corridors increased, accommodating more flights than before the establishment. The average flight density of single routes within the Harbin-Haikou corridor increased by 1.44% after the establishment, with an average increase of 17 flights per route. Similarly, the Harbin-Changsha corridor saw increases of 3.40% and 80 flights respectively. The Beijing-Chongqing corridor witnessed increases of 2.41% and 30 flights respectively. The Shanghai-Chongqing corridor saw an increase of 2.90%. The Beijing-Fuzhou corridor saw increases of 8.22% and 17 flights respectively. The Urumqi-Hangzhou corridor saw increases of 9.55% and 15 flights respectively. The Chongqing-Zhuhai corridor saw the highest increase in flight density after the establishment, with a growth rate of 10.95%. Among these, the Chongqing-Zhuhai corridor experienced the highest growth rate in flight density of individual routes after the establishment, while the Harbin-Changsha corridor witnessed the largest increase in the average number of flights per route. This is mainly attributed to the relatively low number of participating routes and higher flight volumes within these corridors, resulting in increased flight density and growth rates of both percentage and absolute numbers after the establishment.

Results of carbon emission measurement for air corridors

Air corridor carbon emissions analysis

During the study period, aviation carbon emissions in the seven air corridors totaled 619,431 metric tons. The Harbin-Haikou corridor recorded the highest emissions, while the Chongqing-Zhuhai

corridor reported the lowest, with a 17-fold difference between the two (Table 5). Strong correlations exist between emissions and the number of route participants, flights, and types of aircraft in each corridor. The average carbon emissions across the seven air corridors were 88,490 tons. The Harbin-Haikou, Harbin-Changsha, and Beijing-Chongqing corridors exceeded the average carbon emissions by 138, 77, and 13%, respectively. Conversely, the Chongqing-Zhuhai, Urumqi-Hangzhou, Beijing-Fuzhou, and Shanghai-Chongqing corridors fell below 86, 72, 67, and 1% of the corridor's average carbon emissions, respectively

Table 5. CO_2 emissions from seven air corridors.

Air corridors	Total CO_2 emissions/t	LTO phase CO_2 emission s/t	CCD phase CO_2 mission s/t	Average flight distance of route participants/km	Average cruise time of route participants/s
Harbin-Haikou	209,540	17,340	192,200	1,828	7,451
Harbin-Changsha	156,697	10,581	145,748	1,467	8,517
Beijing-Chongqing	99,921	9,127	90,790	1,936	7,332
Shanghai-Chongqing	87,520	5,617	81,843	1,581	7,867
Beijing-Fuzhou	29,067	2,032	27,035	1,345	7,143
Urumqi-Hangzhou	24,650	2,417	22,234	2,971	8,129
Chongqing-Zhuhai	12,257	992	11,257	963	7,271
Total	619,431	48,106	571,107	-	-

Source: Elaborated by the authors.

The Harbin-Haikou corridor exhibits the highest aviation carbon emissions. This is primarily attributed to its highest number of route participants and flights. Additionally, the average distance of routes operated by participants in this corridor is 1,828 km, ranking third among the seven corridors. During the CCD phase, the average aircraft's cruise time is 7,451 s, resulting in an average carbon emission rate of 26 tons per second. Furthermore, 59% of the routes in this corridor utilize medium-sized aircraft suitable for medium to long-haul flights (Table 6), such as the Airbus A320 series (including Airbus A318, Airbus A319, and Airbus A320) and the Boeing 737 series (including Boeing 737-700, Boeing 737-800, and Boeing 737900), with 4,228 and 1,929 flights respectively. The average CO2 emission factor for medium-sized aircraft operating within their route intervals during the study period reached 27.1 kg CO2·km. Some medium-haul routes exceeding 2,000 km in length utilize large-sized aircraft such as the Airbus A330 series (including Airbus A330-200 and Airbus A330-300) used for 98 flights, and the Boeing 787 series (including Boeing 787-8 Dreamliner and Boeing 787-9 Dreamliner) utilized for 24 flights. During the study period, large-sized aircraft exhibited an average CO2 emission factor of 32.7 kg CO2·km within their route intervals. Large-sized aircraft, due to their longer range, heavier weight, and higher passenger capacity, have relatively higher engine fuel consumption rates, resulting in significantly higher CO2 emission factors compared to medium and small-sized aircraft. The Airbus series and Boeing series of large-sized aircraft recorded average CO2 emission factors of 41 kg Co2·km and 34 kg CO2·km within their route intervals, respectively, representing 1.28 and 1.42 times the CO2 emission factors of medium-sized aircraft within the same series. The aviation carbon emissions in the Chongqing-Zhuhai corridor totaled only 12,099 tons, primarily due to its minimal number of route

participants and flights. The average route length for participants in this corridor was 963 km, and the aircraft cruise time and distance were relatively short. The corridor predominantly utilized medium and small-sized aircraft, such as the A320 series with 228 flights and the B737 series with 109 flights, along with a few other small-sized aircraft totaling four flights.

The trend of total air corridor carbon emissions aligns with aircraft CCD phase carbon emissions (Fig. 7). Despite operating in the stratosphere where encountering low drag, slow airflow, and complex weather is more challenging, the maximum engine thrust has been reduced to 34%, resulting in relatively low CO2 output per kilometer. The LTO phase entails more complex operating conditions compared to the CCD phase, characterized by the engine operating at maximum thrust and higher fuel consumption rates. Fuel consumption rates during take-off and climb processes were approximately 2.6 to 3.4 times and 2.0 to 2.8 times higher than those during the CCD phase were. However, due to the short flight duration of the LTO phase, its impact on overall air corridor carbon emissions is not significant. Additionally, the CO2 emission factor for a single type of aircraft decreases as the distance flown increases (Fig. 8). The CO2 emission factor for an aircraft operating at maximum range is reduced by 40.52 to 88.57% compared to that at minimum range. This reduction can be attributed to the fact that long-distance flights typically operate at higher cruising altitudes and speeds, where air density is lower, resulting in reduced drag and increased flight efficiency.

Table 6. CO_2 emission factors for different aircraft types.

Aircraft category	Aircraft type	Minimum flight range/km	CO_2 emission factor / kg·CO_2/km	Maximum flight range /km	CO_2 emission factor / kg·CO_2/km	Average CO_2 emissions during the flight/CO_2·km
Large	A330	1,470	50	3,489	21	41
	A332/A333	1,234	20	3,441	9	13
	B788/B789	1,215	41	3,039	16	34
Medium	A19N/A20N/A21N	619	48	3,489	17	23
	A319/A320/A321	485	67	3,319	12	37
	B736/B737/B738/B739	702	34	3,435	10	23
	B73G	1,106	25	3,395	8	16
	B732	752	34	3,039	10	23
	B733/B735	752	43	2,309	14	27
Small	E190	857	24	1,989	11	16
	CRJ9	935	24	1,572	14	19
	AJ27	752	42	1,526	19	28

Source: Elaborated by the authors.

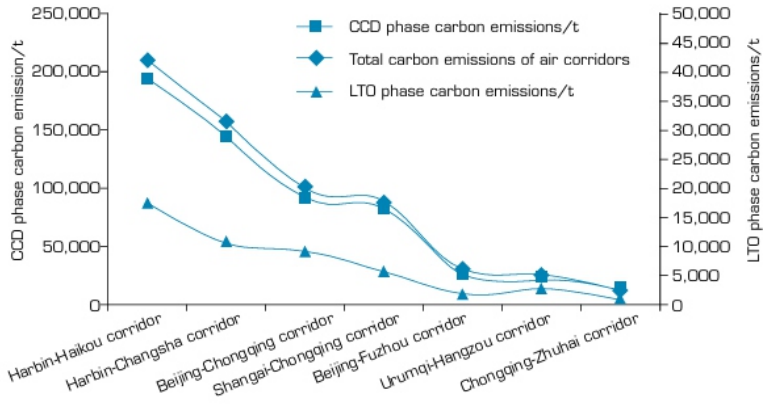

Source: Elaborated by the authors.

Figure 7. Comparison of carbon emissions in LTO and CCD phases.

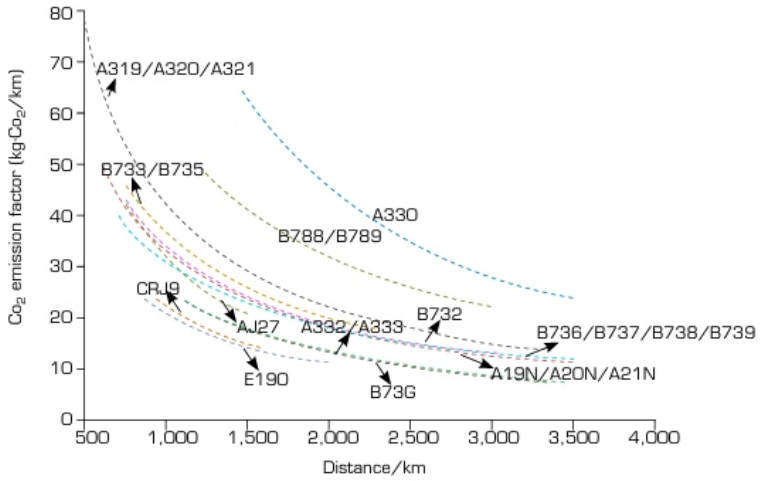

Source: Elaborated by the authors.

Figure 8. The variation of the CO_2 emission factor with mileage for different aircraft types is shown.

Comparison and analysis of carbon emission efficiency in established air corridors

• Two air corridors are operating at high-efficiency levels, namely the Harbin-Haikou corridor and the Harbin-Changsha corridor (Fig. 9), both with efficiency values of 1. This is primarily due to the long average distances flown by participants in these corridors (1,828 km for the Harbin-Haikou corridor and 1,476 km for the Harbin-Changsha corridor), as well as the extended cruise times (7,451 s for the Harbin-Haikou corridor and 8,517 s for the Harbin-Changsha corridor). Based on the results of calculating CO2 emission factors for different aircraft types (Table 4), it is evident that longer flight distances result in lower CO2 emissions per unit distance flown. However, the overall carbon emission efficiency of the participants within these corridors remains high. After the establishment of the Harbin-Haikou corridor and the Harbin-Changsha corridor, the average distances flown by participants increased by 453 km and 207 km respectively compared to before the establishment. The average cruise times of aircraft decreased by 125 s and 1,125 s respectively, indicating that after establishment, the average flight speeds of aircraft within these corridors have increased compared to before establishment, which is the main reason for maintaining high carbon emission efficiency.

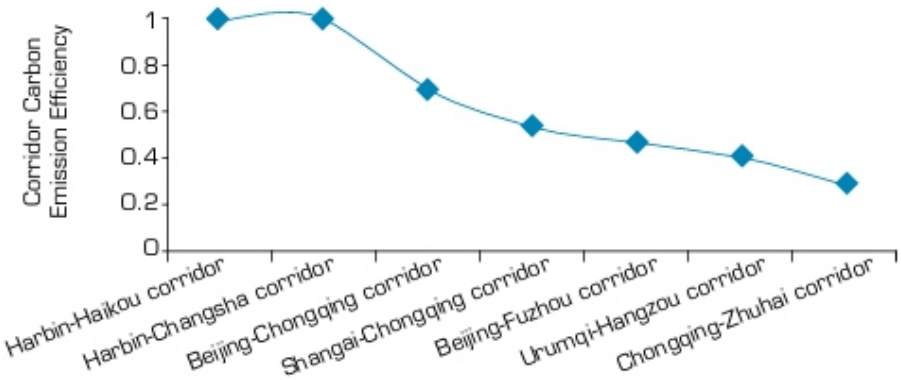

Source: Elaborated by the authors.

Figure 9. Corridor carbon emission efficiency.

• Two air corridors, the Beijing-Chongqing corridor and the Shanghai-Chongqing corridor, are operating at a moderate efficient level, with efficiency values of 0.701 and 0.531 respectively. Post-establishment, the average distances flown by participants in these corridors increased by 585 km and 88 km, respectively, compared to before establishment. However, the average cruise times of aircraft decreased by 330 s and 251 s, respectively. This indicates that post-establishment, aircraft within these corridors are flying at faster speeds compared to pre-establishment levels, resulting in lower carbon emissions per unit of time and higher carbon emission efficiency.

• Two air corridors, the Beijing-Fuzhou corridor and the Urumqi-Hangzhou corridor, are operating at levels, with efficiency values of 0.464 and 0.406, respectively. This is primarily due to the increased average distances flown by participants in these corridors post-establishment. The Beijing-Fuzhou corridor saw an increase of 290 km, while the Urumqi-Hangzhou corridor saw an increase of 341 km. When the average cruise time of aircraft within a corridor remains constant, longer flight distances result in higher carbon emissions, leading to decreased carbon emission efficiency.

• The Chongqing-Zhuhai corridor stands out for its exceptionally very low efficiency, registering at 0.289, making it the least efficient corridor among the seven. This inefficiency primarily stems from the post-establishment increase in the average cruise time of aircraft within the corridor, which rose by 733 s compared to pre-establishment levels. With prolonged cruise times, aircraft emit more carbon, resulting in a notable decline in the corridor's carbon emission efficiency.

DISCUSSION

The increasing air traffic flow has led to issues regarding airspace resource utilization and aviation carbon emissions, which remain major challenges for China's aviation industry. These issues not only affect civil aviation operational safety but also relate to the industry's green development (Yinuo et al. 2019). In terms of airspace utilization, air traffic demand in China is primarily concentrated in the eastern and southern regions, which together account for 31% of the country's total area but 74% of the population and approximately 75% of the aviation demand. Although a dense network of flight routes has been established in these areas, the total available airspace is limited, leading to excessively high flight density in corresponding airspace and flight routes, especially during peak periods. This has increased the probability of flight delays and put pressure on air traffic control, particularly in major hub cities and economically developed regions. In areas such as the Beijing-Tianjin-Hebei region, the Yangtze River Delta, and the Greater Bay Area, where airport clusters are located, frequent flight take-offs and landings result in a supplydemand mismatch in airspace resources, and their usage mutually impacts one another. In addition to the increased demand during holidays, the summer period is also often affected by severe convective weather, which tends to cause delays in major flight routes (Ran et al. 2024). For example, on August 16, 2024, due to heavy rain in Guangzhou, flights could not land,

resulting in varying degrees of take-off delays across the entire Beijing-Guangzhou air corridor. Some were delayed by up to 3 hours, affecting the normal utilization of airspace in at least eight provinces in China. Meanwhile, airspace in Central and Western regions remained largely unused. Regarding aviation carbon emissions, China has been the world's secondlargest civil aviation market since 2005, following the United States. As the national economy continues to grow steadily, aviation demand is expected to rise, leading to a corresponding rigid increase in aviation carbon emissions. On a global scale, there is no significant difference between countries in terms of single-aircraft emission reductions. The long update cycle for aviation engine technology and the high cost of sustainable aviation fuels make it difficult to achieve significant emission reductions in the short term. As a responsible major country committed to sustainable development, China pledged at the 75th United Nations General Assembly in 2020 to peak carbon emissions by 2030 and achieve carbon neutrality by 2060. Therefore, carbon reduction in the aviation sector is a key issue in achieving the national dual-carbon goals. T he Chinese government and civil aviation authorities have proposed a series of relevant policies to address the current airspace issues and mitigate the challenges faced. The 2017 Government Work Report specifically mentioned the need to further optimize the national airspace resource allocation, improve airspace resource utilization, expand civil aviation usage areas, and promote airspace reform. In 2021, the Civil Aviation Administration of China (CAAC) released the 14th Five-Year Plan for Civil Aviation Development, which proposed improvements to the airspace management system and modernization of the air traffic management system, including optimizing flight route networks and enhancing air traffic control service capacity. This plan set the general direction and objectives for efficient air corridor operations and airspace optimization. To address the existing aviation carbon emission pressures, the CAAC released the 14th Five-Year Plan for Green Development of Civil Aviation in 2022. The overall goal for civil aviation development is to achieve phased results in green transformation by 2025 and establish a green, and circular development system by 2035. By then, the aviation industry aims to achieve carbon-neutral growth in air transport and become a global leader in sustainable civil aviation development. Therefore, given the growing demand potential of China's civil aviation market, achieving green transformation and full decarbonization within a tight timeframe will be a challenging and complex task.

This study integrates airspace resource optimization with the issue of aviation carbon emissions. By identifying the structure of China's aviation network, it delineates air corridors and validates the delineation results from the perspective of carbon emissions. Unlike previous studies, which have focused largely on technical aspects of aviation carbon reduction, this research explores carbon reduction from the perspective of airspace resource management. Finding the optimal decarbonization path through non-technical means is a key innovation and contributes to the theoretical exploration of green development in the civil aviation industry. Furthermore, while past research has predominantly

approached the issue from the perspective of airport terminals, focusing on congestion in the terminal areas and carbon emissions during the LTO phase, this study expands the research to include the optimization of airspace linear network structures and carbon emissions throughout the entire flight phase. By validating the research's content from the angle of carbon emissions, it aligns more closely with societal development expectations.

CONCLUSION

The research findings are divided into two main parts:

• Based on the assessment of China's airspace structure, this study aims to optimize airspace resource utilization. Seven air corridors are delineated across China based on the positions of flight ROC, incorporating a total of 196 routes and 16,185 f lights. The seven corridors are as follows: Chongqing-Zhuhai corridor, Beijing-Fuzhou corridor, Urumqi-Hangzhou corridor, Harbin-Changsha corridor, Beijing-Chongqing corridor, Shanghai-Chongqing corridor, and Harbin-Haikou corridor. Among these, the Harbin-Haikou corridor has the most route participants and flight volumes, while the Chongqing-Zhuhai corridor has the fewest. The Harbin-Haikou corridor also has the highest flight frequency, and the Urumqi-Hangzhou corridor has the longest average flight distance for participants. The seven delineated air corridors collectively form a "diamond-shaped threedimensional structure," with the Beijing-Tianjin-Hebei airport cluster, Yangtze River Delta airport cluster, Guangdong-Hong Kong-Macau Greater Bay Area airport cluster, and Chengdu-Chongqing region airport cluster at the vertices. The BeijingFuzhou corridor, Beijing-Chongqing corridor, Chongqing-Zhuhai corridor, and Harbin-Haikou corridor constitute the four edges of this structure, with the Shanghai-Chongqing corridor serving as the central axis. All five corridors are distributed in the region east and south of the Hu Huanyong Line, indicating a high correlation between China's aviation network layout and population and urban distribution. It also reflects the overall control capacity of core airport clusters over air transport.

• A comparative analysis of carbon emissions before and after the delineation of the air corridors was conducted. The seven air corridors emitted a total of 619,431 tons of carbon, with the overall carbon emission trend aligning with the carbon emissions during the aircraft's CCD phase. Among these, the Harbin-Haikou corridor had the highest emissions, while the ChongqingZhuhai corridor had the lowest. The emissions were closely related to the number of route participants, flight volumes, and aircraft types in each corridor. Large aircraft do not have flight environment advantages and are primarily affected by the CO2 emission factor. The corridors in a high carbon emission efficiency state are the Harbin-Haikou corridor and HarbinChangsha corridor, those in a medium carbon emission efficiency state are the Beijing-Chongqing corridor and ShanghaiChongqing corridor, those in a low carbon emission efficiency state are the Beijing-Fuzhou corridor and Urumqi-Hangzhou corridor, and the corridor in an

extremely low carbon emission efficiency state is the Chongqing-Zhuhai corridor. Compared to the pre-corridor delineation, the average carbon emission per second generated by all aircraft in the seven corridors after delineation decreased by 79.75%, and the carbon emission per kilometer decreased by 93%, indicating that the carbon emission efficiency of aircraft improved after the corridors were delineated. This improvement is mainly due to the reduction in the average distance of ROC and the corresponding reduction in carbon emissions from flight routes.

Compared to existing studies (Yaqing et al. 2018), although this research divides only seven air corridors, the coverage is extensive, and the airspace structure is more prominent. The study found that the seven air corridors of different scales varied in terms of carbon emissions and emission efficiency, strongly confirming the uneven development of China's aviation industry in terms of regions, time periods, and other factors. Approaching the optimization of airspace resource utilization from the perspective of air corridor planning not only helps optimize the structural layout of airspace resources and improve airspace utilization efficiency but also provides a solid theoretical foundation for China's civil aviation industry to advance toward green development, offering valuable reference directions. However, the current study has certain limitations. Due to data collection difficulties, the analysis is based on only 1-month's flight data to identify and delineate air corridors and route network structure, resulting in a small sample size that may not fully reflect the complex and dynamic real-world situation. Therefore, future research should focus on expanding the data sample, incorporating long-term and multidimensional data, and conducting comprehensive analysis from a dynamic perspective. This will be a key focus for advancing research in this field in the future.

CONFLICT OF INTEREST

Nothing to declare.

AUTHORS' CONTRIBUTION

Funding Acquisition: Han R; Resources, Supervision: Han R; Writing - Review & Editing: Han R; Conceptualization: Ran X; Methodology: Ran X; Software: Ran X; Investigation: Ran X and Li H; Formal Analysis: Ran X; Writing - Original Draft: Ran X; Data Curation: Ran X and Han R; Visualization: Li H; Resources: Li H and Han R; Supervision: Li H; Validation: Li H and Han R; Final approval: Ran X.

DATA AVAILABILITY STATEMENT

Data sharing is not applicable.

FUNDING

The Third Batch of Hebei Youth Top Talent Project National Science Foundation of China Grants No:

42471327, 42071266

ACKNOWLEDGMENTS

Not applicable.

REFERENCES

Alipio J, Castro P, Kaing H, Shahid N, Sherzai O, Konohue GL (2003) Dynamic airspace super sectors (DASS) as high-density highways in the sky for a new US air traffic management system. Paper presented 2003 Systems and Information Engineering Design Symposium. IEEE, Charlottesville, USA. https://doi.org/10.1109/SIEDS.2003.158005

Babinski PBDO, Guterres MX, Albano CS (2024) Proposal of a matrix to measure the perceived level of safety in a terminal control area. J Aerosp Technol Manag 16: e2624. https://doi.org/10.1590/jatm.v16.1346

Chen J-T (2011) Design and analysis of a flow corridor-based traffic management initiative. West Lafayette: Purdue University. https://doi.org/10.2514/6.2011-6695

Chen R (2022) Spatiotemporal characteristics and evolution path of China's aviation network. Civil Aviation University of China [accessed 10/16/2024]. https://link.oversea.cnki.net/doi/10.27627/d.cnki.gzmhy.2022.000125 Han R (2023) Research on aviation carbon emission reduction based on optimal spatial and temporal allocation of airspace resources. Advances in Earth Science 38(3):309-319. https://doi.org/10.11867/j.issn.1001-8166.2023.008

Han R, Lu Z, Yao H (2019) Study on dynamic transformation, application and comparison of aviation carbon emission environmental damage assessment methods. Advances in Earth Science 34(7):688-696. https://doi.org/10.11867/j.issn.10018166.2019.07.0688

Hoffman R, Prete J (2008) Principles of airspace tube design for dynamic airspace configuration. Paper presented 2008 Congress of International Council of the Aeronautical Sciences. International Council of the Aeronautical Sciences; Anchorage, Alaska. https://doi.org/10.2514/6.2008-8939

[IIR-SJTU] Institute of Industry Research-Shanghai Jiao Tong University (2022) 2022 winter habitat suitability index for migratory bird retirement in China [accessed Nov 30 2022]. https://www.acem.sjtu.edu.cn/acem2021/ news/74464.html Jun ZS (2022) Constructing a new aviation emission model to reveal the carbon dioxide and pollutant emission characteristics of civil aviation in China [accessed Apr 14 2022]. https://www.env.tsinghua.edu.cn/info/1129/7501.htm Ligang Z (2015) Thoughts on problems of part of China's airspace. Civil Aviation Management 4:41-44.

Lili LBW (2012) The design of air highway network. Systems Engineering 30(11):107-111.

Lili ZZW (2019) Airspace planning and management. Pequim: Beihang University.

Liu H, Tian H, Hao Y, Liu S, Liu X, Zhu C, Wu Y, Liu W, Zhu C, Wu Y, et al. (2019) Atmospheric emission inventory of multiple pollutants from civil aviation in China: temporal trend, spatial distribution characteristics and emission features analysis. Sci Total Environ 648:871-879. https://doi.org/10.1016/j.scitotenv.2018.07.407

Lu C, Liu H, Song D, Yang X, Tan Q, Hu X, Kang X (2018) The establishment of LTO emission inventory of civil aviation airports based on big data. Earth Environ Sci 128(1):012069. https://doi.org/10.1088/1755-1315/128/1/012069

Lyu LHC, Xu SD, Yang N, Du MB, Cai BF (2022) Study on fine aviation carbon dioxide emission factors based on the flight phase. Climate Change Research 18(2):196-204. https://doi.org/10.12006/j.issn.1673-1719.2021.158

Nakamura Y, Takeichi N, Kageyama K (2014) A self-separation algorithm using relative speed for a high-density air corridor. Trans Japan Soc Aero Space Sci 57(6):336-342. https://doi.org/10.2322/tjsass.57.336

National Bureau of Statistics of China (2021) Seventh National Population Census Bulletin (No. 1) – Basic Information on the Seventh National Population Census Exercise [accessed May 11 2021]. https://www.gov.cn/guoqing/2021-05/13/content_5606149.htm

Ran X, Li L, Han R (2024) Spatiotemporal characteristics and influencing factors of airport service quality in China. J Air Transp Manag 117:102578. https://doi.org/10.1016/j.jairtraman.2024.102578

Shuyan ZZM, Zhao ZW, Bai B (2023) Evolution and influencing factors of air passenger transport in China from 2000 to 2019. Sci Geo Sin 43(6):1011-1021. https://doi.org/10.13249/j.cnki.sgs.2023.06.008

Sridhar B, Grabbe S, Sheth K (2006) Initial study of tube networks for flexible airspace utilization. Paper presented 2006 AIAA Guidance Navigation and Control Conference. AIAA; Keystone, Colorado. https://doi.org/10.2514/6.2006-6768

Takeichi N, Abumi Y (2016) Benefit optimization and operational requirement of flow corridor in Japanese airspace. Proceedings of the Institution of Mechanical Engineers, Part G-Journal of Aerospace Engineering 230(9):1780-1787. https:// doi.org/10.1177/0954410015616412

Tian YD, Yunlong Y, Bojia WL (2019) A framework for the assessment of distributed self-separation procedures for air traffic in flow corridors. IEEE Access 7:123544-123557. https://doi.org/10.1109/ACCESS.2019.2937655

Tone K (2001) A slacks-based measure of efficiency in data envelopment analysis. Eur J Oper Res 130(3):498-509. https://doi. org/10.1016/S0377-2217(99)00407-5

Wang DDJ, Fengjun J (2019) Comparison of spatial structure and linkage systems and geographic constraints: a perspective of multiple traffic flows. Acta Geo Sin 74(12):2482-2494.

https://doi.org/10.11821/dlxb201912005

Wang DDJ, Jingjuan WHJ (2016) The relationship between the development level of civil aviation and tourism in China. Sci Geo Sin 36(8):1125-1133. https://doi.org/10.13249/j.cnki.sgs.2016.08.001

Wang Z, Delahaye D, Farges JL, Alam S (2021) Air traffic assignment for intensive urban air mobility operations. J Aerosp Inf Syst 18(11):860-875. https://doi.org/10.2514/1.I010954

Xiang Z, Ruiling H, Xiaoyan Z, Xiaohui D (2023) Indirect connection analysis based on wave-system structures of airlines architecture in Hub Airport. J Aerosp Technol Manag 15:e1623. https://doi.org/10.1590/jatm.v15.1306

Xue M (2009) Design analysis of corridors-in-the-sky. Paper presented 2009 AIAA Guidance, Navigation and Control Conference. AIAA; Chicago, Illinois. https://doi.org/10.2514/6.2009-5859

Yang LFES (2023) Research on optimization management and adjustment methods of airline network. Modern Computer 29(7):80-84. https://doi.org/10.3969/j.issn.1007-1423.2023.07.014

Yang WXH, Zhang QR, Zhang F, Wang DDJ (2022) Pattern characteristics and dynamic evolution of urban network development in China based on the comparison between high-speed rail and airline flows. Sci Geo Sin 42(3):436-445. https:// doi.org/10.13249/j.cnki.sgs.2022.03.008

Yaqing D, Lu Z, Liu Y, Zhang Q (2018) The design of China's corridors-in-the-sky and the influence of air routes traffic on the identification of space-time congestion. Acta Geographica Sinica 73(10):2001-2013. https://doi.org/10.11821/dlxb201810013

Yaqing D, Lu Z, Yinuo Z, Feng F, Yan Y (2022) Deconstruction of air traffic flow network and dynamic allocation of airspace resources: a case study of Beijing-Chengdu corridor-in-the-sky. Geography and Geo-Information Science 38(1):116-123. https://doi.org/10.3969/j.issn.1672-0504.2022.01.017

Ye BH, Minghua S, John F (2014) Collision risk-capacity tradeoff analysis of an en-route corridor model. Chin J Aeron 27(1):124-135. https://doi.org/10.1016/j.cja.2013.12.007

Ye BN, Chao T, Yong O, Washington Y (2022) Data-driven distributionally robust generation of time-varying flow corridor networks under demand uncertainty. Trans Res C: Emerging Technologies 136:103546. https://doi.org/10.1016/j. trc.2021.103546

Ye BYT, Shortle J, Ochieng W (2019) Sensitivity analysis of potential capacity and safety of flow corridor to self-separation parameters. Aeronaut J 12(1259):56-78. https://doi.org/10.1017/aer.2018.116

Yinuo LZZ, Du Xinru, Yaqing D, Zhang J (2019) Research on airspace resource allocation supported by spatiotemporal continuous data: review and prospect. Advances in Earth Science 34(9):912-921. https://doi.org/10.11867/j.issn.10018166.2019.09.0912

Yousefi A, Zadeh AN (2013) Dynamic allocation and benefit assessment of NextGen flow corridors. Trans Res C: Emerging Technologies 33(4):297-310. https://doi.org/10.1016/j.trc.2012.04.016

Zhang YS, Sherry JL (2015) Methodology for collision risk assessment of an airspace flow corridor

concept. Reliab Eng Syst Saf 142:444-455. https://doi.org/10.1016/j.ress.2015.05.015

ISSN: 2175 9146

Methodology for Controlling Unmanned Aerial Vehicle Landing on a Ground Wheeled Robot Tethered by Cable

Eduard Kuris1,* , Konstantin Lelkov1 , Timofey Khorev1
1.Moscow Aviation Institute – Control Systems, Informatics and Electric Power Engineering – Flight-navigation and InformationMeasuring Complexes – Moscow – Russian Federation.

A B S T R A C T

For a robotic heterogeneous complex (RHC) consisting of a ground wheeled robot (GWR) and an unmanned aerial vehicle (UAV) connected by a tether mechanism (TM) and subject to steady wind acting on the UAV, a methodology for selecting control parameters for UAV landing on the GWR is considered. Landing is proposed along the straight line connecting the tether attachment point on the UAV with its base on the GWR. A synthesis of control for the TM and UAV engines was carried out to ensure landing within a predetermined time. A corresponding mathematical model of UAV and TM motion was derived. It is shown that the UAV's equilibrium positions along the line are stable, ensuring minimal engine energy consumption during landing. A synthesis of piecewise-linear damping coefficients in the control systems for the TM and UAV engines was performed by selecting moments of slope change based on synchronizing the instantaneous tether length and the distance from the UAV to the landing point. Simulation of the full equations of motion confirmed the feasibility of the proposed UAV landing methodology on the GWR and the validity of the assumptions made.

Keywords: *Unmanned aerial vehicles (UAVs); Aerospace vehicle landing; Wind effects; Tether systems; Control systems.*

INTRODUCTION

A heterogeneous system (RHS) consisting of a wheeled unmanned ground vehicle (UGV) and an unmanned aerial vehicle (UAV) connected by tether mechanism (TM) is undoubtedly an advanced development (Aleshin et al. 2020; Alonso Tabares and Mora-Camino 2017) for the purpose of monitoring the entire outer surface of an aircraft in its parking lot. With the help of such an RHS, monitoring is carried out simultaneously by cameras installed on both the UAV and the wheeled UGV (Cantelli et al. 2013; Kim et al. 2019; Wang L et al. 2020). When using such a wheeled UGV to inspect the aircraft surface, a critical factor is ensuring the operation of the TM, which guarantees the UAV collision avoidance with the aircraft under extreme wind impact conditions. In this case, both wind effects and TM forces act as external disturbances for the UAV, and its onboard control system must compensate them to a significant extent to ensure stable flight. The issue of compensation for external disturbances of UAV are widely covered in various studies (Liu et al. 2024; Uzun and Oktay 2023). There are differential methods of wind impacts in the UAV control system. However, these methods have natural constraints associated with limiting the maximum propellers' thrust of UAV (Chodnicki et

al. 2022; Krishnakumar et al. 2015; Wang B et al. 2020). Generally, the UAV and the aircraft collision avoidance can be ensured if the aerodynamic force from the wind impact on the UAV is counteracted not only by the UAV propellers' forces, but also by the forces generated by the power-guided TM engine to a considerable degree. Moreover, it is assumed that the design of the TM is chosen so that the maximum force exerted by it is greater than the maximum force from the possible wind impact on the UAV. A diagram illustrating the force distribution applied to a multi-rotor UAV when held by TM is shown in the Fig. 1 (Aleshin et al. 2020).

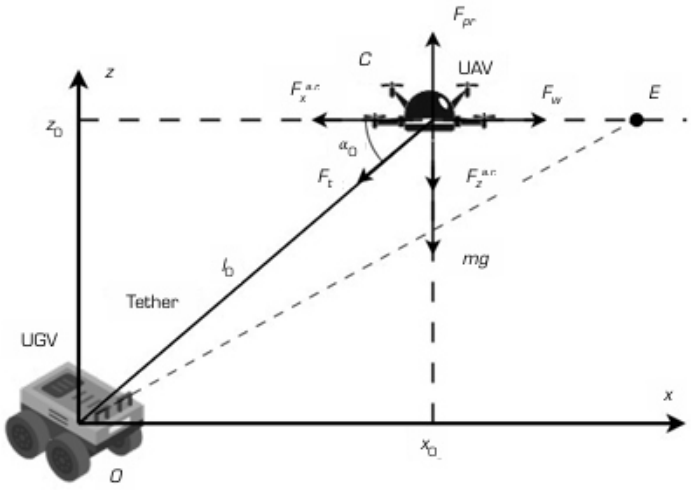

Source: Adapted from Aleshin *et al.* (2020).

Figure 1. Scheme of forces distribution applied to the UAV in the process of counteracting extreme wind impact. Oaxaza is a coordinate system (CS), rigidly connected with UAV (Oa is UAV's center of mass, axis Oaxa is horizontal and applied normal to the UAV trajectory towards the outer surface of the aircraft, axis Oaza is applied to the position vertical); Oxz is CS centered at O in the wheeled UGV's center of mass (its axes are parallel to the corresponding CS axes Oaxaza), O also coincides with the place of tether attachment in the TM; C is the starting point at which the UAV is located before a gust of wind and where it returns before landing, (its coordinates x0, z0); l0 is the tether segment length from the wheeled UGV to the UAV when it is located at the point C; Fw is the aerodynamic force created by the wind load on the UAV; Ft is the force acting on UAV from the tether side; Fpr is the thrust created by the rotors (Aleshin et al. 2020); mg is the UAV gravity (m is the UAV mass, g is the gravity acceleration); Fx, Fz is the drag force acting on the UAV, respectively, along the axes Xa, Za; α0 is the tether tilt angle with the respect to the horizon plane when the UAV is located at the point C. In Fig. 1, the motion from the point C (after the beginning of the wind load action) to the point E and inversely occurs according to a certain algorithm given in Aleshin et al. (2020) and including mainly the operation of the TM engine with the withdrawing the tether to its maximum value at point E (located directly next to the surface of the aircraft) and the subsequent UAV return to the point C where it is in an equilibrium position. The objective of this study is to analyze the possibility and synthesis of TM and UAV control systems under

conditions of the unchanged direction of the wind impact, in which the UAV is pulled up to the landing place on the wheeled UGV along the line connecting the point C of the UAV's initial location and the tether's attachment place O. This is done by organizing its motion along a straight line OC to such a height in the vicinity of the point O from which the landing can be carried out without the participation of TM in accordance with the landing algorithm of the control system of the UAV itself.

Theoretical basis

The mathematical model of the RHS under the specified motion conditions can be considered as a combination of the motion model of the UAV's center of mass and the TM's mathematical model with a DC motor (Aleshin et al. 2020):

$$\begin{aligned}
&m\ddot{x} = F_w - F_t\cos\alpha - F_x^{a.r.};\\
&m\ddot{z} = F_{pr} - F_t\sin\alpha - F_z^{a.r.} - mg;\\
&\alpha = \arccos\frac{x}{\sqrt{x^2 - z^2}};\\
&L_c\dot{I} + R_c I = U - c_{cef}\omega_c;\\
&\left(J + mr_c^2\right)\dot{\omega}_c + \varepsilon\omega_c = M_{met} - \left(\left(F_w\cos\alpha - F_x^{a.r.}\right) + \left(F_{pr} - mg\right)\sin\alpha\right)r_c;\\
&M_{met} = nI;\\
&F_t = \frac{M_{met}}{r_c},
\end{aligned} \tag{1}$$

where x,z are the coordinates of the UAV center of mass in the CS Oxz, α is the tether tilt angle with the respect to the horizon plane, U is the control voltage on the motor, I is the current in the motor drive winding, ωc is the angle rate of the shaft rotation of the motor with the coil (ωc > 0 when winding the tether on the coil), Mmet is the electromagnetic torque on the motor shaft, J is the moment of inertia of the motor shaft with the coil, ε is the torque coefficient of the viscous friction around the axis of the motor shaft's rotation, Lc, Rc are the inductive property and resistance of the motor control winding, respectively, Ccef is coefficient of counter-electromotive force, n is the torque constant of the motor, and rc is the average radius of the coil with the tether. The forces of aerodynamic air resistance Fx a.r., Fza.r. directed by true airspeed are determined by the ratios:

$$F_i^{a.r.} = c_{di}\frac{\rho v_i^2}{2}S_i, i = x, z, \tag{2}$$

where cdi , vi are the non-dimensional aerodynamic coefficients and true airspeed in the corresponding axes' direction, Si are the UAV's effective surface areas normal to the corresponding axes, and ρ is the air density. In the current study, the aerodynamic characteristics of the UAV were determined experimentally, but in general, this can also be done based on modeling (Xie et al. 2022).

METHODOLOGY

Determining the stable position line of the UAV during landing

As mentioned above, upon condition α = α0, the UAV is located at point C in the equilibrium position,

while the required tether tension Ft and lift Fpr can be expressed in terms of a known wind force's constant Fw as follows:

$$F_t = F_w / \cos\alpha;$$
$$F_{pru} = F_w \tan\alpha_0 = F_{pr} - mg. \quad (3)$$

It follows from Eq. 1 that the force F_t corresponds to a motor's constant control voltage U_0 equal to:

$$U_0 = F_t R_c \frac{r_c}{n}. \quad (4)$$

From Eqs. 1 and 3, it is seen that when the UAV is located on a straight axis OC, the ratio is fulfilled for each of its points (x, z):

$$\frac{x}{\sqrt{x^2 + z^2}} = \frac{x_0}{\sqrt{x_0^2 + z_0^2}} \quad (5)$$

At the same time, the values of the forces Ft and Fpru will not change. Thus, at each point of the OC line, when performing Eqs. 3 and 5, the UAV will be in the equilibrium position. It must be shown that this position is stable. Figure 2 shows the forces acting on the UAV at the starting point C (Ft) and at its random displacement to the point C1 (Fw).

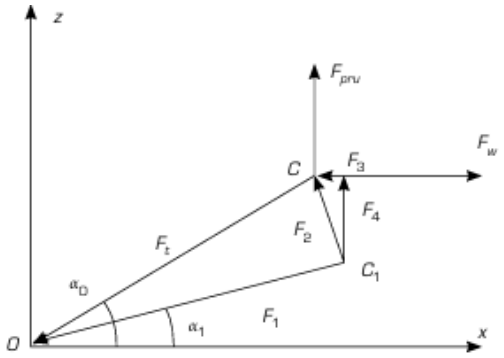

Source: Elaborated by the authors.

Figure 2. Forces' distribution when the UAV is displaced from C to C_1.

Note that the absolute value of $\mathbf{F}_1$ is equal to the absolute value of $\mathbf{F}_t$. In this case, a force $\mathbf{F}_2$ arises such that:

$$\mathbf{F}_t = \mathbf{F}_1 + \mathbf{F}_2. \quad (6)$$

In its turn, F2 is decomposed into components – vertical F3 and horizontal F4, the impact of which returns the UAV to a straight line α = α0. Under the effect of these forces, oscillations occur simultaneously along the horizontal and vertical axes. With damping, the UAV will return to the equilibrium position at the angle α = α0, although the UAV's coordinates may change both vertically and horizontally. This equilibrium position satisfies the Lyapunov stability criterion (Pukdeboon 2011). The system's simulation of the first three equations in Eq. 1 was carried out when performing Eq. 3 to validate the stability of the UAV's straight-line α = α0 equilibrium positions, considering the introduction of damping terms.

$$m\ddot{x} = F_w - F_t\cos\alpha - F_x^{a.r.} - k\dot{x};$$
$$m\ddot{z} = F_{pru} - F_t\sin\alpha - F_z^{a.r.} - k\dot{z}; \quad (7)$$
$$\alpha = \arccos\frac{x}{\sqrt{x^2+z^2}},$$

where , kxkz are the damping forces formed in the UAV engine control system when it is displaced along the corresponding coordinate axes. It is worth noting that to determine the tether tilt angle α in Eq. 7, it is necessary to ensure the determination of high-precision navigation parameters of the UAV and the wheeled UGV. In particular, robust inertial guidance algorithms can be used regarding to the use of the wheeled UGV and UAV near the aircraft's surface, where there are significant distortions of satellite navigation signals (Antonov et al. 2017; Veremeenko et al. 2020; 2021; Zharkov et al. 2022). The simulation result for m = 6 kg, F = 30 N, cd = 0,15, cdx = 0,12, Sx = 0.04 m2, Si = 0.03 m2, k - 2 N·s, x0 = 20 m, z0 = 15 m, α0 = 0.6435 rad and initial conditions x = 21 m, z = 15.5 m is shown in Fig. 3 (the quantities' steady-state values are α = α0, x = 20.38 m, z = 15.29 m).

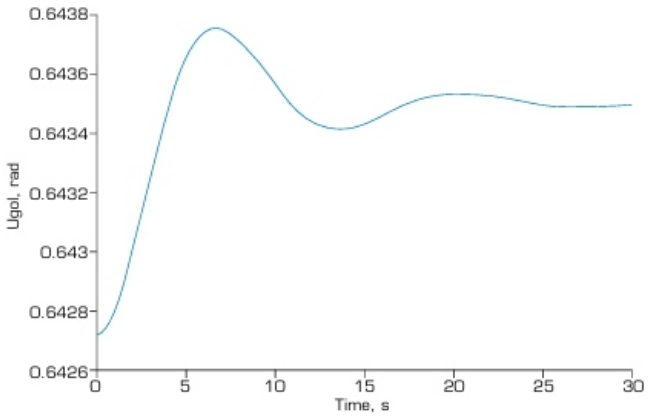

Source: Elaborated by the authors.

Figure 3. Angle change α in case of accidental UAV's deviation from the line $\alpha = \alpha_0$.

Synthesis of TM control

Define the required additional control voltage ku·U0 on the TM engine in Eq. 2 corresponding to the desired UAV's landing time tb on the wheeled UGV. Introduce the notations:

$$U = U_0 + k_u U_0;$$
$$I = I_0 + k_i I_0; \quad (8)$$
$$F_t = F_0 + k_f F_0,$$

where U0 and I0 are the steady-state values of voltage and current in the TM motor corresponding to the tether's tension force in the equilibrium position at the angle I0 and ku, ki , kf are coefficients setting the corresponding control points. For clarity of further compilations, Eq. 1 is transformed by introducing the following terms: F0cosα0 – F0cosα0 in the Eq. 1 and F0sinα0 – F0sinα0 in the second one. Replacing now Fw = F0cosα0, Fpru = F0sinα0 and neglecting the aerodynamic forces' influence, the following is obtained with regard to Eq. 8:

$$
\begin{aligned}
&m\ddot{x} = F_0\left(\cos\alpha_0 - \cos\alpha\right) - k_f F_0 \cos\alpha;\\
&m\ddot{z} = F_0\left(\sin\alpha_0 - \sin\alpha\right) - k_f F_0 \sin\alpha;\\
&\alpha = \arccos\frac{x}{\sqrt{x^2+z^2}};\\
&L_c\dot{I} + R_c k_i I = k_u U_0 - c_{cef}\omega_c;\\
&\left(J + mr_c^2\right)\dot{\omega}_c + \varepsilon\omega_c = nk_i I + F_0\left(1 - \cos\left(\alpha_0 - \alpha\right)\right)r_c;\\
&k_f F_0 = k_i I \cdot n / r_c.
\end{aligned}
\tag{9}
$$

For the landing time tb analytical determination, it is assumed that 0 c LI= and neglect (based on preliminary numerical estimates) the last term in the fourth equation. Then, the third and fourth equations in Eq. 9 can be considered separately from the first three. Adding to them the obvious ratio connecting tb with ωc and the tether's length l0, get:

$$
\begin{aligned}
&R_c k_i I_0 = k_u U_0 - c_{cef}\omega_c;\\
&\left(J + mr_c^2\right)\dot{\omega}_c + \varepsilon\omega_c = nk_i I_0;\\
&l_0 = r_c\int_0^{t_b}\omega_c dt;\\
&l_0 = \sqrt{x_0^2 + z_0^2}.
\end{aligned}
\tag{10}
$$

Finding from the first equation in Eq. 10 and inserting it into the second gives:

$$
\left(J + mr_c^2\right)\dot{\omega}_c + \left(\varepsilon + nc_{cef} / R_c\right)\omega_c = nk_u\frac{U_0}{R_c}.
\tag{11}
$$

The solution of the linear differential Eq. 11 with $\omega_c(0) = 0$ is written as (Massera and Schäffer 1958):

$$
\omega_c = a\left(1 - e^{-a_1 t}\right),
\tag{12}
$$

where $a = nk_u\dfrac{U_0}{\left(\varepsilon + nc_{cef} / R_c\right)\cdot R_c}$; $a_1 = \dfrac{\varepsilon + nc_{cef} / R_c}{J + mr_c^2}$.

Inserting Eq. 12 into the last equation in Eq. 10 and integrating, obtain the desired dependence between the landing time and the voltage control coefficient from Eq. 8:

$$
l_0 = ar_c\left(t_b + \left(e^{-a_1 t_b} - 1\right) / a_1\right)
\tag{13}
$$

or

$$
k_u = \left(\varepsilon + nc_{cef} / R_c\right)R_c\frac{\dfrac{l_0}{r_c\left(t_b + \dfrac{e^{-a_1 t_b} - 1}{a_1}\right)}}{n} / U_0
\tag{14}
$$

Estimate the formal time of the UAV's motion to the landing point in accordance with the first two equations in Eq. 9, assuming that the motion occurs along the line $\alpha = \alpha_0$. Then, taking into account Eq. 4, it will be as follows:

$$m\ddot{x} = -k_u U_0 \frac{n}{R_c} / r_c \cdot \cos\alpha_0;$$
$$m\ddot{z} = -k_u U_0 \frac{n}{R_c} / r_c \cdot \sin\alpha_0. \quad (15)$$

Since each of these equations is a projection of the UAV's motion along the tether tension line on the corresponding axis, for the desired time t_d have the ratio:

$$t_d = \sqrt{\frac{2x_0 m}{k_u U_0 \frac{n r_c}{R_c} \cos\alpha_0}}. \quad (16)$$

Calculations have shown that with the same UAV and TM parameters, the time of the UAV's motion to the landing point in accordance with Eq. 15 is significantly less than the time tb of the tether's winding off by the TM engine in accordance with Eq. 10. This will lead to the tether's sagging, subsequent oscillations of the UAV and a complete disturbance of the landing mode in question. To maintain the proposed landing mode, the value and direction of the UAV engines' thrust were changed so that the times td and tb coincided. Studies have shown that it is advisable to form these additional forces as damping ones – as a of the UAV velocities according to the corresponding coordinates. Then, Eq. 15 will be as follows:

$$m\ddot{x} = -f_{xd}\dot{x} - k_u U_0 \frac{n r_c}{R_c} \cos\alpha_0;$$
$$m\ddot{z} = -f_{zd}\dot{z} - k_u U_0 \frac{n r_c}{R_c} \sin\alpha_0, \quad (17)$$

where fxd, fzd are the corresponding functions at which the synchronization of the current tether length obtained by solving Eq. 10 and the current position of the UAV is carried out – the values of 2 2 L x z = + (the current distance from the position of the UAV to the point of intended landing) obtained by solving Eq. 17. The formation of forces fxdX and fzdZ, for example, for a six-rotor occurs due to the total thrust vectoring (Arellano-Muro et al. 2013). For an anticipatory appraisal of the motion's time of the UAV to the landing point, we will consider fxd as a constant value. In this case, the equations' form of Eq. 17 coincides with Eq. 11, and the solution, for example, of the first equation in Eq. 17 at the initial value will be written as:

$$\dot{x} = c\left(t_d \frac{e^{-c_1 t_d} - 1}{c_1}\right), \quad (18)$$

where $c = -k_u U_0 \frac{n r_c}{R_c} \cdot \frac{\cos\alpha_0}{f_{xd}}$; $c_1 = \frac{f_{xd}}{m}$.

Then for the coordinate $x(t)$ at $x(0) = 0$ and $t = t_d$ get:

$$x(t_d) = ct_d + c\frac{e^{-c_1 t_d}}{c_1} + x_0 - \frac{c}{c_1}. \quad (19)$$

To simulate the landing process, it is necessary to set the time tb = td. When choosing it, the following factors should be taken into account. It should be more than the time constant ai in Eq. 11 and ci in Eq. 18, which will make it possible to consider the tether's and the UAV's motion in the landing process as quasi-stationary, acceptable for practical implementation. At the same time, the least (minimum) energy should be spent when generating voltage on the TM engine and in engines that create thrust. A detailed study of this issue is beyond the scope of the article.

RESULTS

To evaluate the effectiveness of the proposed UAV landing control system, simulation was carried out. The obtained data illustrate the necessary degree of synchronization between the UAV's movement and the operation of the tether mechanism, which in turn ensures the appropriate quality of the landing process.

Set:

$$t_b = t_d = 60\text{c}. \tag{20}$$

For further calculations, the initial values of the UAV and TM parameters were assumed to be the same as in Aleshin et al. (2020): cosα0 = 0.8; J = 0.7 kgm2; m = 6 kg; cdz = 0.15; cdx = 0.12; ccef = 0.016 Vs/rad; Fw = 30 N; ε = 3·10-3 Nm/rad; n = 0.5 Nm/A; I0 = 25 m. When using the ratios Eq. 14 and Eq. 16 to achieve the minimum difference between td and tb, the following results were obtained for the conditions: Rc = 0.2 Ohms; Rc = 0.3 m, while td increased from 10 s to 28 s. For td = 60 s from Eq. 19, the value was determined numerically, based on the division method of the segment in half (Tikhonov et al. 1995), obtained fxd = 0.916 value and the following values in Eq. 8:

$$U_0 = 4.5\text{ V}; I_0 = 22.5\text{ A}; F_0 = 37.5\text{ N}; k_u = 0.0102; k_j = 0.0102 \tag{21}$$

The graph of the UAV coordinate change obtained by solving Eq. 1 for the above parameters and values from Eq. 21 is shown in Fig. 4.

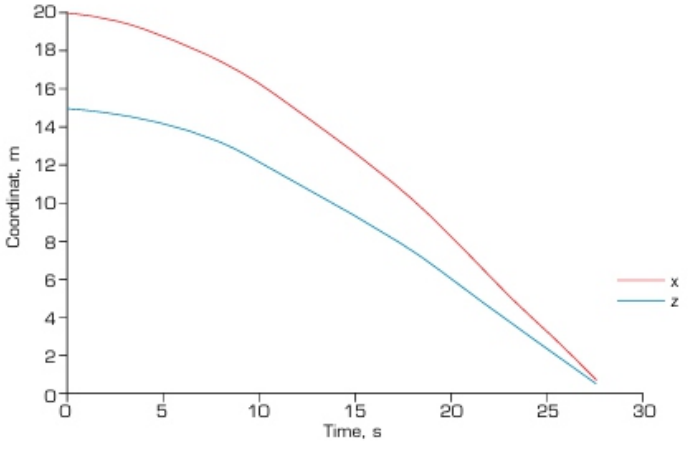

Source: Elaborated by the authors.

Figure 4. Changing the coordinates of the UAV in the motion process to the landing point.

Note that the motion time is close to the one set in Eq. 20. Simultaneously, near the landing point, the UAV's speed is unacceptably high. Now, consider a situation where the wind force remains constant but its magnitude depends on the height above the Earth's surface (absolute altitude). Obviously, in the vicinity of the landing point, the wind force will decrease so much as that only the regular UAV control system will be sufficient for further landing. Let, for example, the dependence of wind strength on height be given by the function (Turgut and Usanmaz 2016):

$$F_w(z) = F_{w0}\left(z^{n/(2-n)} - z_2^{n/(2-n)}\right) / \left(z_1^{n/(2-n)} - z_2^{n/(2-n)}\right), \quad (22)$$

where F_w, F_{w0} are, respectively, the wind strength at the current height Z and the initial one Z_1, Z_2 is the height at which $F_w = 0$, and n is a coefficient that takes into account the temperature gradient in height. The dependence graph Eq. 22 is shown in Fig. 5.

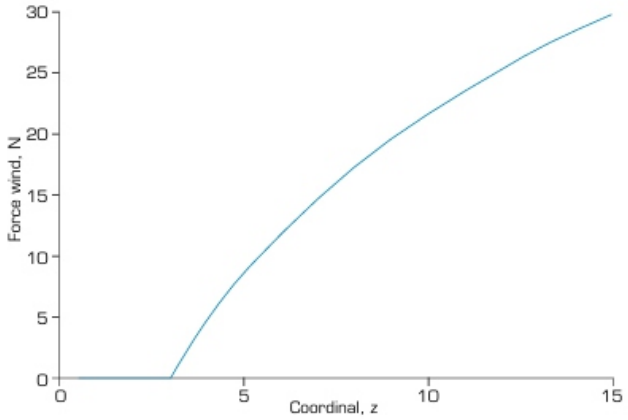

Source: Elaborated by the authors.

Figure 5. Wind strength dependence of an altitude ($z_1 = 3$).

Modeling of the landing process will be carried out according to the following algorithm. From height z = z1 to z = z3 (z3 > z1), landing occurs due to the attraction of the UAV along a line close to α = α0, while the formation of the value of the control voltage U = KuU0(Z) in Eq. 2 is carried out in accordance with the ratio (Eq. 4) (for U0(Z(t))) and the coefficient ku is determined from Eq. 14 and is constant throughout the entire motion from z = z1 to z = z2. The formation of coefficients fxd and fzd, as before, is made from the condition of ensuring synchronization of the current tether length and the UAV's position. At altitude z = z3 only the voltage U = U0(z), corresponding to the wind force at altitude z = z3 is applied to the TM engine, while damping forces fzdz and fxdx continue to form in the UAV engines. In this case, the UAV's speed gradually decreases and UAV's position becomes stable due to the UAV's stable position relative to the line α = α0. However, under the action of inertia, the tether continues to wind off. To synchronize the tether's length with the UAV's coordinates, an appropriate compensating voltage is formed on the TM engine. The UAV hovers, then further landing is carried out with the TM engine turned off only due to the operation of the standard UAV control system. Figures 6–9 represent the results of modeling. Figures obtained on the basis of integration (Eq. 1) with Coordinat, m the corresponding forming of functions fxd and fzd in Eq. 17 for z3 = 5 m and the UAV and TM parameter values mentioned above.

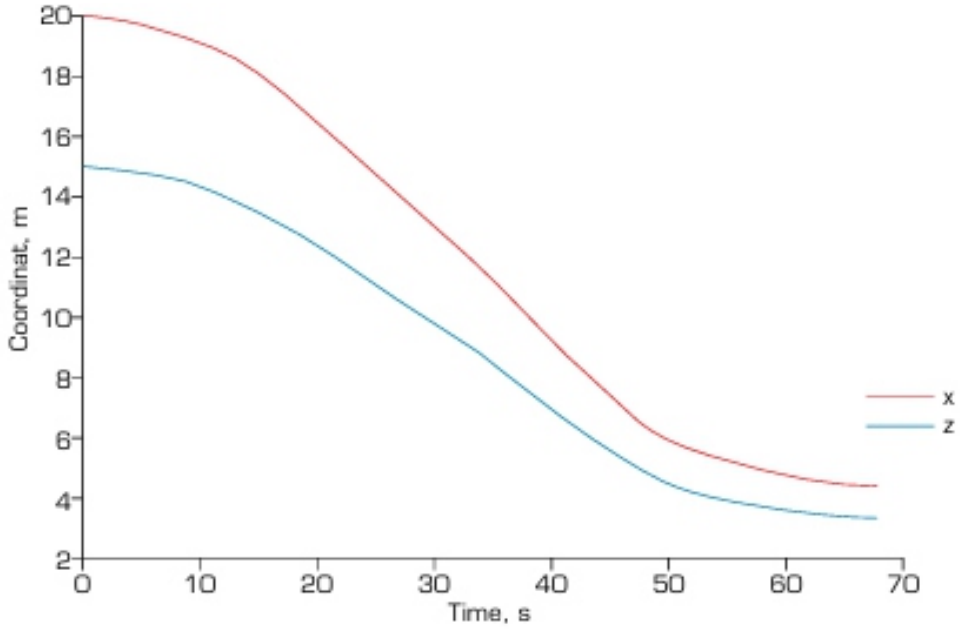

Source: Elaborated by the authors.

Figure 6. UAV coordinates.

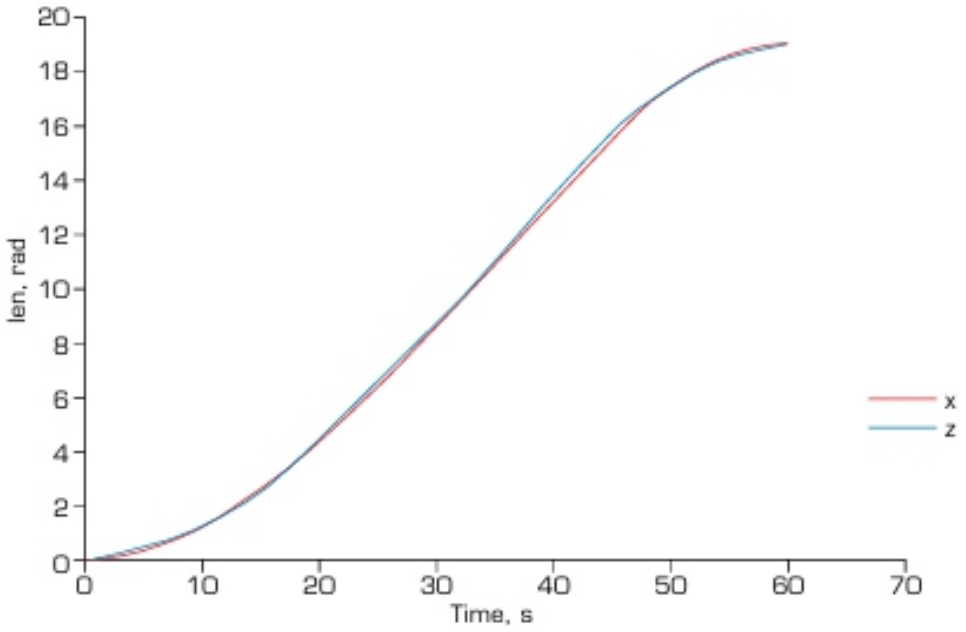

Source: Elaborated by the authors.

Figure 7. Variation of the tether's length and modification in the current distance from the UAV to the presumed landing location $L = \sqrt{x^2 + z^2}$.

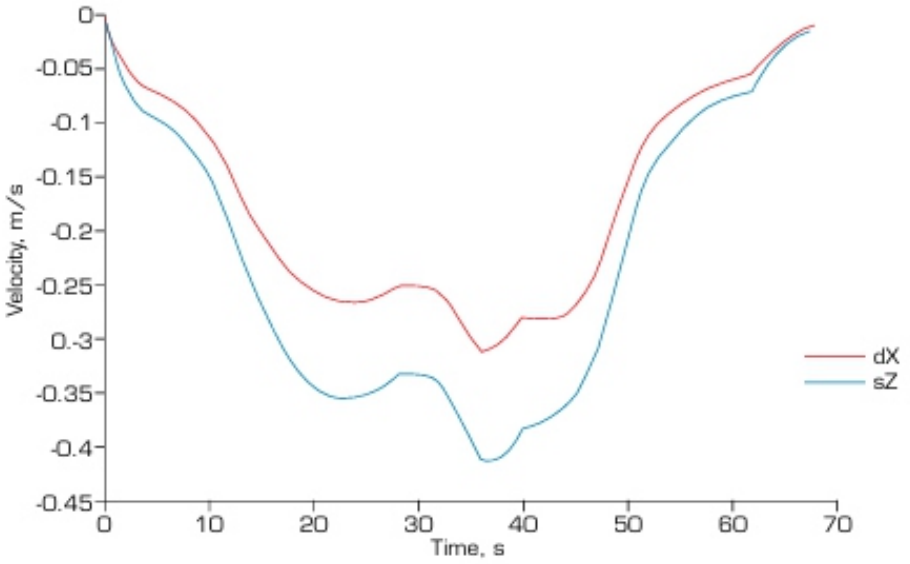

Source: Elaborated by the authors.

Figure 8. UAV velocities projections.

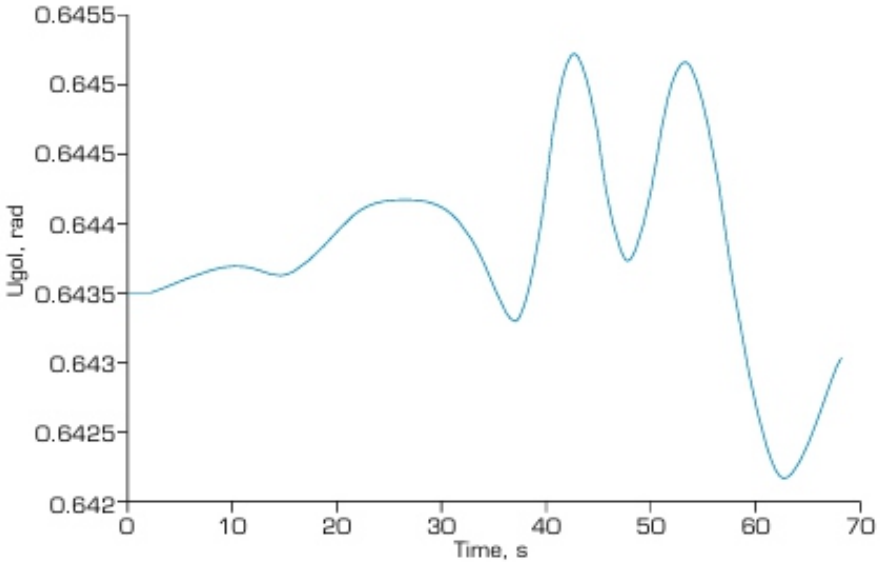

Source: Elaborated by the authors.

Figure 9. Variation in angle α (± 0,015 rad).

DISCUSSION

Under conditions of increasing wind force with changes in the UAV's height, an algorithm for its landing has been proposed, including: attraction of UAV along a straight line connecting the points of attachment of the tether to the UAV and the wheeled UGV, achieved through the formation of a control voltage in the form of the sum of the main voltage, countering the wind force at each height and the voltage controlling the winding of the tether, which is proportional to the main voltage with a predetermined proportionality coefficient; and the formation of the lift in the UAV engines from the main constant force, compensating for its weight and the vertical component of the tether tension force, along with damping forces that allow synchronization of the current tether length with the distance from

the UAV to the tether attachment point on the landing site of the wheeled UGV.

Future research is planned to explore the effects of wind gusts, characterized by their known probabilistic properties, on the dynamics of UAV flight during takeoff and landing processes, following the methodology outlined in this paper. The modeling results have confirmed the functionality of the proposed UAV landing algorithm on a moving platform under quasi-constant extreme wind conditions.

CONCLUSIONS

The analysis of the obtained results allows for the following conclusions:

• The UAV's position on the straight line connecting the tether attachment points on the UAV and the wheeled UGV, under a constant wind effects, is stable according to the Lyapunov stability criterion. Thus, with an initial deviation of UAV of 1 m horizontally and 0.5 m vertically, after several oscillations, it returns to the equilibrium position at the coordinates related by the equation of the indicated line (Fig. 3);

• Based on preliminary numerical estimates, it has been possible to divide the initial general system of equations of motion of the UAV and TM into two independent systems. For each of these, an analytical solution has been obtained and, based on the desired landing time, preliminary control coefficients in the TM engine and damping forces in the UAV engines have been selected;

• For the simulation, the initial values of UAV and TM parameters were taken to be the same as in (Aleshin et al. 2020): $\cos\alpha 0 = 0.8$; $J = 0.7$ kgm2; $m = 6$ kg; $cdz = 0.15$; $cdx = 0.12$; $ccef = 0.016$ Vs/rad; $Fw = 30$ N; $\varepsilon = 3 \cdot 10\text{-}3$ Nm/rad; $n = 0.5$ Nm/A; $I0 = 25$ m.

• The landing time has been selected considering: ensuring the UAV's quasi-stationary motion during landing; acceptability for practical implementation; energy costs during the formation of voltage on the TM engine and in engines that create thrust;

• A simulation of the solution of the complete equations of UAV motion during landing has been carried out, and numerical synthesis of piecewise linear damping coefficients has been conducted by selecting the moments in time of change of their slope from the condition of synchronization of the current values of the cable length and the distance from the UAV's location during the movement to the point of the expected landing.

In this case, from the initial height $z1 = 15$ m to the height $z3 = 5$ m landing occurs due to the operation of TM by attracting UAV along a line close to $\alpha = \alpha 0$, while forming the value of the control voltage $U = kuU0(z)$ is carried out in accordance with the change in wind strength with height, and the coefficient ku is constant throughout the entire movement up to the height $z2 = 3$ m at which the wind force is practically zero (Fig. 5). In this case, the damping forces fzdz and fxdx, continue to form in the UAV engines to ensure synchronization of the current cable length and the UAV position. The speed of UAV gradually decreases and its position stabilizes due to the stability of UAV position relative to the straight

line α = α0. The UAV hovers, after which further landing is carried out with the TM engine turned off, only due to the operation of the standard UAV engine control system. T he corresponding Figs. of the change in UAV coordinates are presented in the Figs. 6–9.

CONFLICT OF INTEREST

Nothing to declare.

AUTHOR CONTRIBUTIONS

Conceptualization: Kuris E, Lelkov K, and Khorev T; Data curation: Kuris E, Lelkov K, and Khorev T; Formal analysis: Kuris E, Lelkov K, and Khorev T; Acquisition of funding: Kuris E, Lelkov K, and Khorev T; Research: Kuris E, Lelkov K, and Khorev T; Methodology: Kuris E, Lelkov K, and Khorev T; Project administration: Kuris E, Lelkov K, and Khorev T; Supervision: Kuris E, Lelkov K, and Khorev T; Validation: Kuris E, Lelkov K, and Khorev T; Writing - Preparation of original draft: Kuris E, Lelkov K, and Khorev T; Writing - Proofreading and editing: Kuris E, Lelkov K, and Khorev T; Final approval: Kuris E, Lelkov K, and Khorev T.

DATA AVAILABILITY STATEMENT

All data sets were generated or analyzed in the current study.

FUNDING

Russian Science Foundation Grant No. 23-29-00958

ACKNOWLEDGEMENTS

Not applicable.

REFERENCES

Aleshin BS, Chernomorsky AI, Kuris ED, Lelkov KS, Ivakin MV (2020) Robotic complex for inspection of the outer surface of the aircraft in its parking lot. Incas Bull 12:21-31. https://doi.org/10.13111/2066-8201.2020.12.S.2

Alonso Tabares D, Mora-Camino F (2017) Aircraft ground handling: analysis for automation. Paper presented 2020 17th AIAA Aviation Technology, Integration, and Operations Conference. AIAA; Denver, USA. https://doi. org/10.2514/6.2017-3425

Antonov DA, Veremeenko KK, Zharkov MVE, Kuznetsov IM, Pron'kin AN (2017) Fault-tolerant airport vehicle integrated navigation system. Paper presented 2017 24th Saint Petersburg International

Conference on Integrated Navigation Systems.

State Research Center of the Russian Federation. Concern Central Scientific and Research Institute Elektropribor; St. Petersburg, Russia. https://doi.org/10.23919/ICINS.2017.7995620

Arellano-Muro CA, Luque-Vega LF, Castillo-Toledo B, Loukianov AG (2013) Backstepping control with sliding mode estimation for a hexacopter. Paper presented 2013 10th International Conference on Electrical Engineering, Computing Science and Automatic Control. Instituto Politécnico Nacional and the Departments of Automatic Control; Mexico City, Mexico. https://doi.org/10.1109/ICEEE.2013.6676026

Cantelli L, Presti ML, Mangiameli M, Melita CD, Muscato G (2013) Autonomous cooperation between UAV and UGV to improve navigation and environmental monitoring in rough environments. Paper presented 10th International Symposium on Humanitarian Demining coupled with the 11th IARP WS HUDEM. IARP; Sibenik, Croatia. https://www.researchgate.

net/publication/303245963_Autonomous_Cooperation_between_UAV_and_UGV_to_improve_navigation_and_ environmental_monitoring_in_rough_environments Chodnicki M, Siemiatkowska B, Stecz W, Stępień S (2022) Energy efficient UAV flight control method in an environment with obstacles and gusts of wind. Energ 15(10):3730. https://doi.org/10.3390/en15103730

Kim P, Price LC, Park J, Cho YK (2019) UAV-UGV cooperative 3D environmental mapping. Paper presented ASCE International Conference on Computing in Civil Engineering 2019. American Society of Civil Engineers, Reston, VA. Krishnakumar R, Rasheed AM, Kumar KS (2015) Enhanced hover control of quad tilt frame UAV under windy conditions. Int J Adv Robot Syst 12(10):146. https://doi.org/10.5772/61231

Liu Z, Wen S, Huang G, Li S, Deng Z (2024) Agricultural UAV obstacle avoidance system based on a depth image inverse projection algorithm and b-spline curve trajectory optimization algorithm. Inf Techn and Contr 53(3):736-757. https://itc. ktu.lt/index.php/ITC/article/view/36021

Massera JL, Schäffer JJ (1958) Linear differential equations and functional analysis, I. Annals of Math 67(3):517-573. https:// doi.org/10.2307/1969871

Pukdeboon C (2011) A review of fundamentals of Lyapunov theory. J Appl Sci 10(2):55-61. https://www.researchgate.net/

publication/267976343_A_Review_of_Fundamentals_of_Lyapunov_Theory Tikhonov AN, Goncharsky AV, Stepanov VV, Yagola AG (1995) Numerical methods for the approximate solution of ill-posed problems on compact sets. Amsterdam: Springer. Turgut ET, Usanmaz Ö (2016) An analysis of vertical profiles of wind and humidity based on long-term radiosonde data in Turkey. Anadolu Univ J Sci and Techn A-Appl Sci and Eng 17(5):830-844. https://doi.org/10.18038/aubtda.279852

Uzun M, Oktay T (2023) Simultaneous UAV having actively sweep angle morphing wing and flight control system design. Aircr Eng and Aerosp Techn 95(3):1062-1068. https://doi.org/10.1108/AEAT-

09-2022-0259

Veremeenko KK, Zharkov MV, Kuznetsov IM, Pron'kin AN (2020) Strapdown inertial navigation system transfer alignment: algorithmic features and simulation performance analysis. Russ Aeronaut 63:618-626. https://doi.org/10.3103/S106879982004008X

Veremeenko KK, Zharkov MV, Kuznetsov IM, Pron'kin AN (2021) Investigation of parametric uncertainty influence on accuracy of strapdown inertial navigation system transfer alignment. Russ Aeronaut 64:518-525. https://doi.org/10.3103/S106879982103020X

Wang B, Ali ZA, Wang D (2020) Controller for UAV to oppose different kinds of wind in the environment. J Contr Sci and Eng 2020(1):5708970. https://doi.org/10.1155/2020/5708970

Wang L, Cheng D, Gao F, Cai F, Guo J, Lin M, Shen S (2020) A collaborative aerial-ground robotic system for fast exploration. Paper presented 2018 International Symposium on Experimental Robotics. International Foundation of Robotics Research; Buenos Aires, Argentina. https://doi.org/10.1007/978-3-030-33950-0_6

Xie J, Huang J, Song L, Fu J, Lu X (2022) An effort saving method to establish global aerodynamic model using CFD. Aircr Eng and Aerosp Techn 94(11):1-19. https://doi.org/10.1108/AEAT-10-2021-0299

Zharkov MV, Veremeenko KK, Kuznetsov IM, Pronkin AN (2022) Experimental results of attitude determination functional algorithms implementation in strapdown inertial navigation system. Sensors 22(5):1849. https://doi.org/10.3390/s22051849

ISSN: 2175 9146

Challenges of Computer Vision for Commercial Unmanned Aerial Vehicle Detection

Valentina Grichshenko1 , Assemkhan Mukushev2*Andrey Kokidko2 , Nurzhan Zikiryaev3
1.Institute of Ionosphere Laboratory of Reliability and Safety of Orbital and Ground Space Systems – Almaty – Republic of Kazakhstan.
2.Military Engineering Institute of Radio Electronics and Communications – Almaty – Republic of Kazakhstan.
3.Military Engineering Institute of Radio Electronics and Communications – Department of the Fundamentals of Military Radio Engineering and Electronics – Almaty – Republic of Kazakhstan.

A B S T R A C T

The study aims to analyze the existing computer vision techniques for commercial drone detection to identify their advantages, disadvantages, and determine the best approaches in different application scenarios. The research methodology used synthesis methods to explore and propose combinations of techniques based on an analysis of the methodology and results of other works in the literature. It employed algorithms and sensor data analysis to assess the effectiveness of detection methods, and deduction to formulate hypotheses and conclusions based on data and theories. The main research results include the development of computer vision methods for detecting commercial drones, identifying their visual detectability at different altitudes, analyzing different object detection methods, and evaluating the applicability of these methods for commercial applications. In addition, the study identified the advantages and disadvantages of applying computer vision to commercial drone detection and offered recommendations for further research and practical implementation. The practical value of this study is to improve the detection systems of commercial drones, thereby enhancing the safety and efficiency of their use.

Keywords: *Aircraft; Detection; Sensor systems; Performance evaluation; Advanced technology*

INTRODUCTION

Nowadays, research on the application of computer vision to the detection of commercial unmanned aerial vehicles (UAVs) is proving to be highly relevant and important due to several key factors (Mykhalevskiy et al. 2024; Yermolenko et al. 2024). With the increasing number of commercial UAVs in various industries such as transport, agriculture, surveying, and environmental monitoring, there is a need for effective detection systems (Cazzato et al. 2020; Chen et al. 2023). This is necessitated not only by the increased security and control over the use of such devices but also by the protection of data privacy, especially in areas where sensitive information is present. Research in this area is also stimulated by the active development of the drone technology market itself. T he constant development of new models and types requires appropriate tools and technologies for their detection and monitoring. T he research problem includes several aspects, including ambiguity in the choice of optimal drone detection methods, limitations in the performance of existing algorithms when processing large

amounts of data, difficulties in adapting algorithms to different survey conditions and customer requirements, and problems of defense against cyber-attacks and hacking of detection systems (Perry and Guo 2021). Other issues include the need to address ethical and legal considerations in the use of computer vision technology for UAV detection, and the need to improve the performance and accuracy of detection systems to effectively monitor the growing number of commercial drones in various industries and domains.

Kozachenko (2021) addressed the model of complex application of measures to detect small UAVs, the problems of radio electronic suppression of the UAV navigation system, as well as the features of radio-electronic suppression of the UAV navigation system based on the reception of satellite navigation system signals, and the problems of radio-electronic suppression of UAV control and data transmission radio lines. However, it is necessary to analyze how effective the proposed methods are in real conditions and whether they apply to different types of UAVs.

According to Zhao et al. (2022), the field of computer vision is sufficiently developed to detect and track intruding UAVs. They propose a DUT Anti-UAV dataset that includes extensive material for training detection and tracking algorithms. However, the dataset's effectiveness and its applicability in real surveillance environments require further study. Pawełczyk and Wojtyra (2020) note the significant increase in the number of drone incidents and the need for drone detection systems running on low-performance hardware. However, the performance and reliability of such systems under different operating conditions should be investigated in more detail. Leira et al. (2020) study an object detection, recognition, and tracking system for UAVs applied in a maritime object tracking system. It is important to extend the research to other applications of this system and evaluate its performance in different scenarios. Bazeltsev (2020) states that over the last 10 years, the field of UAVs has expanded rapidly. They are used in various environments such as reconnaissance, surveying, rescue operations, and mapping. UAVs are maneuverable in the air, can be operated by remote control, and can reach high altitudes and distances. Many UAVs are equipped with an inbuilt camera, such as an action camera, which allows the drone to take photos and videos from various angles. However, there are some disadvantages: drone control can be quite complicated. Even when applying the latest advances in software, the pilot must be very careful, as losing control of the drone could mean losing the UAV itself. His study did not address the aspect related to technical limitations and potential risks that may arise when using drones. T he study aims to investigate and evaluate existing computer vision techniques for commercial drone detection, with a focus on identifying the most effective approaches for UAV detection across various contexts. By considering the current limitations and challenges discussed in the literature, the study seeks to assess the performance and applicability of these techniques in realworld scenarios, providing a comprehensive understanding of the strengths and weaknesses of different methods.

METHODOLOGY

The methodology consists of nine sequential steps, each addressing a critical aspect of the research process. These steps include selecting performance indicators, conducting data analysis, synthesizing different algorithms, integrating data from various sensors, applying fusion methods, evaluating algorithm performance, analyzing trends and patterns, researching the visual detectability of drones, and formulating hypotheses and conclusions. A detailed description of each stage is provided below to ensure a clear understanding of the methodology and its application in the context of this study. The simplified process flow (Fig. 1) summarizes the main steps in the methodology for the study of the use of computer vision to detect commercial drones.

Selecting Performance Indicators

The first step was to select appropriate performance indicators to evaluate the use of computer vision in commercial drone detection. The key metrics are accuracy, completeness, F-Score, detection rate, and the number of false positives and missed detections. These metrics enable a comprehensive quantitative evaluation of the performance of detection models, focusing on their accuracy and effectiveness under varying conditions. Evaluation and Optimization of Drone Detection Methods After collecting and analyzing the data, conclusions were drawn about the effectiveness of various drone detection methods. This stage allows us to evaluate which methods provide the best results in real-world conditions and helps to identify weaknesses in the applied approaches that require further optimization.

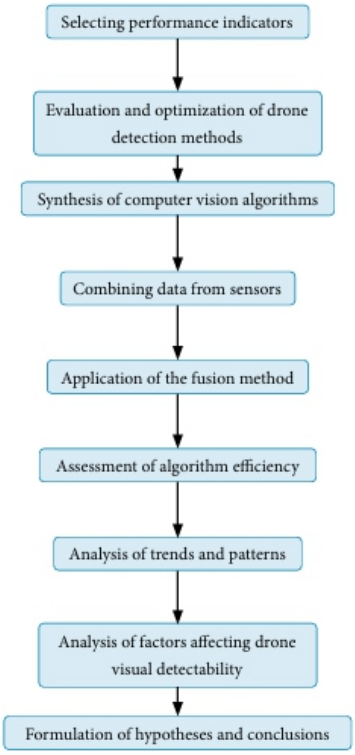

Source: Elaborated by the authors.

Figure 1. Main stages of the methodology for researching the use of computer vision to detect commercial drones.

Synthesis of Computer Vision Algorithms

In this stage of the research, a synthesis method was used to combine different computer vision algorithms to create a more efficient and reliable commercial drone detection system. By combining the strengths of several methods, better detection quality was achieved and a wider coverage of different scenarios and usage conditions was provided, which increased the system's efficiency.

Combining Data from Sensors

The fusion method was also used to combine data from different sensors, such as video cameras, radars, and Light Detection and Ranging (LIDAR). This has resulted in a more comprehensive drone detection system that takes advantage of the strengths of each sensor to improve the accuracy and reliability of the system in different environments. Combining data from different sources makes the system more adaptable to varying conditions.

Application of the Fusion Method

The fusion method involves more than just integrating various input data into a model for classification and detection tasks. It also encompasses the combination of results from different models after they have processed the data. By using outputs from multiple models together, after they have completed their respective processes, we can enhance the stability and efficiency of the drone detection system. This approach helps reduce the number of false positives and improves the accuracy of target detection, as it leverages the strengths of different models and algorithms to provide a more robust final result. Thus, the fusion method not only integrates data but also merges the outcomes of different models to achieve more reliable and precise detections.

Assessment of Algorithm Efficiency

The study used an analytical approach to evaluate the effectiveness of different drone detection algorithms based on metrics such as accuracy, completeness, and detection rate. This stage allows comparing the effectiveness of different methods and choosing the most suitable one for specific application conditions, which is important for further optimization of the system. Analysis of Trends and Patterns Analytical methods were used to identify the main trends and patterns in the behavior of detected objects. This allows for a better understanding of the detection process and optimization of the overall system performance, particularly by adapting to typical drone behavioral patterns. Studying such trends helps to improve detection algorithms for specific conditions.

Analysis of Factors Affecting Drone Visual Detectability

The study also examined the visual detectability of drones at different heights and distances. For this

purpose, data from various sources, such as video footage, sensors, and flight simulations, were used. This research allows for the improvement of visual detection methods by taking into account various factors that affect drone visibility, such as weather conditions and flight altitude.

Formulation of Hypotheses and Conclusions

The last step is to formulate hypotheses and conclusions based on data analysis and logical thinking. Using the deductive method, researchers formulate theoretical models that explain the effectiveness or ineffectiveness of specific drone detection methods. This stage provides general principles and patterns underlying the effectiveness of detection algorithms and suggests areas for further research and improvement of detection technologies.

RESULTS

Evolution of Computer Vision Techniques in Drone Detection

The history of computer vision development in drone detection can be traced through key milestones that show the evolution from early image processing techniques to the advanced methods used today. This timeline outlines the significant advancements in the field, with each stage building upon the previous one (Cazzato et al. 2020).

The journey of computer vision began with the first attempts to use computers to analyze images. In the early stages, computer vision was limited to primitive image processing techniques, such as filtering and thresholding. These methods focused on basic tasks like enhancing image contrast and detecting simple patterns. During this period, researchers also began experimenting with pattern recognition techniques to detect objects in images, laying the groundwork for more advanced methods. T he foundations of computer vision were laid during the initial attempts to use computers for analyzing visual data. At the early stages, primitive image processing techniques such as filtering and thresholding were widely used. Filtering methods aimed to reduce noise, enhance image contrast, and emphasize important features in visual data. Thresholding, on the other hand, was employed to segment images into binary formats by differentiating objects from their background based on pixel intensity values. Although these methods were simple and limited in scope, they provided critical insights into the challenges and possibilities of automated visual analysis, establishing a framework for more sophisticated approaches. T hese early techniques were closely tied to the development of pattern recognition methods, which marked a significant step forward in object detection. Researchers began experimenting with statistical models and feature extraction techniques to identify and classify objects within images (Borodin et al. 2024; Xu et al. 2022). This work laid the groundwork for modern methods introducing the idea of extracting relevant information from raw visual data and using it to train algorithms. Over time, the limitations of these approaches, such as their inability to handle complex patterns or adapt to variations in lighting, and object orientation, highlighted the need for more

advanced methods, paving the way for the development of machine learning and deep learning-based techniques.

Between the 1970s and 1990s, computer vision saw significant development with the introduction of methods based on the extraction of characteristic features from images. Geometric analysis, pattern matching, and object classification became widely used in UAV detection tasks. These methods aimed to identify key features in images, such as edges, corners, and textures, to recognize objects. However, the computational limitations of the time and the huge variability of imaging conditions, such as lighting and scale, hindered further progress.

The period from 2000 to 2010 marked a resurgence in computer vision for drone detection, driven by advances in computing power. Machine learning algorithms started to be actively applied to computer vision tasks, and object classification and detection algorithms trained on large datasets produced significantly better results (Bay et al. 2006; Lowe 2004). Datasets specifically designed for UAV detection became crucial to the development of this field, as they enabled the training of models that could handle the complexities of real-world drone detection. T he true breakthrough came after 2010 with the advent of deep neural networks and deep learning techniques, which revolutionized computer vision. Convolutional Neural Networks (CNNs) emerged as the dominant method for image processing and object detection. CNNs allowed for the automatic extraction of hierarchical features from images, leading to more accurate and robust detection systems (Borges et al. 2024; Borodin et al. 2024). The application of transfer learning methods also enabled the adaptation of pre-trained models for specific tasks like drone detection. This period has seen continuous progress in the field, with CNNs powering some of the most advanced and efficient object detection models used today. The evolution of computer vision techniques for drone detection has laid a strong foundation for the development of advanced algorithms and architectures (Xu et al. 2022). With the advent of CNNs and their ability to extract complex hierarchical features, modern computer vision has reached new heights. Building on this progress, it is crucial to explore the key algorithms and architectures that underpin contemporary advancements in drone detection.

Key Algorithms and Architectures in Computer Vision for Drone Detection

Throughout the development of computer vision techniques for UAV detection, several key algorithms have played an important role. One such method is Harris corner detection, which identifies points in an image where the intensity changes significantly in multiple directions, ideal for detecting distinctive features in images. Another important method is the scale-invariant feature transform (SIFT), which generates local descriptors that are invariant to scale and rotation, making it particularly useful for feature description in various environments. Speeded-up robust features (SURF), a faster alternative to SIFT, improves feature extraction speed while maintaining robustness, making it suitable for real-time

applications. Both SIFT and SURF are widely used in computer vision as feature description methods, typically applied in matching algorithms to find pairs of similar features (Douklias et al. 2022). These methods, along with others, have formed the foundational building blocks for more sophisticated and accurate object detection algorithms used in modern drone detection. Deep learning algorithms, such as CNNs, are highly computationally demanding, especially during the training phase. These models require substantial computational resources due to the large volume of data required for training and the complexity of the models themselves, which consist of many layers and parameters (Tang et al. 2023). Training deep learning models typically requires powerful graphics processing units or specialized processors, as these computational resources accelerate the training process. During inference (prediction) with these models, the computational requirements are reduced but still remain high, particularly for real-time applications in complex conditions (Douklias et al. 2022). Traditional computer vision methods, such as Harris, SIFT, and SURF algorithms, are generally less computationally demanding compared to deep learning-based approaches. These algorithms rely on simpler techniques to detect distinctive points in images, which reduces the strain on hardware resources, making them suitable for tasks with fewer objects or where feature recognition and matching are the primary objectives. For example, algorithms like SIFT and SURF can perform well in scenarios where object detection is not real-time or where the dataset is smaller and less complex. While these methods require less computational power, they may struggle with large, complex datasets or tasks involving real-time object detection, where the need for higher accuracy and faster processing speeds becomes critical. In these cases, deep learning models, despite their higher computational cost, demonstrate significant advantages. Their ability to process large datasets and handle complex features allows them to outperform traditional algorithms in tasks such as detecting objects in real-time or in highly varied environments.

While traditional methods like SIFT and SURF may offer lower computational costs in specific scenarios, they cannot match the effectiveness of deep learning models when dealing with more complex, large-scale tasks. The trade-off between computational efficiency and detection performance becomes evident when considering the increasing demands of modern object detection applications. Faster CNN (R-CNN) improves the original R-CNN by integrating the region proposal network (RPN) to streamline object detection, combining region proposals and classification into one network, significantly boosting both speed and accuracy (Kakaletsis et al. 2021). You Only Look Once (YOLO) takes a different approach by predicting bounding boxes and class probabilities directly from the image in a single pass, making it suitable for real-time applications. Its various versions (YOLOv1 to YOLOv5) have enhanced speed, accuracy, and handling of small objects. Single Shot Multibox Detector (SSD) eliminates region proposals, performing detection in a single pass with multiple feature maps for different object sizes, offering a balance of speed and accuracy. Mask R-CNN extends Faster

R-CNN with a branch for instance segmentation, enabling pixel-level object delineation, which is crucial for detailed applications like medical imaging or autonomous driving. T he Table 1 compares different CNN architectures such as YOLO, Faster R-CNN, SSD, and Mask R-CNN on several important metrics including accuracy, precision, recall, F1-Score, frame rate, resource consumption, suitability for real-time applications, and application domains. These metrics are key to selecting the appropriate architecture depending on the specific requirements of the object detection task, such as speed, accuracy, and resource consumption.

Table 1. Comparison of CNN architectures for object detection.

Model	Accuracy	Precision	Recall	F1-Score	Speed	Resource consumption	Real-time applicability	Use case suitability
YOLO	0.75	0.74	0.77	0.75	45	Medium	Yes	Surveillance, robotics
Faster R-CNN	0.80	0.79	0.82	0.80	10	High	No	Surveillance
SSD	0.78	0.76	0.79	0.77	25	Medium	Yes	Real-time detection
Mask R-CNN	0.82	0.80	0.83	0.81	8	High	No	Segmentation

Source: Based on the study by Tang *et al.* (2023).

Following the comparison of CNN architectures for object detection presented in Table 1, it is also important to evaluate architectures designed for object classification tasks. It is important to note that the YOLO architecture discussed here is YOLOv5, which became widely adopted due to its opensource nature, ease of use, and stable performance at the time the paper was written. However, later versions such as YOLOv6, YOLOv7, and the more recent YOLOv8 and YOLOv9 have introduced significant improvements in accuracy, speed, and resource efficiency. These newer versions have enhanced capabilities in handling small objects, improved robustness in varying environmental conditions, and optimizations for edge computing devices. YOLOv8 and YOLOv9 represent significant advancements in the YOLO architecture, building upon the successes of earlier versions like YOLOv5 and YOLOv7. These newer iterations focus on enhancing the overall performance of the YOLO family by improving both accuracy and efficiency, addressing some of the limitations seen in previous versions. YOLOv8, introduced with improved accuracy and speed, has brought about several innovations in object detection. One of the key features of YOLOv8 is its ability to better handle small objects, which had been a challenge for earlier versions. The model's architecture includes advanced techniques like feature fusion and multi-scale detection, which help in extracting finer details from the input images and improve the model's ability to detect objects at various scales. These advancements make YOLOv8 particularly effective in applications such as security surveillance, autonomous driving, and industrial inspections, where detecting small or partially obscured objects is crucial. Furthermore, YOLOv8 has been optimized for edge computing devices, allowing for faster inference and lower resource consumption, which is essential for real-time applications that require low latency.

YOLOv9, the latest version, continues to push the boundaries of real-time object detection by further refining the architecture for greater robustness and efficiency. It includes several optimizations, such as

improved loss functions and the use of advanced backbone networks that contribute to better feature extraction. YOLOv9 introduces enhanced capabilities for handling challenging environmental conditions, including low-light scenarios and extreme weather, which often cause difficulty for traditional object detection systems. Additionally, YOLOv9 has been designed with a focus on computational efficiency, allowing it to maintain high accuracy and speed even in resource-constrained environments. This makes YOLOv9 particularly suitable for deployment in areas such as mobile robotics and embedded systems, where computational power is often limited but real-time performance is essential. Table 2 below provides a detailed comparison of popular architectures, including AlexNet, VGG, ResNet, and Inception. These architectures are assessed based on performance metrics such as Top-1 and Top-5 accuracy, parameter count, depth, and their notable features. This comparison highlights the evolution of classification-focused CNN architectures and their distinct advantages, which play a crucial role in selecting the most suitable model for specific classification tasks.

Table 2. Comparison of CNN architectures for object classification.

Architecture	Top-1 accuracy (%)	Top-5 accuracy (%)	Parameters (millions)	Layers	Notable Features
AlexNet	57.1	80.2	60.0	8	First deep CNN for classification, ReLU activation
VGG	71.5	89.9	138.0	16	Deeper network, high parameter count
ResNet	77.0	93.3	25.6	50	Skip connections to avoid vanishing gradient
Inception	78.8	93.9	23.0	22	Multi-scale feature extraction

Source: Based on the study by Tang *et al.* (2023).

AlexNet has become one of the key architectures that has significantly advanced the field of deep learning by dramatically reducing the classification error rate compared to previous methods. However, it's worth noting that deep neural networks for classification already existed before AlexNet, in particular the LeCun LeNet5 network, which was developed in the 1990s (Bangar 2022). LeNet5 consisted of three main components: convolutional, clustering, and linear activation functions, and included seven layers. The main problem at the time was the loss of gradient along deep networks, which made training them much more difficult. With the advent of AlexNet, the use of ReLU activations and deeper architectures significantly reduced the error rate and improved training efficiency, which was an important step in the development of deep learning. Although AlexNet was not the first deep network, its innovations were key to the further development of this field.

Deep CNNs represent an evolution from shallow neural networks, characterized by their significantly larger number of layers and parameters. Unlike shallow methods, which typically involve one or two convolutional layers for simple feature extraction, deep CNNs are designed to capture hierarchical and complex patterns in data by stacking multiple convolutional and pooling layers. T his depth allows for the extraction of high-level features essential for complex tasks such as object detection and segmentation. T he specialized techniques in deep CNN architectures address inherent challenges such as the vanishing gradient problem, which becomes more pronounced as the network depth increases. Innovations like batch normalization (to stabilize and accelerate training), skip connections (as

introduced in ResNet, to mitigate gradient loss), and advanced loss functions (e.g., focal loss in dense object detection) enable deep networks to learn effectively even with increased complexity.

Furthermore, these architectures incorporate advanced feature extraction techniques to handle a variety of real-world challenges. For example, multi-scale feature extraction, as seen in SSD and YOLO architectures, enables robust detection of objects across different sizes and conditions. These innovations allow deep CNNs to perform effectively in diverse scenarios, such as varying lighting, background noise, and object occlusion, providing a significant advantage over earlier shallow approaches. Deep neural networks have achieved remarkable advancements across various fields due to key innovations that address critical limitations of traditional models. Batch normalization stabilizes and accelerates training by normalizing the input distribution for each layer. Skip connections, as implemented in ResNet, ensure efficient gradient flow throughout the network, mitigating the vanishing gradient problem in deep architectures. Multi-scale feature extraction, utilized in SSD and YOLO architectures, enhances object detection accuracy across various sizes and challenging conditions. These innovations have made deep neural networks highly effective and adaptable for complex image analysis tasks.

The application of neural network architectures in computer vision opens new opportunities for solving a variety of problems related to image processing. Particularly significant are CNNs, which have become a major tool in this field. These networks consist of convolution layers that allow the automatic extraction and analysis of various features from images (Prayudi et al. 2020). T he application of CNNs finds wide use in object detection tasks, where the network is trained to recognize and localize objects in an image. In addition, they are successfully used in image segmentation, where it is required to identify each pixel of an image and classify it to belong to a particular object or class.

The RPN is a fundamental innovation in the Faster R-CNN architecture that significantly enhances detection speed by generating region proposals directly within the network. Unlike earlier methods such as R-CNN and Fast R-CNN, which relied on external algorithms like selective search for proposal generation, the RPN integrates this process into the neural network itself, streamlining the overall workflow. The RPN operates as a fully convolutional network that scans the input image and predicts candidate bounding boxes, along with their objectness scores, which indicate the likelihood of the region containing an object. By using predefined anchor boxes of varying sizes and aspect ratios, the RPN effectively detects objects of different scales and shapes in a single forward pass. Additionally, its shared convolutional layers with the main detection network reduce computational overhead, making the approach more efficient.

YOLO, with its multiple iterations such as YOLOv1, YOLOv2, YOLOv3, YOLOv4, and YOLOv5, is renowned for its real-time object detection capabilities (Kouvaras and Petropoulos 2024; Prayudi et al. 2020). YOLO processes an image in a single forward pass, dividing it into a grid and predicting

bounding boxes and class probabilities simultaneously. Each subsequent version of YOLO has introduced improvements, such as better feature extraction, optimized anchor boxes, and enhanced training strategies, resulting in higher speed and accuracy.

SSD achieves efficient and accurate object detection by combining multi-scale feature extraction with direct predictions of bounding boxes and class scores. Unlike Faster R-CNN, SSD eliminates the need for a separate proposal generation stage, making it more computationally efficient. By using feature maps at multiple scales, SSD excels at detecting objects of varying sizes and performs well in real-time applications.

In addition to object detection, CNN architectures are widely used for image classification tasks, where the goal is to assign an image to a specific category or class. Notable architectures such as AlexNet, VGG, ResNet, and Inception have set benchmarks in image classification by introducing innovations like deeper layers, skip connections, and improved convolutional operations. The general trend in CNN development is to create deeper and more efficient architectures capable of processing large volumes of data while maintaining high accuracy and speed. These advancements have driven the success of CNNs in both object detection and image classification tasks, solidifying their role as a cornerstone of modern computer vision (Chen et al. 2023).

Building on the advancements in CNN architectures and their pivotal role in object detection and classification, it is essential to consider how these methods are applied specifically to UAV detection. The unique characteristics of UAVs, their visual detectability under varying conditions, and the methods employed to identify them using computer vision form the core of modern UAV detection systems.

Characteristics, Visual Detectability, and Detection Methods for UAVs

Unmanned aerial vehicles are a variety of devices that do not require a pilot on board to perform tasks. They vary in size, shape, and characteristics, depending on their purpose (Tian et al. 2020a). One of the most common types of UAVs is multirotor vehicles equipped with multiple rotating rotors. This includes quadcopters with four rotors, as well as three-, six-, and eight-copters. They can range in size from small, such as the size of the palm of your hand, to large professional models with wingspans of several meters. Multi-rotor UAVs are usually highly maneuverable and capable of hovering in place in the air. Another type of aircraft is fixed-wing vehicles, similar to those found on conventional aircraft. They provide a longer flight time than multirotor vehicles. They range in size from small radio-controlled models to large vehicles capable of carrying heavy and flying long distances. They are often used for monitoring, reviewing, and surveying large areas. There are also hybrid UAVs that combine the features of both multi-rotor and fixed-wing aircraft. These vehicles offer flexibility of use and can combine the advantages of both types (Ariza-Sentís et al. 2023). Their characteristics vary depending on their intended use and may include maximum speed, range, and duration of flight, payload capacity,

types of sensors and equipment used, and degree of autonomy and protection from external factors such as weather and wind. The visual detectability of drones at different altitudes and distances depends on several factors, including their size, shape, color scheme, and environmental lighting and background.

At low altitudes and close ranges, UAVs can be easily spotted due to their distinctive sounds and movement characteristics. Multirotor vehicles, for example, often emit a characteristic noise from rotating rotors, making them visible even at low altitudes. Fixed-wings UAVs may be less conspicuous at low altitudes due to the lack of sound, but their large size and flight characteristics can attract attention (Lai and Huang 2020). However, at high altitudes and long distances, their visual detectability is reduced. Multirotor vehicles may become less conspicuous due to their reduced size against the surrounding background and the lack of brightness of LEDs or other markers on the hull. Fixed-wings UAVs, on the other hand, may retain higher detectability due to their larger size and brighter markers. Lighting also plays an important role in the visual detectability of aircraft. In bright sunlight, the contrast between the vehicle and the environment may be low, making them less visible. However, in low-light conditions or when the angle of view changes, the vehicle may become more visible (Castellano et al. 2020). Thus, visual detectability at different altitudes and distances depends on many factors and can be vary depending on the viewing conditions. Methods for detecting objects in images can be divided into two main groups: feature-based methods and methods using object detectors. Feature-based methods are designed to extract characteristic features of objects in images, such as corners, contours, or textures. The classic methods of this group include SIFT and SURF. These methods have low computational requirements and can provide fairly good accuracy in images with a small number of objects. At the same time, they have significant limitations: sensitivity to changes in lighting, scale, and viewing angle (Oyallon and Rabin 2015; Sadou and Njoya 2023). Adapting and optimizing computer vision models for different drone detection scenarios requires the use of specialized data augmentation methodologies. While data augmentation is often employed to minimize the amount of training data, its primary objective is frequently to achieve class balancing. For instance, in cases where certain drone classes are underrepresented in the dataset, augmentation techniques such as duplicating and transforming samples of the minority class (e.g., through rotation, scaling, or mirroring) can help balance the dataset. This ensures the model does not overfit to more frequently occurring classes, improving its generalization ability across all categories. In addition to augmentation, simpler techniques like data downsampling can also address imbalances. By reducing the number of samples in overrepresented classes, this method provides a straightforward approach to balancing datasets, particularly when computational resources or data complexity are limited. It is worth noting that in some cases, alternative strategies such as training from scratch, transfer learning, or fine-tuning on pre-trained models can eliminate the need for data augmentation entirely. These methods enable model adaptation to specific tasks by leveraging existing knowledge or highly customized training processes, thereby bypassing the need for extensive

augmentation (Sivakumar and Tyj 2021). Color transformations are an equally important tool in enhancing the robustness of drone detection models. Changing the brightness, contrast, saturation, adding noise, and simulating different color spaces help models become invariant to variations in lighting and camera sensors. This approach is critical for ensuring stable operation of drone detection systems in different weather conditions and times of day. These transformations can be applied effectively as long as spectral information is not crucial for the specific method being used. For example, if only RGB data is being used, almost any transformation can be applied to the image to increase the amount of data and make the training set as general as possible, thus representing the most diverse situations. However, if spectral information is important, such transformations should not be used. More advanced techniques include generative data augmentation methods. Generative Adversarial Networks (GANs) allow for the creation of synthetic images of drones with a high degree of realism. These artificially generated images can fill in gaps in the training data, especially for rare or complex surveillance scenarios. The result of these methodologies is the creation of more versatile and robust computer vision models that can effectively detect and classify drones in a wide range of real-world scenarios (Sonkar et al. 2023; Xu et al. 2022). T he use of color transformations and generative data augmentation techniques has significantly enhanced the robustness of drone detection models, enabling them to perform reliably under diverse environmental conditions. These advancements have laid the groundwork for more sophisticated approaches in UAV detection. The integration of deep learning techniques, particularly CNNs and GANs, has further revolutionized this field, providing unparalleled accuracy and efficiency in detecting and classifying UAVs.

Advancements in Deep Learning for UAV Detection

Image segmentation identifies each pixel in an image and classifies it as belonging to an object. This method provides accurate object boundaries and the ability to distinguish between objects with overlapping contours but requires high computational resources and is prone to errors under complex imaging conditions (Ferreira et al. 2020). To summarize, the choice of object detection method depends on the specific task, accuracy and speed requirements, and available computational resources (Table 3).

Table 3. Comparison of object detection methods.

Method	Pros	Cons
Feature-based	Low requirements for computing resources	Sensitivity to changes in lighting and scale
	Good accuracy on images with a small number of objects	Sensitivity to viewing angles
Object detectors	High-speed image processing	Computationally intensive
	High accuracy of object detection	The need for large datasets for training
Image segmentation	The exact boundary of the objects	High computing resource requirements
	Ability to distinguish between objects with overlapping contours	Prone to errors under difficult surveying conditions

Source: Based on Ferreira *et al.* (2020), Kozachenko (2021), and Leira *et al.* (2020).

Drone detection and classification methods using computer vision, machine learning, and deep learning have different approaches and features. An important technology is image segmentation, which allows you to identify each pixel of an image and classify it as part of a specific object. This method provides accurate object boundaries and the ability to distinguish between objects with overlapping contours, but it requires significant computing resources and is prone to errors in difficult shooting conditions (Luo et al. 2023; Terven et al. 2023). T he use of deep learning and neural networks has become one of the most effective approaches in modern computer vision technology. Deep learning allows you to create complex neural networks that can automatically extract features from images and learn from large amounts of data. The most common approach to detecting UAVs is to use CNNs. Such networks can process images efficiently and accurately, identifying the characteristic features of objects (Tian et al. 2020b). Neural network architectures such as Faster R-CNN, YOLO, SSD, and Mask R-CNN are actively used to detect UAVs in images. These models are able to work in real-time and provide high accuracy of object detection even in the presence of strong background noise or changes in lighting. The use of deep learning and neural networks allows for the automation and improvement of airspace control, which is especially important in the context of the growing number and diversity of UAVs (Tang et al. 2023). Although the paper primarily focuses on classification and detection, it is important to also acknowledge the significant advancements in segmentation networks, which are designed specifically for tasks requiring pixel-level understanding of images. T hese architectures play a critical role in many applications, including medical image analysis, autonomous driving, and scene understanding. Some of the most notable segmentation architectures include U-Net, DeepLab, SegNet, Fully Convolutional Networks (FCN), and PSPNet (Yu et al. 2023). U-Net is a widely used architecture in medical image segmentation. It is characterized by its symmetric encoder-decoder structure, with skip connections between corresponding layers in the encoder and decoder. These connections help retain spatial information, making U-Net highly effective for precise pixel-level segmentation tasks. Its ability to work with relatively small datasets while achieving high performance has made it a popular choice in the field of biomedical image analysis. DeepLab is another powerful architecture for semantic segmentation, known for its use of atrous convolutions (dilated convolutions), which allow the network to capture multi-scale context without losing resolution. DeepLab has undergone several iterations, with DeepLabv3+ being one of the most advanced versions, incorporating encoder-decoder structures and advanced atrous spatial pyramid pooling (ASPP) to improve segmentation accuracy in complex scenarios, such as urban and natural scene segmentation (Vasterling and Meyer 2013).

SegNet is another encoder-decoder network, with a focus on efficient feature extraction and segmentation. Unlike U-Net, SegNet employs max-pooling indices in the decoder to improve segmentation quality while reducing the computational load. It has been particularly useful in applications requiring real-time performance, such as autonomous vehicles and robotic systems. FCNs

were among the first architectures to introduce the concept of using fully convolutional layers for semantic segmentation. By replacing the fully connected layers of traditional CNNs with convolutional layers, FCNs can handle input images of any size and generate pixel-wise predictions. This architecture has been foundational in advancing the field of deep learning-based segmentation (Mittal et al. 2020).

Pyramid Scene Parsing Network (PSPNet) takes a different approach by using pyramid pooling to capture context at multiple scales. This multi-scale context helps the network understand global scene information, which is essential for accurate segmentation of complex scenes. PSPNet has proven highly effective for large-scale scene parsing tasks, including street scene segmentation for autonomous driving (Minaee et al. 2022). Although some of the networks discussed, such as YOLO and Faster R-CNN, can be adapted to segmentation tasks, their concept was developed for object detection and classification. These networks focus on defining the boundaries of objects and their categories, rather than on the exact definition of each pixel of the image, which is the main task of segmentation. although they can be adapted for segmentation, they are not optimal for such tasks compared to networks specifically designed for segmentation, such as U-Net or DeepLab.

Adapting drone detection algorithms to specific survey conditions and customer requirements plays a key role in ensuring the effective operation of the surveillance and control system. Environmental conditions, such as lighting, weather, landscape type, and obstacles, must be taken into account. For example, when shooting in low or changing light conditions, detection algorithms must be adapted to work more efficiently. However, such adaptations must be accompanied by a rigorous evaluation of performance to ensure that the algorithms continue to deliver accurate and reliable results under varying conditions. One of the key tools for evaluating the performance of these detection algorithms is the confusion matrix. Confusion matrices are widely used to assess classification models, particularly in object detection tasks. This tool visually demonstrates how the model classifies objects and helps identify types of errors, such as false positives and false negatives. By using confusion matrices, it becomes easier to understand whether the model is working correctly in real-world conditions and how it can be further optimized to improve results. Below is an example of a confusion matrix and its components for drone detection, which highlights its importance as an effective instrument for evaluating the accuracy of the model (Samaras et al. 2019; Shaharom and Tahar 2023). Customer requirements may vary depending on the specific task and application. In the security sector, a customer may be interested in high detection accuracy and speed, while in natural resource monitoring, they may be interested in reliability and the ability to work in different climatic conditions. Therefore, algorithms must be customized and optimized to meet specific requirements (Macukow 2016; Taha and Shoufan 2019).

The types of drones are extremely diverse and are classified according to many parameters. They can differ in size – from micro to large devices, in purpose – military, commercial, or entertainment, in

configuration – multi-rotor, airplane-type, or hybrid. Drones differ in flight range, payload capacity, and type of power plant – electric, gasoline, or hybrid. Thus, adapting UAV detection algorithms to specific survey conditions and customer requirements involves considering the environment, customizing them for specific tasks, taking into account the characteristics of the objects to be detected, and optimizing the use of resources. This ensures efficient and reliable operation of the detection system in various conditions and applications.

Integration of Multi-Sensor Technologies

Metrics for evaluating the performance of UAV detection algorithms are essential tools for analyzing and comparing their effectiveness under different conditions and application scenarios. Accuracy, for instance, measures how correctly an algorithm detects UAVs, calculated as the ratio of correctly detected aircraft to the total number of objects flagged as UAVs. The higher the accuracy, the fewer the false positives. Completeness, on the other hand, assesses how well the algorithm detects all real-world UAVs, defined as the ratio of correctly detected UAVs to the total number of UAVs present. A higher completeness means fewer Given the importance of these metrics in assessing algorithm performance, it is crucial to regularly calibrate and update UAV detection systems to adapt to changing conditions, such as varying lighting, weather, and new UAV designs. These updates ensure that detection systems remain reliable, accurate, and efficient over time. Looking ahead, the integration of additional technologies, such as LIDAR and radar, will play a vital role in enhancing UAV detection capabilities. While computer vision algorithms are integral to real-time detection, multi-sensor approaches can significantly boost efficiency and reliability. Radar systems, for instance, are invaluable for detecting objects at long ranges, even in challenging weather conditions and low visibility. In combination with computer vision, radar data provides spatial coordinates and velocity information, improving overall system accuracy. LIDAR technology complements these sensors by offering extremely detailed spatial information through laser scanning. LIDAR can generate highly accurate three-dimensional maps of the terrain, enabling precise detection of UAV shapes, sizes, and positions. This synergy between multiple sensors will enhance the robustness and adaptability of UAV detection systems, ensuring higher reliability and efficiency in diverse environments (Jiang et al. 2022).

The F-Score is the harmonic mean between accuracy and completeness. It covers both metrics in a single numerical value and provides an overall measure of the algorithm's performance. The higher the F-Score, the better the combination of accuracy and completeness. The detection rate is the time it takes for the algorithm to detect aircraft in an image or video stream. This metric is important for tasks where a fast response to object detection is required, such as in security systems or airspace monitoring. False positives are the number of objects that the algorithm mistakenly flagged as UAVs when in fact they are not. This metric is important for evaluating unwanted false positives that can affect the reliability of the

detection system. Missed detections are the number of actual UAVs that the algorithm failed to detect. This metric is important for assessing detection completeness and evaluating potential gaps in the T he analysis of these metrics provides a comprehensive evaluation of the performance of the algorithms and determines their suitability for specific tasks and application conditions. When comparing different drone detection methods and algorithms, it is important to consider their features, advantages, and disadvantages (Table 1). This table provides an overview of the main methods and their characteristics, which helps make an informed decision about the most appropriate method for a particular aircraft detection task. A confusion matrix is a valuable tool for evaluating the performance of classification models, particularly in tasks like UAV detection. It provides a clear representation of the model's predictions by categorizing them into four outcomes: true positives (correctly identified UAVs), false positives (objects incorrectly identified as UAVs), false negatives (missed UAVs), and true negatives (correctly identified non-UAVs). This framework simplifies the explanation of key concepts such as model accuracy and error types. The confusion matrix facilitates the calculation of essential metrics like sensitivity (the ability to detect all actual UAVs) and specificity (the ability to correctly identify non-UAVs), offering a comprehensive assessment of the model's effectiveness in real-world applications (Bouguettaya et al. 2022; Kaur et al. 2021). One of the main advantages of modern computer vision algorithms is their high detection accuracy. However, accuracy alone may not fully capture the specific requirements of critical systems. In addition to accuracy, other key metrics such as recall (sensitivity), mean average precision (mAP), mAP50, and the F1-Score are also important, as these metrics provide a more comprehensive evaluation of model performance in complex scenarios. These metrics can be especially valuable in applications like UAV detection, where balancing detection quality and minimizing false positives or false negatives is crucial for system safety, defined here as the ability to accurately identify and respond to threats while minimizing errors that could lead to undetected UAVs or incorrect actions. Furthermore, in critical systems, it is important to consider uncertainty factors and ensure redundancy in the detection process. This redundancy helps maintain safety and operation in the event of a detection failure, ensuring more reliable and continuous performance. Another significant advantage is the wide range of applications of computer vision technology. It can be used not only for UAV detection for security purposes but also in environmental monitoring, area protection, and in the aviation and transport industries to detect and track vehicles. However, besides the advantages, there are some disadvantages to applying computer vision for UAV detection (Iqbal et al. 2024; Kakaletsis et al. 2021). These may include the need for high computational resources, Pyramid Scene Parsing Network (PSPNet) takes a different approach by using pyramid pooling to capture context at multiple scales. This multi-scale context helps the network understand global scene information, which is essential for accurate segmentation of complex scenes. PSPNet has proven highly effective for large-scale scene parsing tasks, including street scene segmentation for autonomous driving (Minaee et al. 2022).

Although some of the networks discussed, such as YOLO and Faster R-CNN, can be adapted to segmentation tasks, their basic concept was developed for object detection and classification. These networks focus on defining the boundaries of objects and their categories, rather than on the exact definition of each pixel of the image, which is the main task of segmentation. Therefore, although they can be adapted for segmentation, they are not optimal for such tasks compared to networks specifically designed for segmentation, such as U-Net or DeepLab. the dependency on environmental conditions such as lighting and weather, and the potential for false positives or negatives in complex scenarios. Addressing these challenges is crucial for the effective deployment of computer vision systems in real-world applications (Kouvaras and Petropoulos 2024).

Some computer vision methods, especially those based on deep learning, require significant computational resources for training and inference. This may require the use of powerful computing systems and infrastructure (Poplavskyi 2024). In addition, computer vision methods may be sensitive to imaging conditions such as changes in lighting, weather conditions, and other environmental factors. This can degrade the performance of algorithms under uncontrolled conditions, requiring additional efforts to adapt and optimize the methods for different imaging scenarios.

It is also worth noting that to maintain the effectiveness of the aircraft detection system, the computer vision algorithms must be calibrated and updated regularly to meet changing conditions and task requirements. This requires additional time and resources to maintain and support the system. Overall, despite some limitations, the application of computer vision for commercial UAV detection is an effective and promising approach that can significantly improve safety and efficiency in various applications. T he prospects for further research in the application of computer vision for commercial UAV detection are promising and offer significant benefits in various aspects. One of the key areas of focus in this area is to continuously improve the accuracy and reliability of detection algorithms. The development of new computer vision techniques and the improvement of existing ones will lead to more accurate results, which is essential to ensure the safety and efficiency of the detection system.

The integration of LIDAR into drone detection systems provides unique advantages that dramatically increase the efficiency of airspace monitoring. LIDAR provides extremely precise three-dimensional spatial information, allowing for the instantaneous determination of geometric parameters of drones with millimeter accuracy. Unlike traditional optical systems, LIDAR technology can clearly identify the shape, size, and spatial orientation of unmanned vehicles even in difficult environmental conditions. The key advantage of the integration approach is the ability to detect drones in conditions where traditional technologies are ineffective. T his is especially relevant for ensuring the security of critical infrastructure, airports, sensitive facilities, and mass events where the most complete control of the airspace is required (Poplavskyi 2024).

Infrared sensors are vital components in UAV detection systems, as they enable effective monitoring in low visibility conditions such as at night or during poor lighting. These sensors operate by detecting thermal radiation, allowing objects to be identified based on their temperature differences from the surrounding environment. Infrared sensors are especially valuable for detecting drones in challenging weather conditions, such as fog, rain, or snow, where traditional optical cameras may struggle to provide clear images. T he integration of infrared sensors with other sensor types, such as video cameras and radars, creates more versatile and reliable drone detection systems, significantly enhancing both accuracy and detection efficiency in a variety of environmental conditions (Chen et al. 2023). Infrared sensors contribute additional data that complements other sensor outputs, enabling more detailed and real-time observation of objects. T he advantages of infrared sensors lie in their ability to detect objects in conditions where optical sensors are ineffective, such as low-light or in difficult weather. They also offer a non-intrusive method for detecting drones, which is crucial for maintaining security without disrupting the surrounding environment (Du et al. 2022). Infrared sensors are highly effective for continuous monitoring and can operate autonomously in real-time, making them crucial for applications such as critical infrastructure protection, security monitoring, and airspace control. Their importance in providing redundancy in detection systems, where reliability and safety are paramount, cannot be overstated. Overall, further research in this area will focus on the development of more accurate, faster, and more reliable UAV detection systems to enable their effective use in various fields such as security, monitoring and control, and in the transport industry. Summarizing the research on the application of computer vision to commercial UAV detection, several important conclusions and generalizations can be drawn. T he integration of computer vision with other sensory data, such as radar and infrared sensors, plays a crucial role in enhancing detection systems. By combining these technologies, we can achieve more complete and efficient systems capable of operating effectively in a variety of environments and scenarios. This multi-sensor approach is essential not only for improving detection accuracy but also for adapting to challenging and changing conditions.

The future of real-time UAV detection systems lies in further advancing these technologies. A key focus of this development will be to optimize computer vision algorithms to ensure the fastest and most accurate detection of UAVs, even in highly dynamic and complex environments. The goal is to create intelligent systems capable of instantaneously recognizing and classifying drones. However, the development of such systems is not limited to computer vision alone. The integration of computer vision with other technologies, such as radar, acoustic, and thermal imaging systems, is vital for increasing detection reliability and minimizing recognition errors. This approach will allow for more robust and efficient UAV detection systems that can operate in a broader range of conditions.

One such technology that promises to significantly improve UAV detection is LIDAR. By combining LIDAR with other sensors like radar, LIDAR offers extremely detailed spatial information, enabling the

precise detection of UAVs even in conditions where optical cameras and traditional detection methods may fail. Radar, for example, has already demonstrated its ability to detect drones at long distances, even in poor visibility conditions such as fog or rain, where optical sensors struggle. This data fusion approach, which integrates radar, LIDAR, and infrared cameras, is poised to enhance the effectiveness of UAV detection systems, ensuring they are both accurate and reliable across a variety of operational scenarios.

Practical results show that combined systems using radar, LIDAR, and infrared sensors achieve much better outcomes compared to using a single sensor. For example, one system that integrated these technologies demonstrated a 95% detection accuracy while simultaneously reducing false positives to 5%, which significantly surpasses the results of individual sensors (Du et al. 2022; Poplavskyi 2024). This highlights the importance of integrating data from different sensors to achieve high accuracy and reliability in the system. Data fusion compensates for the weaknesses of individual sensors: radar works well in poor visibility but does not provide detailed characteristics of objects, while LIDAR and infrared cameras offer additional capabilities for precise detection under various conditions. The use of neural networks to process fused data enables real-time drone detection, which is crucial for rapid response in complex scenarios.

Experimental and practical results confirm the effectiveness of data fusion methods from different sensors in creating reliable drone detection systems. They demonstrate significant advantages over the use of individual sensors, particularly in improving accuracy, reducing false positives, and enhancing operational efficiency in challenging conditions.

DISCUSSION

The results of this study confirm the significance of using computer vision to detect commercial drones to improve safety and efficiency in various applications. The study determined that the use of advanced computer vision techniques can provide high detection accuracy and system reliability. Similar findings are obtained in studies conducted by other researchers dealing with similar topics. For instance, the study by Akbari et al. (2021) on the application of computer vision to analyze videos and images captured by drones highlights the importance of using technology to improve UAV functionality and safety. However, the results of this study are peculiar due to the focus on a specific application area – UAV detection. While the study by the researchers covers a wide range of applications of data from drones, the analysis focuses on the specific task of object detection. T hus, while both studies support the importance of using computer vision to improve safety and efficiency in the aviation industry, the results of this study add value by drawing attention to specific aspects of the application of this technology in UAV detection. A study conducted by Kakaletsis et al. (2021) and this study share similar aspects in that they both address safety issues in the context of drone use and recognize the importance

of integrating safety knowledge into drone algorithms and architectures. Both studies also consider the role of computer vision in improving the safety and efficiency of drone use. However, while the study by the researchers focuses on analyzing the increasing use of autonomous drones and the importance of legal regulation in area, the study written above focuses on analyzing and optimizing computer vision techniques for detecting commercial to improve safety and control their use in various industries.

Chelluri and Manjunathachari (2019) and Mittal et al. (2020) reviewed state-of-the-art object detection algorithms and their applicability to low-altitude drone data. The main objective of this study is to survey and analyze algorithms such as Faster R-CNN,YOLO, SSD, and RetinaNet and their applicability to specific low-altitude data. In contrast, this study focuses on the analysis and optimization of computer vision techniques for the detection of commercial UAVs in various industries. This study seeks to develop more efficient and robust UAV detection systems, making them more applicable and practical in various fields of endeavor. The approach in the study not only considers existing algorithms but also proposes adaptation and optimization of these methods to suit specific needs and survey conditions. Thus, unlike the study by the researchers, which concentrates on algorithm review, this study aims to provide applicable solutions for UAV detection in real-world environments. Perry and Guo (2021) present a new remote sensing approach to measure the dynamic displacement of three-dimensional structures using a sensor system on UAVs and optical and infrared cameras. This research significantly contributes by the integration of different types of cameras to measure three-component displacement and the development of new data

processing algorithms to extract information from video. Its performance has been validated by laboratory experiments, indicating its potential relevance in the field of measuring the dynamic structural response of three-dimensional structures. Both studies highlight the need for further research and innovation in commercial UAV detection. However, the researchers focus on the development of a new sensing method using optical and infrared cameras on UAVs, while this study offers general conclusions and recommendations for improving UAV detection systems, including computer vision algorithms, integration of data from different sensors, and system security. A study by Ramachandran and Sangaiah (2021) and this study highlight the role of computer vision in the context of UAVs and its application to real-time object detection and tracking. Both studies emphasize the importance of these tasks for monitoring different environments and identifying gaps in existing research, which helps to identify directions for future research. The methodology of both studies includes a detailed literature review on object detection and tracking using UAVs and the development of methods to detect objects in UAV images. Both studies also enumerate specific datasets for these tasks and summarize existing research work in different UAV applications. However, the study of the researchers is more focused on the literature review and classification of object detection methods in UAV images, while this study is more specifically focused on analyzing the performance of UAV detection methods and their suitability

for specific tasks and applications. Thus, although both studies address similar topics, they have different biases and approaches to analyzing the issues under investigation. T his study focuses on analyzing the findings and recommendations for improving UAV detection systems. It notes that to improve the performance and reliability of such systems, improvements in computer vision algorithms and integration of data from different sensors such as radar, LIDAR, and infrared sensors are needed. It also emphasizes the importance of real-time operation and highlights the potential threats and risks associated with the use of such systems, which requires further research in cybersecurity and data protection.

CONCLUSION

The study highlighted the significant benefits of using computer vision to detect drones, including its ability to provide high accuracy and rapid response to threats. This is an important aspect of the work, as it emphasizes the importance of the system's operational effectiveness in detecting and responding to potential threats in real-time. Computer vision for drone detection not only ensures high accuracy in UAV identification, but also guarantees a quick response, which is critical for applications that require immediate action, such as security and surveillance. In the context of the study, high accuracy is only one of the key metrics used to evaluate the effectiveness of drone detection systems. While accuracy plays a crucial role, other performance metrics such as recall, precision, and F1-Score are equally important and should be considered when assessing the overall performance of the system. These metrics have been discussed throughout the study, providing a more complete understanding of the system's capabilities beyond simple accuracy. It is important to emphasize the importance of these additional metrics as they help to provide a complete picture of the strengths and weaknesses of the detection system.

The study has determined that deep learning architectures, particularly deep CNNs, play a central role in solving UAV detection tasks. This terminology aligns with the specific usage in the paper, where deep CNNs are highlighted for their ability

to automatically extract hierarchical features from visual data, significantly enhancing the accuracy and reliability of detection systems. These architectures are especially effective in challenging conditions, such as varying lighting, poor visibility, or different background obstacles, making them essential for robust and adaptive UAV detection systems. Data fusion involves not only integrating diverse inputs into a model for classification and detection but also combining the results and methods used during the detection process. This means that fusion can occur at different stages, from pre-processing, where different types of data can be combined to create a more comprehensive view, to combining the output from multiple models after processing. In addition, fusion can include the integration of different detection methods, allowing the strengths of each method to be combined to achieve more accurate and

reliable results. Deep learning, particularly CNNs, has greatly improved the efficiency of processing large volumes of data and enabled the implementation of more complex and adaptive UAV detection methods. This confirms the importance of such technologies for achieving high results in real-time, particularly through integration with other sensors such as radar and LIDAR. At the same time, despite their numerous advantages, the use of deep networks requires significant computational resources, which must be considered when developing real-world detection systems.

The importance of adapting UAV detection algorithms to specific survey conditions and customer requirements such as lighting, weather, landscape type, and object specificity was emphasized. It is necessary to consider the different needs of customers and optimize the algorithms to meet their requirements. It was also found that to maintain the effectiveness of the drone detection system, it is important to regularly calibrate and update the computer vision algorithms according to changing conditions and task requirements. This may require additional time and resources, but it is necessary to ensure reliable system performance. The application of computer vision to the detection of commercial UAVs promises to be an effective and promising approach that can significantly improve safety and efficiency in a variety of applications. The development of new methods and the improvement of existing methods will enable more accurate results to be achieved. T he visual detectability of UAVs at different altitudes and distances is described, considering factors such as size, shape, color scheme, lighting, and environmental background. The study reveals the future of real-time UAV detection systems and suggests a direction for further research: improving the adaptability of detection systems to different imaging conditions, including lighting, climatic zones, and UAV movement scenarios. This direction will develop more efficient and robust detection systems, contributing to the safety and efficiency of UAV applications in various fields. Further research in these areas can lead to more efficient and reliable UAV detection systems, which in turn contributes to improved safety and efficiency in various UAV applications.

CONFLICT OF INTEREST

Nothing to declare.

AUTHORS' CONTRIBUTION

Conceptualization: Grichshenko V; Methodology: Mukushev A, Kokidko A, and Zikiryaev N; Software: Kokidko A and Zikiryaev N; Validation: Mukushev A and Kokidko A; Formal analysis: Grichshenko V and Zikiryaev N; Investigation: Mukushev A and Zikiryaev N; Resources: Grichshenko V and Mukushev A; Data Curation: Grichshenko V and Kokidko A; Writing - Original Draft: Grichshenko V and Mukushev A; Writing - Review & Editing: Grichshenko V, Mukushev A, Kokidko A, and Zikiryaev N; Visualization: Kokidko A and Zikiryaev N; Supervision: Mukushev A; Final

approval: Mukushev A.

DATA AVAILABILITY STATEMENT

The data that support the findings of this study are available on request from the corresponding author.

FUNDING

Science Committee of the Ministry of Science and Higher Education of the Republic of Kazakhstan. Grant No: BR109012/0221.

ACKNOWLEDGMENTS

Not applicable.

REFERENCES

Akbari Y, Almaadeed N, Al-Maadeed S, Elharrouss O (2021) Applications, databases and open computer vision research from drone videos and images: A survey. Artif Intell Rev 54:3887-3938. https://doi.org/10.1007/s10462-020-09943-1

Ariza-Sentís M, Baja H, Vélez S, Valente J (2023) Object detection and tracking on UAV RGB videos for early extraction of grape phenotypic traits. Comput Electron Agric 211:108051. https://doi.org/10.1016/j.compag.2023.108051

Bangar S (2022) LeNet 5 Architecture Explained. Medium. [accessed Feb 26 2024]. https://medium.com/@siddheshb008/lenet-5-architecture-explained-3b559cb2d52b

Bay H, Ess A, Tuytelaars T, Van Gool L (2006) SURF: speeded up robust features. Comput Vis Image Underst 110(3):346-359. https://doi.org/10.1007/11744023_32

Bazeltsev KO (2020) UAV navigation software based on openCV and tensorflow. Kyiv: National Aviation University. https://dspace.nau.edu.ua/handle/NAU/47729

Borges SF de S, Cardoso Júnior MM, Castilho DS (2024) Method for defining the automation level of an eVTOL. J Aerospace Technol Manag 16:e2224. http://doi.org/10.1590/jatm.v16.1342

Borodin V, Selin A, Kolesnichenko V, Kalyagin M (2024) Selection of routing metrics and service channel characteristics of ad hoc network for UAV swarm. J Aerospace Technol Manag 16:e2324. http://doi.org/10.1590/jatm.v16.1343

Bouguettaya A, Zarzour H, Kechida A, Taberkit AM (2022) Vehicle detection from UAV imagery with deep learning: a review. IEEE Trans Neural Netw Learn Syst 33(11):6047-6067. https://doi.org/10.1109/TNNLS.2021.3080276

Castellano G, Castiello C, Mencar C, Vessio G (2020) Crowd detection for drone safe landing through

fully-convolutional neural networks. In: SOFSEM 2020: theory and practice of computer science. Cham: Springer. https://doi.org/10.1007/978-3-030-38919-2_25

Cazzato D, Cimarelli C, Sanchez-Lopez JL, Voos H, Leo M (2020) A survey of computer vision methods for 2D object detection from unmanned aerial vehicles. J Imaging 6(8):78-89. https://doi.org/10.3390/jimaging6080078

Chelluri HB, Manjunathachari K (2019) SIFT and it's variants: an overview. Paper presented 2019 Proceedings of International Conference on Sustainable Computing in Science, Technology and Management. Amity University Rajasthan; Jaipur, India.

Chen C, Zheng Z, Xu T, Guo S, Feng S, Yao W, Lan Y (2023) Yolo-based UAV technology: a review of the research and its applications. Drones 7(3):190. https://doi.org/10.3390/drones7030190

Douklias A, Karagiannidis L, Misichroni F, Amditis A (2022) Design and implementation of a UAV-based airborne computing platform for computer vision and machine learning applications. Sensors 22(5):2049. https://doi.org/10.3390/s22052049

Du K-L, Legun C-S, Mow WH, Swamy MNS (2022) Perceptron: learning, generalization, model selection, fault tolerance, and role in the deep learning era. Mathematics 10(24):4730. https://doi.org/10.3390/math10244730

Ferreira PM, de Almeida DRA, Papa DA, Minervino JBS, Veras HFP, Formighieri A, Santos CAN, Ferreira MAD, Figueiredo EO, Ferreira EJL (2020) Individual tree detection and species classification of Amazonian palms using UAV images and deep learning. For Ecol Manage 475:118397. https://doi.org/10.1016/j.foreco.2020.118397

Iqbal U, Davies T, Perez P (2024) A review of recent hardware and software advances in GPU-accelerated edge-computing single-board computers (SBCs) for computer vision. Sensors 24(15):4830. https://doi.org/10.3390/s24154830 Jiang C, Ren H, Ye X, Zhu J, Zeng H, Nan Y, Sun M, Ren S, Huo H (2022) Object detection from UAV thermal infrared images and videos using YOLO models. Int J Appl Earth Obs Geoinf 112:102912. https://doi.org/10.1016/j.jag.2022.102912 Kakaletsis E, Symeonidis C, Tzelepi M, Mademlis I, Tefas A, Nikolaidis N, Pitas I (2021) Computer vision for autonomous UAV flight safety: an overview and a vision-based safe landing pipeline example. ACM Comput Surv 54(9):181. https://doi.org/10.1145/3472288

Kaur R, Kumar R, Gupta M (2021) Review on transfer learning for convolutional neural network. Paper presented 2021 3rd International Conference on Advances in Computing, Communication Control and Networking. Institute of Electrical and Electronics Engineers; Greater Noida, India. https://doi.org/10.1109/ICAC3N53548.2021.9725474

Kouvaras L, Petropoulos GP (2024) A novel technique based on machine learning for detecting and segmenting trees in very high-resolution digital images from unmanned aerial vehicles. Drones 8(2):43. https://doi.org/10.3390/drones8020043

Kozachenko DV (2021) Development of the concept of optical channel of secure communication with quadrocopters in the conditions of active counteraction. Vinnytsia: Vasyl Stus Donetsk National University.

Lai YC, Huang ZY (2020) Detection of a moving UAV based on deep learning-based distance estimation. Remote Sens 12(18):3035. https://doi.org/10.3390/rs12183035

Leira FS, Helgesen HH, Johansen TA, Fossen TI (2020) Object detection, recognition, and tracking from UAVs using a thermal camera. J Field Robot 38(2):242-267. https://doi.org/10.1002/rob.21985

Lowe DG (2004) Distinctive image features from scale-invariant keypoints. Int J Comp Vis 60(2):91-110. https://doi. org/10.1023/B:VISI.0000029664.99615.94

Luo K, Kong X, Zhang J, Hu J, Li J, Tang H (2023) Computer vision-based bridge inspection and monitoring: a review. Sensors 23(18):7863. https://doi.org/10.3390/s23187863

Macukow B (2016) Neural networks – State of art, brief history, basic models and architecture. Computer information systems and industrial management. Paper presented 2016 15th IFIP TC8 International Conference. IFIP; Vilnius, Lithuania. https://doi.org/10.1007/978-3-319-45378-1_1

Minaee S, Boykov Y, Porikli F, Plaza A, Kehtarnavaz N, Terzopoulos D (2022) Image segmentation using deep learning: a survey. IEEE Trans Pattern Anal Mach Intell 44(7):3523-3542. https://doi.org/10.1109/TPAMI.2021.3059968

Mykhalevskiy D, Vasylyshyn V, Riabkov V, Myronenko R, Bryl D (2024) Method for improving the coverage efficiency of wireless sensor networks based on UAVs. Machinery & Energetics 15(2):81-94. https://doi.org/10.31548/machinery/2.2024.81

Mittal P, Singh R, Sharma A (2020) Deep learning-based object detection in low-altitude UAV datasets: a survey. Image Vis Comput 104:104046. https://doi.org/10.1016/j.imavis.2020.104046

Oyallon E, Rabin J (2015) An analysis of the SURF method. Image Process on Line 5:176-218. http://org/10.5201/ipol.2015.69

Pawełczyk MŁ, Wojtyra M (2020) Real world object detection dataset for quadcopter unmanned aerial vehicle detection. IEEE Access 8:174394-174409. http://doi.org/10.1109/ACCESS.2020.3026192

Perry BJ, Guo Y (2021) A portable three-component displacement measurement technique using an unmanned aerial vehicle (UAV) and computer vision: a proof of concept. Measurement 176:109222. https://doi.org/10.1016/j.measurement.2021.109222

Poplavskyi O (2024) Information technology for image data processing based on hybrid neural networks using geometric features. Inf Technol Comput Eng 21(2):4-16. https://doi.org/10.31649/1999-9941-2024-60-2-4-16

Prayudi A, Sulistijono IA, Risnumawan A, Darojah Z (2020) Surveillance system for illegal fishing prevention on UAV imagery using computer vision. Paper presented 2020 International Electronics Symposium. IEEE; Surabaya, Indonesia. http://doi.org/10.1109/IES50839.2020.9231539

Ramachandran A, Sangaiah AK (2021) A review on object detection in unmanned aerial vehicle surveillance. Int J Cogn Comput Eng 2:215-228. https://doi.org/10.1016/j.ijcce.2021.11.005

Sadou AM, Njoya ET (2023) Applications of artificial intelligence in the air transport industry: a bibliometric and systematic literature review. J Aerospace Technol Manag 15:e2223. http://doi.org/10.1590/jatm.v15.1312

Samaras S, Diamantidou E, Ataloglou D, Sakellariou N, Vafeiadis A, Magoulianitis V, Lalas A, Dimou A, Zarpalas D, Votis K, et al. (2019) Deep learning on multi sensor data for counter UAV applications – A systematic review. Sensors 19(22):4837. https://doi.org/10.3390/s19224837

Shaharom MF, Tahar KN (2023) Multispectral image matching using SIFT and SURF algorithm: a review. Int J Geoinformatics 19(1). https://doi.org/10.52939/ijg.v19i1.2495

Shantyr A (2024) Specifics of quality assessment models application at development and use stages of software systems. Inf Technol Comput Eng 21(1):127-138. https://doi.org/10.31649/1999-9941-2024-59-1-127-138

Sivakumar M, Tyj NM (2021) A literature survey of unmanned aerial vehicle usage for civil applications. J Aerospace Technol Manag 13:e4021. http://doi.org/10.1590/jatm.v13.1233

Sonkar S, Kumar P, Puli YT, George RC (2023) Design & implementation of an electric fixed-wing hybrid VTOL UAV for asset monitoring. J Aerospace Technol Manag 15:e0823. http://doi.org/10.1590/jatm.v15.1297

Taha B, Shoufan A (2019) Machine learning-based drone detection and classification: state-of-the-art in research. IEEE Access 7:138669-138682. http://doi.org/10.1109/ACCESS.2019.2942944

Tang G, Tang G, Ni J, Zhao Y, Gu Y, Cao W (2023) A survey of object detection for UAVs based on deep learning. Remote Sens 16(1):149. https://doi.org/10.3390/rs16010149

Terven J, Cordova-Esparza DM, Ramirez-Pedraza A, Chavez-Urbiola EA, Romero-Gonzalez JA (2023) Loss functions and metrics in deep learning. A review. arXiv:2307.02694.. https://doi.org/10.48550/arXiv.2307.02694

Tian H, Wang T, Liu Y, Qiao X, Li Y (2020a) Computer vision technology in agricultural automation – A review. Inf Process Agric 7(1):1-19. https://doi.org/10.1016/j.inpa.2019.09.006

Tian Y, Zhang C, Jiang S, Zhang J, Duan W (2020b) Noncontact cable force estimation with unmanned aerial vehicle and computer vision. Comput Aided Civ Infrastruct Eng 36(1):73-88. https://doi.org/10.1111/mice.12567

Vasterling M, Meyer U (2013) Challenges and opportunities for UAV-borne thermal imaging. In: Kuenzer C, Dech S, editors. Thermal infrared remote sensing. Remote sensing and digital image processing. Vol 17. Dordrecht: Springer. https://doi.org/10.1007/978-94-007-6639-6_4

Xu X, Zhang L, Yang J, Cao C, Wang W, Ran Y, Tan Z, Luo M (2022) A review of multi-sensor fusion SLAM systems based on 3D LIDAR. Remote Sensing 14(12):2835. https://doi.org/10.3390/rs14122835

Yermolenko R, Klekots D, Gogota O (2024) Development of an algorithm for detecting commercial unmanned aerial vehicles using machine learning methods. Machinery & Energetics 15(2):33-45. https://doi.org/10.31548/machinery/2.2024.33

Yu Y, Wang C, Fu Q, Kou R, Huang F, Yang B, Yang T, Gao M (2023) Techniques and challenges of image segmentation: a review. Electronics 12(5):1199. https://doi.org/10.3390/electronics12051199

Zhao J, Zhang J, Li D, Wang D (2022) Vision-based anti-UAV detection and tracking. IEEE Trans Intell Transp Syst 23(12):25323-25334. http://doi.org/10.48550/arXiv.2205.10851

Instructions for Authors

Essentials for Publishing in this Journal

1 Submitted articles should not have been previously published or be currently under consideration for publication elsewhere.

2 Conference papers may only be submitted if the paper has been completely re-written (taken to mean more than 50%) and the author has cleared any necessary permission with the copyright owner if it has been previously copyrighted.

3 All our articles are refereed through a double-blind process.

4 All authors must declare they have read and agreed to the content of the submitted article and must sign a declaration correspond to the originality of the article.

Submission Process

All articles for this journal must be submitted using our online submissions system. http://enrichedpub.com/ . Please use the Submit Your Article link in the Author Service area.

Manuscript Guidelines

The instructions to authors about the article preparation for publication in the Manuscripts are submitted online, through the e-Ur (Electronic editing) system, developed by **Enriched Publications Pvt. Ltd**. The article should contain the abstract with keywords, introduction, body, conclusion, references and the summary in English language (without heading and subheading enumeration). The article length should not exceed 16 pages of A4 paper format.

Title

The title should be informative. It is in both Journal's and author's best interest to use terms suitable. For indexing and word search. If there are no such terms in the title, the author is strongly advised to add a subtitle. The title should be given in English as well. The titles precede the abstract and the summary in an appropriate language.

Letterhead Title

The letterhead title is given at a top of each page for easier identification of article copies in an Electronic form in particular. It contains the author's surname and first name initial .article title, journal title and collation (year, volume, and issue, first and last page). The journal and article titles can be given in a shortened form.

Author's Name

Full name(s) of author(s) should be used. It is advisable to give the middle initial. Names are given in their original form.

Contact Details

The postal address or the e-mail address of the author (usually of the first one if there are more Authors) is given in the footnote at the bottom of the first page.

Type of Articles

Classification of articles is a duty of the editorial staff and is of special importance. Referees and the members of the editorial staff, or section editors, can propose a category, but the editor-in-chief has the sole responsibility for their classification. Journal articles are classified as follows:

Scientific articles:

1. Original scientific paper (giving the previously unpublished results of the author's own research based on management methods).

2. Survey paper (giving an original, detailed and critical view of a research problem or an area to which the author has made a contribution visible through his self-citation);

3. Short or preliminary communication (original management paper of full format but of a smaller extent or of a preliminary character);

4. Scientific critique or forum (discussion on a particular scientific topic, based exclusively on management argumentation) and commentaries. Exceptionally, in particular areas, a scientific paper in the Journal can be in a form of a monograph or a critical edition of scientific data (historical, archival, lexicographic, bibliographic, data survey, etc.) which were unknown or hardly accessible for scientific research.

Professional articles:

1. Professional paper (contribution offering experience useful for improvement of professional practice but not necessarily based on scientific methods);
2. Informative contribution (editorial, commentary, etc.);
3. Review (of a book, software, case study, scientific event, etc.)

Language

The article should be in English. The grammar and style of the article should be of good quality. The systematized text should be without abbreviations (except standard ones). All measurements must be in SI units. The sequence of formulae is denoted in Arabic numerals in parentheses on the right-hand side.

Abstract and Summary

An abstract is a concise informative presentation of the article content for fast and accurate Evaluation of its relevance. It is both in the Editorial Office's and the author's best interest for an abstract to contain terms often used for indexing and article search. The abstract describes the purpose of the study and the methods, outlines the findings and state the conclusions. A 100- to 250-Word abstract should be placed between the title and the keywords with the body text to follow. Besides an abstract are advised to have a summary in English, at the end of the article, after the Reference list. The summary should be structured and long up to 1/10 of the article length (it is more extensive than the abstract).

Keywords

Keywords are terms or phrases showing adequately the article content for indexing and search purposes. They should be allocated heaving in mind widely accepted international sources (index, dictionary or thesaurus), such as the Web of Science keyword list for science in general. The higher their usage frequency is the better. Up to 10 keywords immediately follow the abstract and the summary, in respective languages.

Acknowledgements

The name and the number of the project or programmed within which the article was realized is given in a separate note at the bottom of the first page together with the name of the institution which financially supported the project or programmed.

Tables and Illustrations

All the captions should be in the original language as well as in English, together with the texts in illustrations if possible. Tables are typed in the same style as the text and are denoted by numerals at the top. Photographs and drawings, placed appropriately in the text, should be clear, precise and suitable for reproduction. Drawings should be created in Word or Corel.

Citation in the Text

Citation in the text must be uniform. When citing references in the text, use the reference number set in square brackets from the Reference list at the end of the article.

Footnotes

Footnotes are given at the bottom of the page with the text they refer to. They can contain less relevant details, additional explanations or used sources (e.g. scientific material, manuals). They cannot replace the cited literature.
The article should be accompanied with a cover letter with the information about the author(s): surname, middle initial, first name, and citizen personal number, rank, title, e-mail address, and affiliation address, home address including municipality, phone number in the office and at home (or a mobile phone number). The cover letter should state the type of the article and tell which illustrations are original and which are not.